POLITECNICO DI TORINO
Master's degree course in Aerospace Engineering

Design of Attitude Control System for satellites with flexible appendages

---

Supervisor:
Capello Elisa
Co-Supervisors:
Gherlone Marco
Mancini Mauro

Candidate:
Di Giorgi Danilo

Academic Year 2023/2024
Graduation Session October

ACKNOWLEDGMENT

I would like to express my sincerest gratitude to my advisors, Professor Elisa Capello, Professor Gherlone Marco, and Doctor Mancini Mauro, for their invaluable guidance, encouragement, and support throughout the course of this research. Their expertise, insight, and unwavering dedication have been essential in shaping both this thesis and my interest in the topics covered during this project.

Abstract

Nowadays, spacecrafts are employed for a wide variety of missions: Earth's observation and monitoring, deep universe investigation, communication and much more. For the success of these missions, it is essential that the satellite is correctly oriented during space flight and maintains this orientation with high pointing accuracy in spite of various perturbations. This objective is pursued by Attitude Determination and Control Systems (ADCS), which is responsible to determine the true attitude and to control the actuators to track desired orientation.

In contemporary space missions, the design of ADCS is complicated by the fact that modern satellites are equipped with different large devices featuring low stiffness and moving parts, such as antennas and solar arrays. In this case, the effects of these devices on the overall system dynamics must be taken into account and the rigid-body model of attitude dynamics must be dismissed. Indeed, the coupling between the flexibility of the structure and the attitude dynamics causes vibrations of the flexible bodies and the internal torques acting on the satellite which disturb the attitude dynamics.

Hence, the object of this work is the design of a three-axis Attitude Control System (ACS) to adequately handle the coupling effects due to the flexible appendages. The satellite model is based on *ICEYE-X1*, which was launched in January 2018 and consisted in a proof-of-concept satellite mission of the Finnish startup *ICEYE*, whose aim is a Synthetic Aperture Radar (SAR) equipped commercial constellation of 48 satellites. The simplified structural model of the spacecraft has been built in MSC Patran and consists of a main rigid body to which the flexible appendages are attached. Next, a Finite Element Method (FEM) analysis is performed by solver MSC Nastran to evaluate natural modes of the structure. The latter are the used to build an appropriate mathematical model for flexible spacecraft attitude dynamics, that captures the coupling effects between structural dynamics and attitude dynamics. Different spacecraft configurations are analysed and the above mathematical model is derived for each of them. This allows to establish the parameters which mainly impact the magnitude of the coupling effects between flexible and attitude dynamics. The comprehension of these aspects is crucial for generalising the procedure for estimating the significance of the coupling effect in other types of satellites.

The second part of this thesis is focused on the design of a robust attitude control technique, i.e the Quaternions Feedback Control (QFC), to handle external perturbations and dynamics uncertainties. The control strategy is tested in a three degree-of-freedom orbital simulator including the mathematical model for attitude dynamics of the flexible spacecraft and the control algorithm. Extensive numerical simulations are performed in Matlab/Simulink environment to study the realization of inertial pointing maneuvers with different spacecraft configurations.

The results show that SAR panels heavily influence the dynamics response of the spacecraft during the attitude maneuvers. This is most evident in the first seconds of simulation, when the transient excites the coupling between attitude and flexible dynamics and vibrations reaching their maximum values. However, the QFC controller proves its ability to counteract and nullify these disturbances by providing appropriate attitude control actions.

Contents

List of Figures

List of Tables

Chapter 1

Introduction

1.1 Introduction to space missions

The advent of modern space satellite missions has marked a profound revolution in our understanding and utilisation of space, thus inaugurating a new era of technological advancement and scientific discovery. The objectives of these missions are diverse, encompassing scientific research, Earth observation, telecommunications, navigation, and global positioning systems. The deployment of sophisticated satellites equipped with advanced sensors and instruments enables scientists and engineers to monitor environmental changes, track weather patterns, and study cosmic phenomena in unprecedented detail. The vast quantity of data collected has proved invaluable in addressing a number of global challenges, including climate change, natural disasters and resource management.

The monitoring of the Earth has become one of the most critical functions of modern satellite missions, representing a significant advancement in Earth observation technology. Satellites equipped with remote sensing technologies provide uninterrupted, comprehensive, and high-resolution images of the Earth's surface, offering a detailed and continuous representation of the planet's surface. Such images facilitate the monitoring of deforestation, urban expansion and agricultural productivity. Moreover, satellites are of significant value in the context of disaster management, offering real-time data during natural disasters such as hurricanes, earthquakes and floods. This allows for a more rapid and effective response to such occurrences. A significant technological advancement in the domain of Earth observation has been the development and deployment of Synthetic Aperture Radar (SAR) antennas. In contrast to optical imaging systems, SAR antennas are capable of capturing high-resolution images irrespective of meteorological conditions or the time of day. This attribute is especially beneficial for monitoring regions that are frequently obscured by clouds or experience extended periods of darkness, such as the polar areas. SAR technology enables comprehensive surface analysis, including topographical mapping, soil moisture estimation, and the detection of subtle ground movements, which are vital for investigating geophysical processes and mitigating natural hazards.

Moreover, satellites play an integral role in our daily lives, as they facilitate global communications. They facilitate internet connectivity, broadcasting services, and real-time communication across continents, thereby reducing the digital divide and ensuring that even the

most remote regions of the planet have access to information and services. Furthermore, the incorporation of satellite technology into the global economy has facilitated enhancements to transportation systems, improvements to logistics, and the provision of support to critical infrastructure.

The advent of innovative technologies and international collaborations has facilitated the development of more efficient, cost-effective, and multi-functional satellites. The deployment of small satellite constellations has gained considerable interest due to their capacity to provide comprehensive coverage and rapid data transmission. Furthermore, the involvement of the private sector in space exploration has facilitated accelerated advancements, resulting in a reduction in costs and an increase in the frequency of launches.

1.2 ICEYE-X1 Satellite

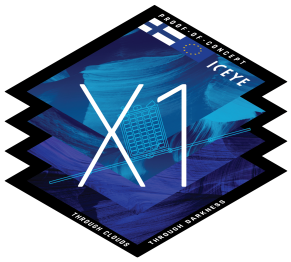

Figure 1.1: ICEYE-X1 mission logo. Credits: ICEYE [1]

In order to create a mathematical model that is as representative as possible of real satellites and to develop a valid attitude control and dynamics control system (ADCS), it was decided that an operational satellite should be chosen as the basis for the model. The satellite selected for this purpose is the ICEYE-X1, developed by **ICEYE Ltd** [1], a Finnish startup established in 2014 from a university nanosatellite group, Aalto-1. The ICEYE-X1 was the proof-of-concept microsatellite mission with a SAR sensor payload, and the first satellite successfully launched by the team on 12 January 2018. Furthermore, it was the inaugural satellite in the world to utilise SAR technology weighing less than 100 kilograms. Additionally, it was the first satellite to be launched by a Finnish commercial enterprise, enabling the generation of radar images of the Earth even when obscured by clouds or darkness. The objective of the mission was firstly to validate the in-orbit performance of the spacecraft and secondly to commence operations with ICEYE customers. The available data can be used for a wide variety of cases, including sea ice monitoring for maritime navigation or environmental changing studies, marine oil spills tracking, helping to prevent illegal fishing. Moreover, another ICEYE's objective is to improve Earth's catastrophes monitoring, like wildfires and flooding, immediately getting clarity about their impacts. These types of operations are possible thanks to the near-real-time insight ICEYE is able to provide, ensuring efficient risk management.
ICEYE-X1 was launched by a Polar Satellite Launch Vehicle (PSLV-C40), one of the launcher of the Indian Space and Research Organisation (ISRO), at the Satish Dhawan Space Centre in India. The satellite was deployed in a sun-synchronous orbit (SSO) with an altitude of 505 km and an inclination of 97.55°. In June 2018, ICEYE Ltd announced the successful ending of ICEYE-X1's mission and the conclusion of its operation.
A proof of ICEYE's SAR technology is shown in fig. 1.2, where in a preliminary flood analysis, ICEYE-X1 combined and processed the data of an European satellite, which is Sentinel-1 by

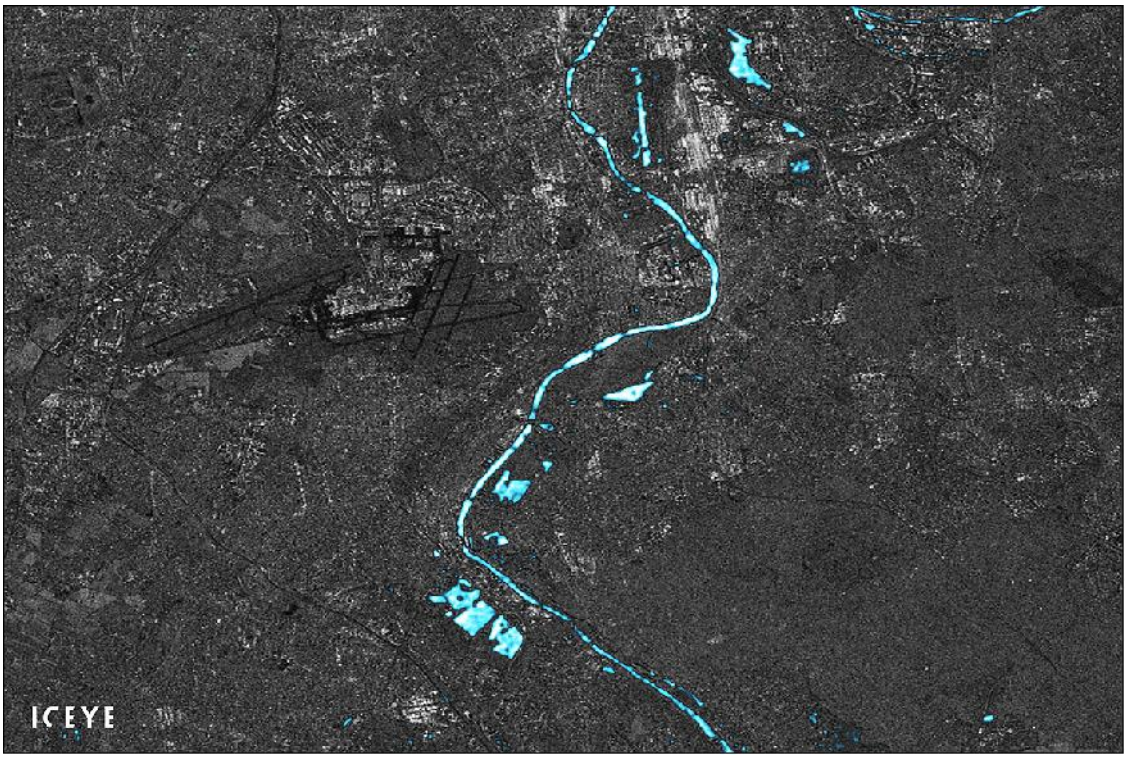

Figure 1.2: ICEYE-X1 preliminary flood analysis exercise image. [2]

European Space Agency (ESA), to foresee potential changes. The figure features the Seine river and Paris Orly Airport, at the beginning of 2018.

ICEYE-X1 spacecraft

ICEYE-X1 has been developed and integrated by ICEYE. The platform is a three-axis stabilized spacecraft with a total mass of 85 kg. The electric power is provided by one fixed solar array and battery packs. ICEYE-X1 falls into micro satellite category, and its size in launch configuration is 70 cm in height × 60 cm in width. The SAR antenna has a total length of 3.25 meters instead. The spacecraft lifetime has been estimated in about two or three years.
One of the objective of the ICEYE team is the implementation of as more as possible of Commercial Off The Shelf (COTSs) components, in order to reduce cost and development time. The main technical specifications of the spacecraft bus are presented in table 1.1 [2].

1.3 Thesis outline

The objective of this study is to design a three-axis Attitude Control System (ACS) that can effectively handle the coupling effects resulting from the flexible appendages. A simplified structural model of the spacecraft has been created in MSC Patran and consists of a main rigid body to which the flexible appendages are attached. Subsequently, a Finite Element Method (FEM) analysis is conducted using the solver MSC Nastran, with the objective of evaluating the natural modes of the structure. The latter are employed to develop an appropriate mathematical

Feature	**ICEYE Satellite**
Average unit mass	85 [kg]
Imaging and polarization	X-band SAR, VV polarization
Resolution	20x20/ 3x3/ 1.5x1.5/ 1x1 [m]
Dynamic range	16 [bit]
Imagining mode	180 s per orbit/120 s continuous
Communication (downlink)	X-band radio, 100+ [Mbit/s]
ADCS	Reaction wheels, magnetorquers, star trackers
Propulsion	Ion thrusters

Table 1.1: Technical capabilities of ICEYE satellite

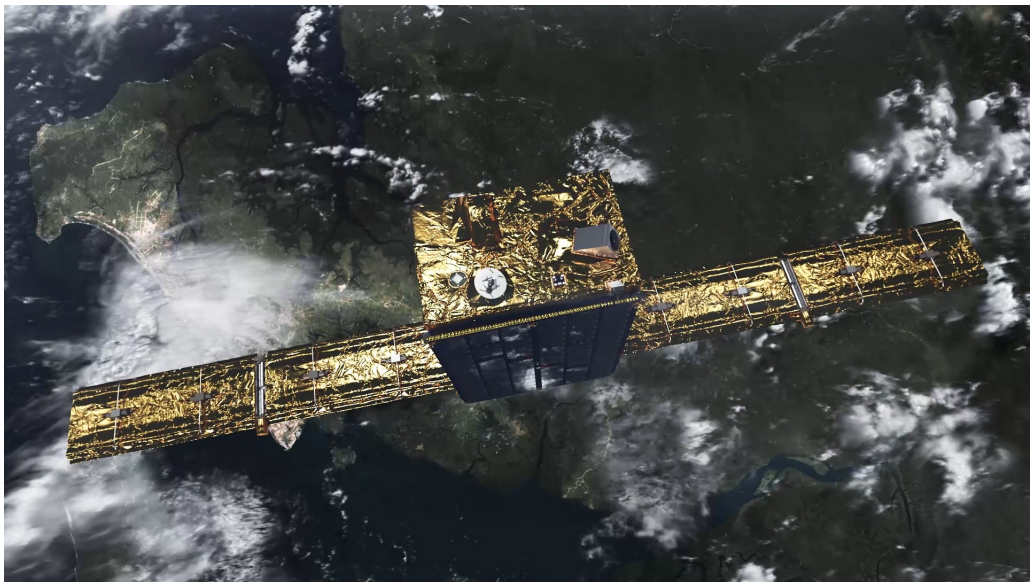

Figure 1.3: ICEYE-X1 launch render, Credits: ICEYE [1]

model for flexible spacecraft attitude dynamics, which captures the coupling effects between structural dynamics and attitude dynamics. Different spacecraft configurations are analysed, and the previously described mathematical model is derived for each of them. This allows the parameters that mainly impact the magnitude of the coupling effects between flexible and attitude dynamics to be established. An understanding of these aspects is crucial for generalising the procedure for estimating the significance of the coupling effect in other types of satellites.

The second part of this thesis is concerned with the design of a robust attitude control technique, i.e. the Quaternions Feedback Control (QFC), which is capable of handling external perturbations and dynamics uncertainties. The control strategy is tested in a three-degree-of-freedom orbital simulator that includes the mathematical model for attitude dynamics of the flexible spacecraft and the control algorithm. Extensive numerical simulations are performed in the Matlab/Simulink environment with the objective of studying the realisation of inertial pointing manoeuvres with different spacecraft configurations.

The results demonstrate that SAR panels exert a significant influence on the dynamics response of the spacecraft during attitude manoeuvres. This is most evident in the initial seconds of the simulation, when the transient excites the coupling between attitude and flexible dynamics and vibrations, reaching their maximum values. However, the QFC controller is shown to possess the capacity to counteract and nullify these disturbances by providing appropriate attitude control actions.

To sum up, this thesis is organized as follows: First the elements for attitude analysis are introduced, with a focus on attitude kinematics and dynamics presentation in sections 2.1 and 2.2. Additionally, the flexible spacecraft dynamics are introduced in this section. Subsequently, in section 2.3, the finite element method is described and analysis performed in this work is provided. In section 2.4, the generalities of Guidance-Navigation-Control system are given, along with an explanation of the rationale behind the choice of controller. The results of FEM analyses performed in MSC Patran/Nastran and the numerical simulations performed in Matlab/Simulink environment are in chapter 3. For each of the simulation scenarios described in section 2.3 and section 2.4, graphs of the most significant results obtained are provides, accompanied by comments and highlighting salient aspects. Finally, Conclusions are drawn in chapter 4.

Chapter 2

System mathematical model

This chapter describes the attitude of the satellite, introducing reference frames, parameters and elements to properly describe it. Then, the torques acting on the satellite are evaluated to understand how they manipulate the attitude dynamics, also a section will be regarded to a brief comparison between passive and active stabilization and the actuators needed. Moreover, the flexible-rigid coupling is introduced and described through the coupling matrix δ, which links attitude and flexible dynamics. In addiction, the main orbital perturbations are described. Then an overview about finite element method (FEM) and control laws is given, introducing the type of analysis performed and the control algorithm used for the orbital simulator.

2.1 Elements for spacecraft attitude analysis

The attitude of a spacecraft is its orientation in space as properly described in [7]. The problem of determining the orientation is crucial for every kind of space mission, from the Earth's observation missions to the deep space observation ones. To cope with attitude determination problem, it's firstly necessary to present the reference frames often used in spacecraft attitude analysis. Also, it's important to introduce the elements that allow the description of the attitude, i.e. the relative orientation between two reference frames.

2.1.1 Reference frames

The attitude of any spacecraft is usually described by relative orientation of a frame attached to the satellite and a second reference frame. Several frames can be used to express satellite orientation and position with respect to Earth [8], but only the most relevant for the goal of this thesis will be discussed here. To properly define a reference frame, the position of the origin and the orientation of the coordinate axes are needed.

Body Frame

The body frame is the reference system attached to the spacecraft. It is defined by an origin located at a specific point on the body and by three Cartesian axes.

A common simplification in attitude analysis is to make the body frame coincident with the central axes of inertia, in this way the satellite inertia tensor is diagonal. However, in real application, launch environment stresses, thermal gradients in orbits and displacements of satellite's appendages make difficult to properly characterize the behaviour of the center of mass and main axes of inertia.
Due to these reasons, it's common to first assume that the spacecraft is a rigid body, and then to add some uncertainties based to the case study.

Earth-Centered Inertial (ECI) frame

The Earth-Centered Inertial frame (ECI) is often used in spacecraft attitude analysis because many satellites are used for inertial pointing, this means that the orientation of such spacecraft with respect to the ECI frame must be kept constant. The Earth-Centered inertial frame has the ecliptic plane, i.e. the plane of Earth's revolution motion around the Sun, as fundamental plane. The fundamental axes are defined from the point where the ecliptic and equatorial plane cross. In particular, the origin of the frame coincide with Earth's center of mass and the X_I axis is defined at the vernal equinox with the positive direction pointing the Aries constellation. The Z_I, instead, is perpendicular to the equatorial plane and points towards the North Pole. Finally, Y_I completes the right tern.

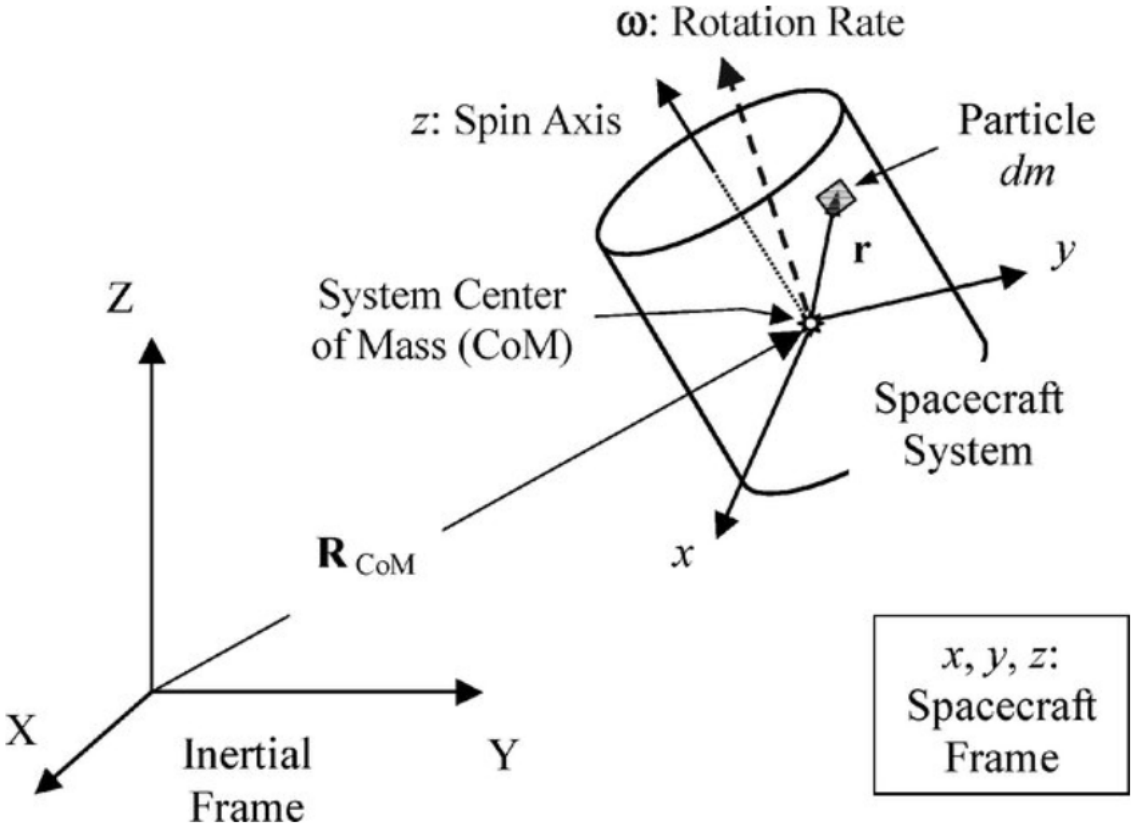

Figure 2.1: ECI and Body frames representation. Credits: [3]

A representation of both the body frame $\mathcal{F}_B$ and ECI frame $\mathcal{F}_I$ is given in Figure 2.1.

2.1.2 Quaternions and Euler angles definition

It has already been told that there are many ways to represent the attitude of a spacecraft. To properly conduct an attitude analysis, rotation matrices must be defined, because they specify the rotation that allows one reference frame to coincide with the other. For this purpose, a minimum of three parameters must be defined for a 3D rotation analysis. In the following, two attitude representations selected for this thesis are introduced. Finally, an appropriate method to evaluate attitude error is described.

Euler Angles

A common set of parameters used in attitude analysis is the Euler angles set.
As in [7], these angles express a rotation from an initial reference frame $\mathcal{F}_1$, with *ortho-normal* set of unit vectors $\mathcal{F}_{1_i}$, with $i = (x, y, x)$, to a second reference frame $\mathcal{F}_2$, defined by another set of ortho-normal unit vectors $\mathcal{F}_{2_i}$, as the product of three different rotations. It has to be underlined that those rotations are not commutative, so the rotation sequence influences the final configuration.

The rotation *(ψ,ϑ,φ)*, also named *3-2-1 rotation* or *Tait Bryant rotation*, is a commonly used rotation in aerospace. Three elementary rotations are applied as follows to let the frame $\mathcal{F}_2$ be aligned to $\mathcal{F}_1$:

1. Rotation ψ: positive rotation about Z_2, anti clockwise. An intermediate frame $\mathcal{F}_2^{'}$ is defined
2. Rotation θ: rotation about $Y_2^{'}$. Another intermediate frame is defined as $\mathcal{F}_2^{''}$
3. Rotation ϕ: rotation about $X_2^{''}$. Finally, $\mathcal{F}_1$ is obtained

In all rotation right handed reference frame are assumed. A representation of 3-2-1 rotation is shown in fig. 2.2.

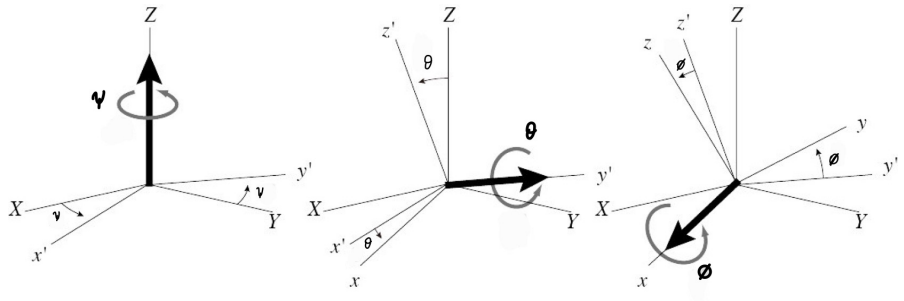

Figure 2.2: Tait-Bryant rotation representation

Each of the three rotations can be described by the following matrix formulation:

$$[\Psi] = \begin{bmatrix} cos(\psi) & -sin(\psi) & 0 \\ sin(\psi) & cos(\psi) & 0 \\ 0 & 0 & 1 \end{bmatrix}$$

$$[\Theta] = \begin{bmatrix} cos(\theta) & 0 & sin(\theta) \\ 0 & 1 & 0 \\ -sin(\theta) & 0 & cos(\theta) \end{bmatrix}$$

$$[\Phi] = \begin{bmatrix} 1 & 0 & 0 \\ 0 & cos(\phi) & -sin(\phi) \\ 0 & sin(\phi) & cos(\phi) \end{bmatrix}$$

The complete rotation matrix, for successive rotations, can be obtained by multiplying the rotation matrix in the reverse order of the rotation:

$$A_{21}(\Psi, \Theta, \Phi) =$$
$$\begin{bmatrix} cos(\theta)cos(\psi) & cos(\phi)sin(\psi) + sin(\phi)sin(\theta)sin(\psi) & sin(\phi)sin(\psi) - cos(\phi)sin(\theta)cos(\psi) \\ -cos(\theta)sin(\psi) & cos(\phi)cos(\psi) - sin(\phi)sin(\theta)sin(\psi) & sin(\phi)cos(\psi) + cos(\phi)sin(\theta)sin(\psi) \\ sin(\theta) & -sin(\phi)cos(\theta) & cos(\phi)cos(\theta) \end{bmatrix}$$

Quaternions

Even though the Euler's angles represent an intuitive way to describe the space orientation of a spacecraft, they could lead to many singularities. In the previous section, the 3-2-1 rotation has been introduced. For this set of angles, a singularity occurs when the Euler basis vectors are not linearly independent, so the orientation can not be unambiguously expressed (gimbal-lock). To avoid any kind of singularity, it can be necessary to add a redundant parameter to describe the rotation matrix. Quaternions allow to adopt a fully algebraic expression and allows to solve the singularity problem. The definition of the quaternions is based on the *Euler's Theorem*, which states that a fixed frame $\mathcal{F}_I$ can be rotate to any frame $\mathcal{F}_B$ by a rotation α, called *Euler's angle*, about an axis $\hat{a}$, called *Euler's axis*, that is fixed in both frame [7]. Euler's axis and Euler's angle are shown in fig. 2.3.

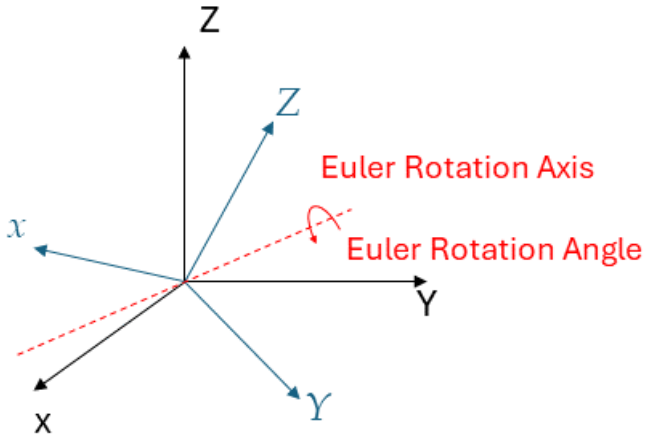

Figure 2.3: Euler's axis and rotation angle

Now, Euler's parameters, or quaternions, can be defined as follows.
Quaternions consist in a scalar part q_0 and in a 3D vectorial part $q_v = [q_1, q_2, q_3]^T$, as follows:

$$\begin{cases} q_0 = \cos\alpha/2 \\ q_1 = a_1 \sin\alpha/2 \\ q_2 = a_2 \sin\alpha/2 \\ q_3 = a_3 \sin\alpha/2 \end{cases} \tag{2.1}$$

The quaternion $\mathbf{Q}_I{=}(1,0,0,0)^T$ is usually referred to as the *unit quaternion*, and it represents the situation where the body frame is aligned with the inertial frame. This formulation is useful not only to avoid any singularity, but also because it represents a high computational efficiency method as it is purely algebraic and no trigonometric functions are used.

The rotation matrix of the previous subsection can be also given in quaternion terms as $\mathbf{A}_{21} = \left(q_0^2 - q_v^T \cdot q_v\right) I_3 + 2 q_v q_v^T - q_v^x$;
where:

- I_3 is the 3x3 identity matrix
- q_v^x is the skew matrix defined as follows:

$$q_v^x = \begin{bmatrix} 0 & -q_{v_3} & q_{v_2} \\ q_{v_3} & 0 & q_{v_1} \\ -q_{v_2} & -q_{v_1} & 0 \end{bmatrix}$$

In this thesis the Quaternions Feedback Control (QFC) is chosen as control law (section 2.4), so the quaternion error should be introduced. Since quaternions have a matrix representation, the quaternion error can not be computed as a simple difference, but it must be determined with matrix operations. Indeed, assuming that the current attitude of the spacecraft is indicated as $\mathbf{q}_{true}$, while the desired orientation is given by $\mathbf{q}_{Des}$, the attitude error is defined as follows:

$$\mathbf{q}_{err} = \mathbf{q}_{Des}^{-1} \bigotimes \mathbf{q}_{true}, \tag{2.2}$$

where $\otimes$ identifies the quaternion multiplication and the quaternion inverse is computed as:

$$\mathbf{q}^{-1} = \frac{q*}{||q||_2} = \frac{[q_0, -q_1, -q_2, -q_3]^T}{(q_0^2 + q_1^2 + q_2^2 + q_3^2)}, \tag{2.3}$$

where $q*$ is the quaternion conjugate, and $||q|| = 1$ due to the properties of attitude quaternions.

2.2 Attitude kinematics and dynamics

This section explores the attitude kinematics by performing the time derivatives of the attitude representations defined in the previous section. The equations for attitude kinematics express the time evolution of satellite attitude, and are focused on rotational motion without considering any torques. If torques are introduced, the field of study moves from attitude kinematics to attitude dynamics, and the satellite's angular momentum plays a fundamental role in relevant equations. Firstly, the assumption of rigid body is adopted and dynamics equations will be

derived as in [9]. Then, the flexibility of satellite appendages will be introduced according to the model proposed in [10]. Hence, the flexible-rigid coupling effect must be introduced and the mutual interaction between rigid and flexible dynamics must be analyzed, in order to perform a rigorous dynamics analysis. In the last subsection, the external disturbances considered in the model will be described.

2.2.1 Attitude kinematics

This subsection presents the time derivatives of Euler Angles and quaternions, introduced in subsection 2.1.2. The reference frames defined in subsection 2.1.1 are used for this purpose.
Let define:

- ω_e: angular velocity of $\mathcal{F}_B$ frame, with respect to the objective frame $\mathcal{F}_D$, in $\mathcal{F}_B$ coordinates
- ω_B: angular velocity of $\mathcal{F}_B$ relative $\mathcal{F}_I$, in $\mathcal{F}_B$ coordinates
- ω_D: angular velocity of an objective frame $\mathcal{F}_D$ relative to $\mathcal{F}_I$, in $\mathcal{F}_D$ coordinates

From the rule of composition of angular rates is known that they are additive, so ω_e can be obtain as:

$$\boldsymbol{\omega_e} = \boldsymbol{\omega_B} - A_{21}^T(\Theta_e)\boldsymbol{\omega_D}, \qquad or \qquad \boldsymbol{\omega_e} = \boldsymbol{\omega_B} - A_{21}^T(q_e)\boldsymbol{\omega_D} \tag{2.4}$$

Now the kinematics in terms of attitude representation can be described.

Attitude kinematics for Euler angles

Time evolution in terms of Euler angles for a 1-2-3 rotation is as follow:

$$\dot{\boldsymbol{\Theta}}_{\boldsymbol{e}} = \begin{bmatrix} \dot{\phi}_e \\ \dot{\theta}_e \\ \ddot{\psi}_e \end{bmatrix} = \frac{1}{cos(\theta_e)} \begin{bmatrix} c_{\psi_e} & -s_{\psi_e} & 0 \\ c_{\theta_e} s_{\psi_e} & c_{\theta_e} c_{\psi_e} & 0 \\ -s_{\theta_e} c_{\psi_e} & s_{\theta_e} s_{\psi_e} & c_{\theta_e} \end{bmatrix} \boldsymbol{\omega_e} = \boldsymbol{B(\Theta_e)\omega_e} \tag{2.5}$$

Where c_x and s_x are cosine and sine of the angle reported in the subscript "x", respectively.
The kinematics relationship in eq. (2.5) is not linear and the components are coupled. However, for small attitude errors $\Theta_e \approx 0$, $\boldsymbol{B(\Theta_e)} \approx \boldsymbol{I_3}$ can be considered, which realizes a linear model for attitude kinematics.

Attitude kinematics for quaternions

The time evolution of the attitude error in terms of quaternions for a 1-2-3 rotation is as follow:

$$\dot{\boldsymbol{q}}_{\boldsymbol{e}} = \frac{1}{2} \left(q_{e_0} I_4 + \begin{bmatrix} 0 & q_{e_\nu}^T \\ q_{e_\nu} & q_{e_\nu}^\times \end{bmatrix} \right) \begin{bmatrix} 0 \\ \omega_{e_1} \\ \omega_{e_2} \\ \omega_{e_3} \end{bmatrix} \tag{2.6}$$

Like in the previous subsection, the kinematics equations are coupled, but with the hypothesis of small attitude error, i.e $q_e \approx (1, 0, 0, 0)^T$, eq. (2.6) reduces to the following linear equation:

$$\dot{q}_{e_i} = \frac{1}{2}\omega_{e_i}; \qquad i = x, y, z \tag{2.7}$$

2.2.2 Attitude dynamics

This subsection aims to underline the fundamental role of the angular momentum in attitude dynamics analysis, as in [9]. Moreover, the rotational dynamics of the rigid spacecraft will be presented by deriving relations between the time evolution of the angular rate of the satellite and internal or external forces and torques. Firstly, definitions of angular momentum and center of mass of a collection of mass points are given. Then, the attitude dynamics of the rigid spacecraft, referring to the body frame as defined in section 2.1.1 is analyzed. Since the control laws in this work consider the momentum exchange devices (reaction wheels RWs), a short description of those actuators will be included in this subsection.

Angular momentum

We consider a spacecraft to be made up of a collection of n point masses. The angular momentum with respect to the origin *0* of an inertial coordinate frame is defined in terms of masses m_i, position $\boldsymbol{r}^{i0}$ and velocities $\boldsymbol{v}^{i0} = \dot{\boldsymbol{r}}^{i0}$ of a certain point to 0 as follow:

$$\boldsymbol{H}^0 = \sum_{i=1}^{n} \boldsymbol{r}^{i0} \times m_i \boldsymbol{v}^{i0} \tag{2.8}$$

Figure 2.4 show the center of mass c and two representative mass point. From Newton's second

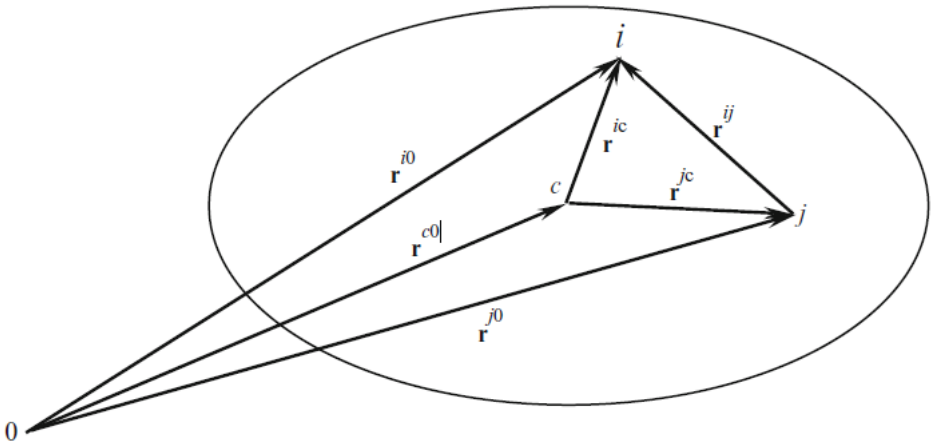

Figure 2.4: Center of mass representation

law, considering an inertial frame, the derivative equation from eq. (2.8) is:

$$\dot{\boldsymbol{H}}_I^0 = \sum_{i=1}^{n} \boldsymbol{r}_I^{i0} \times \boldsymbol{F}_I^i = \sum_{i=1}^{n} \boldsymbol{r}_I^{i0} \times \left(\sum_{j=1}^{n} \boldsymbol{F}_I^{ij} + \boldsymbol{F}_I^{i-ext} \right) \tag{2.9}$$

Where $\boldsymbol{F}_I^{ij}$ is the force exerted on mass point i by mass point j and $\boldsymbol{F}_I^{i-ext}$ is the force exerted on i by everything external to the system of mass points. In the assumption of force between two mass points acting only along the line between them, the cross product vanishes and

$$\dot{\boldsymbol{H}}_I^0 = \sum_{i=1}^{n} \boldsymbol{r}_I^{i0} \times \boldsymbol{F}_I^{i-ext} = T_I^0 \tag{2.10}$$

where T_I^0 is the net torque about 0 exerted on the collection of mass points by all external forces. The center of mass of n mass point is defined as:

$$\boldsymbol{r}^{c0} = \frac{\sum_{i=1}^{n} m_i \boldsymbol{r}^{i0}}{M} \tag{2.11}$$

where $M = \sum_{i=1}^{n} m_i$ is the total mass of the collection of mass points. From that definition follows:

$$\sum_{i=1}^{n} m_i \boldsymbol{r}^{ic} = \sum_{i=1}^{n} m_i \left(\boldsymbol{r}^{i0} - r^{c0}\right) = 0 \tag{2.12}$$

Using this result and its derivative in eq. (2.8) we can obtain:

$$H^0 = \sum_{i=1}^{n} m_i \left(\boldsymbol{r}^{ic} + r^{c0}\right) \times \left(\boldsymbol{v}^{ic} + \boldsymbol{v}^{c0}\right) = \boldsymbol{H}^c + \boldsymbol{r}^{c0} \times M\boldsymbol{v}^{c0} \tag{2.13}$$

This equation states that the angular momentum about a point 0 can be written as the sum of the angular momentum about the center of mass and the angular momentum of the center of mass motion [9]. The net torque can similarly be written as:

$$\boldsymbol{T}^0 = \boldsymbol{T}^c + \boldsymbol{r}^{c0} \times \boldsymbol{F} \tag{2.14}$$

where $\boldsymbol{F}$ is the net external force on the mass points. Finally, in an inertial frame, we have $\boldsymbol{F}_I = M\dot{\boldsymbol{v}}_I^{c0}$, so putting eq. (2.13) and eq. (2.14) in eq. (2.10), we obtain the *Euler's Equation*:

$$\dot{\boldsymbol{H}}_I^c = \boldsymbol{T}_I^c \tag{2.15}$$

This is the fundamental equation of the attitude dynamics.

Rigid body dynamics

We now focus on the rigid body dynamics. A rigid body is defined by a body frame $\mathcal{F}_B$, where all the vectors $\boldsymbol{r}_B^{ic}$ previously defined are constant. We consider a body frame centred in the center of mass and with the axes aligned with the central axes of inertia. Then, the angular momentum in $\mathcal{F}_B$ frame is:

$$H = [J]_B \omega_B \tag{2.16}$$

where $[J]_B \in \mathbb{R}^{3x3}$ is the inertia tensor in $\mathcal{F}_B$, and is defined as follow:

$$[J]_B = \begin{bmatrix} J_{xx} & 0 & 0 \\ 0 & J_{yy} & 0 \\ 0 & 0 & J_{zz} \end{bmatrix}$$

The hypothesis of rigid body allows to consider $[J]_B = const$. The attitude dynamics of a rigid spacecraft is described by Euler's equation for the rotational dynamics and its form depends on the type of actuators installed on board. If the satellite has not momentum exchange device, the total angular momentum H is as in eq. (2.16), and its time derivative is:

$$\dot{\boldsymbol{H}}_B = J_B \dot{\omega}_B \tag{2.17}$$

Then we can write the Euler's equation for rotational dynamics for rigid body as:

$$J_B \dot{\omega}_B = m - \omega_B \times J_B \omega_B \tag{2.18}$$

where $m = d + u$ is the external torque acting on the spacecraft, consisting of both orbital disturbances d and control torques u. Devices providing an external torque, like thruster or magnetorquers, are named *reaction actuators*, they control spacecraft attitude by modifying the overall angular momentum of the system. Momentum exchange device will be described deeper in next subsection, now let us focus in writing dynamics equation when reaction wheels are equipped.

The total angular momentum is given by the sum of the angular momentum of the rigid body (eq. (2.16)) and the angular momentum of the wheels relative to the body h_{RW}:

$$H = J_B\omega_B + h_{RW} \tag{2.19}$$

In the design of attitude control algorithms we consider three reaction wheels aligned with the three central axes of inertia. The conservation of angular momentum in an isolated system let us consider:

$$\dot{H}_B = J_B\dot{\omega}_B + \dot{h}_{RW} \tag{2.20}$$

allowing to obtain the Euler's equation in case of reaction wheels device as:

$$J_B\dot{\omega}_B = m - \omega_B \times (J_B\omega_B + h_{RW}) - \dot{h}_{RW} \tag{2.21}$$

Reaction wheels

Reaction wheels (RWs) secure three-axis stabilisation without thruster or any other kind of external torques generators, and provide an high precision control. They allow to control spacecraft attitude by re-distributing angular momentum between the wheels themselves and the main body. In this subsection, the assumptions in [12] are considered: no reaction type actuators (u=0), free from orbital perturbations (d=0), thus to have m=0 in eq. (2.21) and *H=const.* Moreover, let us assume that the initial conditions of the system are $\omega_0 = 0$ and $h_{RW_0} = 0$, so $H(t) = 0 \ \forall t$. These assumptions lead to the following relation:

$$J_B\omega(t) = -h_{RW}(t) \quad \forall t \tag{2.22}$$

This equation reveals that if an electric motor is switched on to power the wheel to which it is linked, then the spacecraft body begins to counter-rotate for conservation of angular momentum. This is illustrated in fig. 2.5.

Reaction wheels certainly give many benefits, as the already underlined high pointing accuracy, the saving costs due to avoiding propellant, which also allow a significant reduction for payload fraction, and the autonomous active three-axis stabilization. On the other hand, there are some issues regarding the performances that RWs can offer. The maximum rotational rate of the wheel, which is linked to the maximum angular momentum $\overline{h}_{RW} \in \mathbb{R}$ stored into a wheel, depends on structural constraints. Secondly, the torque exchanged between the wheels and the spacecraft is developed by an electric motor. Therefore, the torque is related to electrical power required to sustain the motor, this leads to a saturation value $\overline{\tau}$ on the maximum torque supplied. These consideration lead to the conclusion that control laws must ensure specific conditions in order to avoid saturation:

$$\tau_i \in [-\overline{\tau}, \overline{\tau}], \ \ h_{RW_i} \in [-\overline{h}_{RW}, \overline{h}_{RW}]; \quad i = x, y, z. \tag{2.23}$$

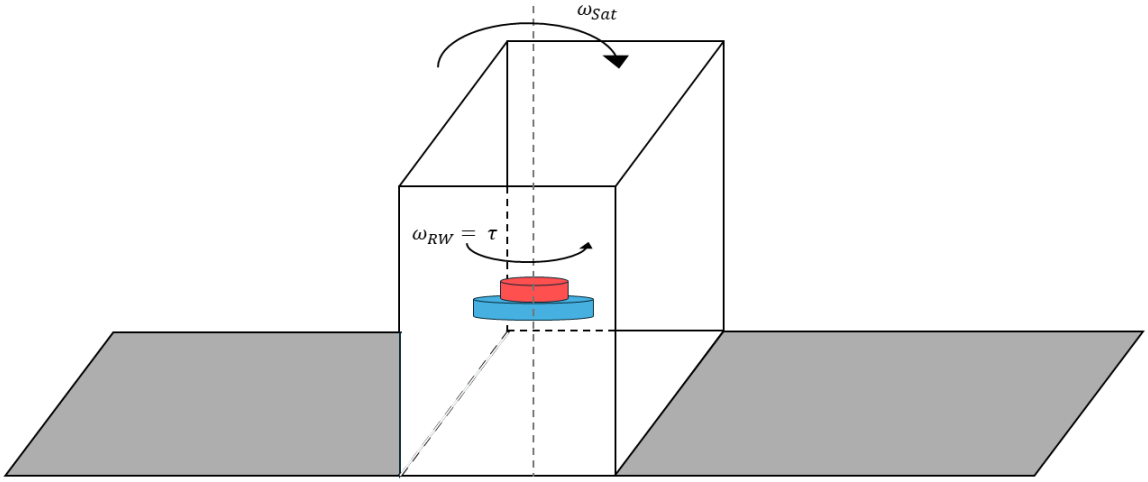

Figure 2.5: Attitude control scheme with reaction wheels actuator

The angular momentum saturation condition consists in the impossibility to store any more angular momentum. Considering the eqs. (2.22) and (2.23), also recalling the assumption in [12] allows to decouple the three channels of attitude dynamics equations, the angular momentum saturation is avoided if the following hold:

$$\overline{h}_{RW} \leq (J_B\omega)_i \leq \overline{h}_{RW} \implies$$

$$\implies -(J_B^{-1}(\overline{h}_{RW}\mathbf{1}_3))_i = -\overline{\omega}_i \leq \omega_i \leq \overline{\omega}_i = (J_B^{-1}(\overline{h}_{RW}\mathbf{1}_3))_i \tag{2.24}$$

In real application, RWs are used not only to manoeuvre the spacecraft, but also to balance external perturbations to maintain the desired attitude. This lead to a surplus of angular momentum absorbed by RWs and may cause saturation. To this end, spacecrafts with RWs devices must be equipped with reaction-type actuators too, for de-saturation process.

2.2.3 Flexible spacecraft

This subsection introduces the problem of flexibility in lightweight structures. Now a days, spacecrafts are usually equipped with lightweight, flexible, store-able and deploy-able antennas, solar panels or booms [13]. These flexible appendages represent a challenge in control performance since they introduce many uncertainties. Firstly, the flexible dynamics equations are introduced and linked with the attitude dynamics through the coupling matrix δ. Then, the attitude dynamics equations are integrated with the contributions due to structure-flexibility.

Flexible dynamics

The elastic deformations of such large appendages result in a disturb for satellite bus attitude, but are also influenced by it. This thesis considers the rigid-flexible coupling effect using the hybrid-coordinates method, as proposed in [10], that considers a combination of discrete coordinates and the modal superposition to define a mathematical model for the flexible appendages.

Consequently, a modal FEA is needed, and it is crucial to compute the modal shapes as better as possible.

The main assumption to properly obtain the equations of motion is the small deformation hypothesis. Another important aspect of this thesis is the modelization of the flexible structure, consisting in the four SAR panels of the satellite defined in section 1.2, as a collection of n elastically interconnected, discrete and rigid sub-panels. The next step is evaluating the natural modes through the FEM modal analysis, obtaining the natural frequencies and the relative eigenvectors associated to each mode. These data are used to compute the δ matrix for every panels taken into account. A better explanation about the finite element method and analyses is given in section 2.3. The general equations of motion for an undamped structure are expressed as a function of the stiffness matrix **K** and the mass matrix **M** as follows:

$$M\ddot{\nu} + K\nu = 0, \tag{2.25}$$

where ν stands for the flexible displacement vector. In a linear system, where the free vibrations are harmonic, ν is defined as:

$$\nu = \Phi e^{i\Omega t} = \Phi\eta, \tag{2.26}$$

where Φ is the matrix of eigenvectors, Ω are the natural frequencies and η is the modal coordinate vector.
The eigenvectors and the frequencies are linked to a specific natural mode. Substituting the eq. (2.26) in eq. (2.25) and doing the necessary algebraic passages, the classical eigenvalue problem is obtained, and the equation becomes:

$$(K - \lambda M)\,\Phi = 0, \tag{2.27}$$

where λ is the eigenvalue for each mode.

In this thesis FEM software Patran/Nastran was used to solve the eq. (2.27). Also, under the assumption of small deformation, the dynamics equation of the modal coordinate vector η for the flexible appendage attached to the spacecraft is as follows:

$$\ddot{\eta} + D\dot{\eta} + K\eta = -\delta\dot{\omega}, \tag{2.28}$$

where $K, D \in \mathbb{R}^{N\times N}$, with N the number of natural modes considered to build Φ, and $\eta \in \mathbb{R}^N$ is the modal coordinate vector. The stiffness matrix K is diagonal matrix and it is composed by model natural frequencies, so it is as:

$$K = \begin{bmatrix} \Omega_1^2 & \dots & 0 \\ \vdots & \ddots & \vdots \\ 0 & \dots & \Omega_n^2 \end{bmatrix},$$

since the dumping effect is hard to consider without empirical test, the dumping matrix D is calculated from the stiffness matrix by a scalar factor α, so $D = \alpha \cdot K$.

Equation (2.28) shows that the dynamics response depends on a term proportional to angular acceleration $\dot{\omega}$ of the system by the coupling matrix δ.
In the following section, the effects of structure flexibility in angular momentum pf the spacecraft are presented.

Coupling matrix δ

The coupling matrix δ expresses the interaction between rigid body attitude dynamics and flexible appendages. The assumption of uncoupled attitude and structure dynamics, frequently used in many case studies, is not suitable when structures are not stiff enough. Therefore, the coupled equations must be compared to Euler's equation defined above. At this aim, this paragraph is focused to the definition and computation of the matrix δ. As in [10], the coupling matrix $\delta \in \mathbb{R}^{N\times 3}$ is as follow:

$$\delta = -\Phi^T M \left(\Sigma_{0I} - \Sigma_{I0}\tilde{R} - \tilde{r}\Sigma_{I0}\right) \tag{2.29}$$

where:

- Φ is a matrix composed by sub-panels eigenvectors
- M is the mass matrix composed as follows:

$$M_i = \begin{bmatrix} m_{sub}I & \mathbf{0} \\ \mathbf{0} & m_{sub}I \end{bmatrix}$$

  with I 3×3 identity matrix and m_{sub} mass of the sub-panel
- Σ_{I0} and Σ_{0I} are $\mathbb{R}^{6N\times 3}$ operator defined as:

$$\Sigma_{0I} = \begin{bmatrix} \Sigma_{0I_i} \\ \vdots \\ \Sigma_{0I_n} \end{bmatrix} \quad ; \quad \Sigma_{I0} = \begin{bmatrix} \Sigma_{I0_i} \\ \vdots \\ \Sigma_{I0_n} \end{bmatrix},$$

  where Σ_{0I_i}=$[\mathbf{0}_3; \mathbf{I}_3]$, Σ_{I0_i}=$[\mathbf{I}_3; \mathbf{0}_3]$, with $\mathbf{0}_3$, $\mathbf{I}_3 \in \mathbb{R}^{3\times 3}$ null and identity matrices, respectively.
- R is the vector between the center of mass of the rigid hub and the flexible appendages interface. The ~ stands for the skew-symmetric 3×3 matrix. A visualization is given in fig. 2.6a.
- r is the vector between the flexible appendage interface and the COM of each sub-panels, as better defined in fig. 2.6b.

Attitude dynamics

Now it is possible to modify the eq. 2.19 in order to derive the attitude dynamics equation for the flexible satellite. It can be demonstrated that the flexibility of the appendages adds a term to the total angular momentum, that is:

$$H_{Flex} = \delta^T \dot{\eta}, \tag{2.30}$$

thus the total angular momentum becomes:

$$H = J\omega + h_{rw} + \delta^T \dot{\eta} \tag{2.31}$$

Finally, the complete attitude dynamics equation is obtain from eq. 2.20 by determining the time derivative of the equation 2.31 above, this results in:

$$J\dot{\omega} = m - \omega \times \left(J\omega + h_{rw} + \delta^T \dot{\eta}\right) - \dot{h}_{rw} - \delta^T \ddot{\eta} \tag{2.32}$$

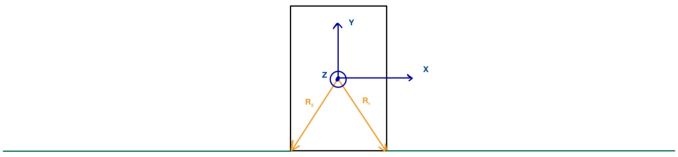

(a) Visualization of R vector

(b) Visualization of sub-panels division and r vector definition

Figure 2.6: Visualization of different elements in δ matrix

2.2.4 Orbital disturbances

This subsection aims to introduce the main orbital disturbances usually considered in attitude and orbit control system, for further information refer to [4, 9]. Orbital perturbation has been considered in the previous equations as the disturbance torque d, but indeed it is composed by many terms, and they arise from the environment in which the spacecraft operates. In an Earth mission scenario the most relevant perturbation torques are the magnetic torque, the solar radiation pressure torque, the aerodynamic drag torque and the gravity gradient torque. These orbital disturbances are implemented in orbital simulator as external torques, applying the models described in the following sections. A summary of orbital perturbations based on mission profiles are illustrated in figure 2.7.

Gravity gradient torque

Any non-symmetrical rigid body in a gravity field is subject to a gravity gradient torque, which is due to the quadratics decrease of Earth gravitational force with the distance from its center. Therefore, not all parts of a spacecraft experience equal force, this results in a disturbance effect. The gravity gradient torque increases with the angle between the local vertical and spacecraft's principal axes, trying to align the minimum principal axis with the local vertical. A simplified expression for the gravity gradient torque for a spacecraft with the minimum axis aligned to local vertical is:

$$d_g = \frac{3\mu}{|r|^5} r \times J_b r \tag{2.33}$$

where:

- μ is Earth gravitational parameter
- r is the orbital position of the spacecraft center of mass

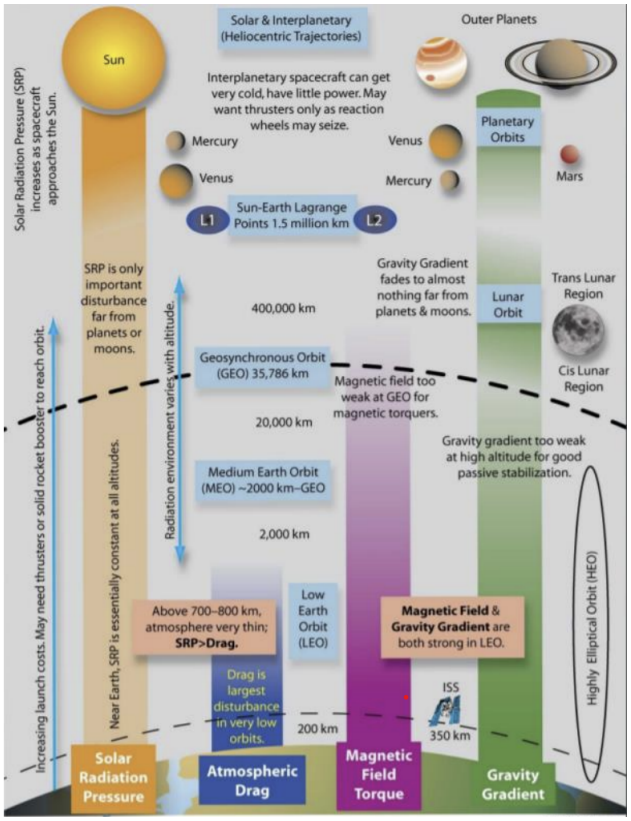

Figure 2.7: Effects of major environmental disturbances on spacecraft attitude control system design [4]

- J_B is the spacecraft inertia matrix

Magnetic Torque

The magnetic torque derives from the interaction between the Earth's magnetic field and the equivalent magnetic dipole of the satellite, resulting from electronic devices on board. When the spacecraft dipole is not aligned with the local magnetic field, it experiences a magnetic torque that try to align the magnet to the local field. Earth's magnetic field modeling is complex, because it is asymmetric, not aligned with Earth's spin axis, varies with both geographical movement of the dipole and changes in solar particle flux. However, for attitude determination and control system (ADCS) we can consider it as a dipole and determinate the maximum possible value for a certain orbit altitude. The disturbance torque is:

$$d_m = m \times b \tag{2.34}$$

where:

- m is the spacecraft magnetic dipole moment
- b is the Earth's magnetic field

Solar radiation pressure torque

Sunlight has momentum, and therefore it exerts pressure on those objects it strikes. If an object absorbs all the sunlight incising on it, then all of its momentum is absorbed too. This causes a certain pressure force directed towards the optical center of pressure of the satellite and it produces a torque around the center of mass of the spacecraft if this one does not coincide with the optical center of pressure. Moreover, if the spacecraft completely reflects the sunlight, this pressure is twice as much as the first case. The magnitude of solar radiation changes due to Solar activity, due to seasonal variations according to Sun's cycles, ans it must be consider in high orbits (≥ 800 km), since in low-Earth orbits (LEO) aerodynamics is usually dominant, while it is zero when the spacecraft orbits in shadow condition. Now let us consider the spacecraft in sun's light, the torque d_s can be obtained as follow:

$$d_s = -p\left[c_{ps}\int_{S_{la}}(n\cdot s)dS\right]\times s, \tag{2.35}$$

where:

- p is the solar radiation pressure
- S_{la} is the spacecraft lit area normal to sun unit vector
- s is the sun unit vector directed from the sun towards the spacecraft
- c_{ps} is the distance between body center of mass and optical center of pressure

However, as underlined in [9], this formulation has several limitations, first of all because the Sun is not the only source of radiation, and in many case the light from Earth and Moon, namely *albedo*, can be significant; secondly the thermal radiation emitted from the spacecraft (to assure long-term energy balance) has been ignored. Anyway, for this study the formulation in eq 2.35 is accurate enough.

Aerodynamic drag torque

The atmospheric density is an exponential decaying function of altitude, so generally only spacecraft in LEO encounter enough particles to cause relevant disturbances. When the center of mass of the satellite and the center of atmospheric pressure, determined by the area exposed to the atmosphere in the direction of orbital velocity, are not aligned, a torque d_A results, namely aerodynamic torque. It can be estimated as:

$$d_A = c_{pa}\times\left(-\rho_A\nu\int_{Sfa}(n\cdot\nu)dS\right) \tag{2.36}$$

where:

- ν is the impact velocity between molecules and satellite, and it is assumed equal to the satellite's translation velocity
- S_{fa} is the spacecraft surface facing the flow
- n is the unit vector normal to the surface element dS
- ρ_A is the atmospheric density
- c_{pa} is the distance between the center of mass and the center of aerodynamic pressure.

2.3 Finite element method and analysis

In this section an overview about finite element method (FEM) and analysis (FEA) is given. The latter are effective tools for validating the design before entering the production phase. FEM is a mathematical model made of nodes and element that can be scalar, 1D, 2D and 3D. The goal of modeling is to obtain a model as representative as possible of the physics one. Therefore, this chapter first gives an overview on the generalities of finite element method. Then it details the elements, constraints and the type of finite element analysis used in this thesis for modeling the flexible structure. Finally, the FEM model is presented with its geometry, material properties, mesh and hinge modeling for any spacecraft configuration studied. Then the analysis parameters will be introduced.

2.3.1 Introduction to Finite Element Method

The Finite Element Method (FEM) is a numerical technique used to find approximate solutions to complex problems governed by differential equations, particularly in areas like structural analysis, heat transfer, fluid dynamics, and electromagnetism. In this thesis the structural analysis is considered. In this case, it works by breaking down a continuous domain, such as a physical structure, into smaller, discrete subdomains called *finite elements*. These elements can take various shapes, including triangles, quadrilaterals, tetrahedra, or hexahedra, depending on the problem's dimensionality. Each element is associated with nodes, specific points at which the governing equations are evaluated. The relationship between these nodes is defined through interpolation functions, often referred to as shape functions, which approximate the solution across the element. The governing equations, typically in the form of differential equations, are converted into an algebraic system using techniques like the Galerkin method or weighted residuals. This process is known as discretization [14, 15]. A key strength of FEM lies in its ability to model complex geometries, as the mesh of elements can conform to irregular shapes and boundaries. Additionally, FEM can handle varying material properties within the domain, apply different types of boundary conditions, and work effectively in multi-physics scenarios (e.g., coupled thermal-structural analyses). Once the problem is discretized, the resulting system of equations is typically large but sparse, which can be efficiently solved using numerical methods like direct solvers (LU decomposition) or iterative solvers (conjugate gradient method).
The FEM solution process involves several steps

1. Pre-processing
2. Formulation
3. Assembly
4. Solving
5. Post-processing

FEM's precision depends on the size and quality of the mesh. A finer mesh generally yields more accurate results but at the cost of increased computational effort. Adaptive meshing, where the mesh is refined in regions of high gradients, can improve accuracy while keeping computational demands manageable.

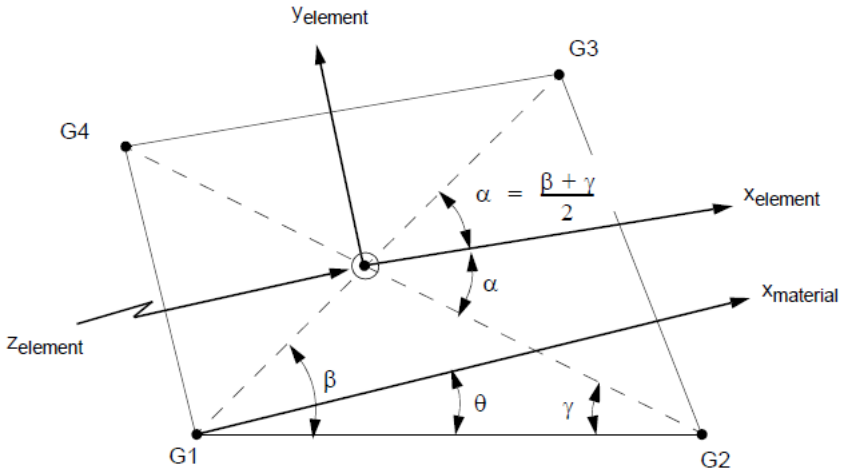

Figure 2.8: CQUAD4 element geometry and coordinate systems. [5]

1	2	3	4	5	6	7	8	9	10
PSHELL	PID	MID1	T	MID2	$12I/T^3$	MID3	TS/T	NSM	
	Z1	Z2	MID4						

Figure 2.9: PSHELL bulk data entries. [5]

To sum up, FEM is a versatile and efficient tool for solving a wide range of physical and engineering problems, offering flexibility in modeling complex structures and materials under various conditions. Now, an overview about finite element method has been proposed, so the model used in this thesis can be presented.

The spacecraft model is constituted by 2D elements. In the following, the various 2D elements available in MSC Patran/Nastran are defined:

- **CSHELL**: these elements can be further divided in two groups, based on the number of points they are composed of: *CQUAD* and *CTRIA*. The former can be defined as *CQUAD4* or *CQUAD8*, while the latter as *CTRIA3* or *CTRIA6*. The number stands for the grid points defined for each element, it is usually more difficult to mesh CQUAD8 and CTRIA6 elements, so they are not commonly used. Moreover, CTRIA elements are used to mesh irregular shapes. These elements allow to simulate any type of plates trough the definition of the right properties. The material properties for CQUAD and CTRIA elements are specified with the PSHELL or PCOMP entries, where PCOMP is only used for composite. The Bulk Data entry for PSHELL element is reported in fig. 2.9, where the *MID* entries stand for material identification:
  1. MID1: material identification number for the membrane
  2. MID2: material identification number for bending
  3. MID3: material identification number for transverse shear
  4. MID4: material identification number for membrane-bending coupling
- **CSHEAR**: these elements can be used when the bending and axial stiffness of the plate are negligible. CSHEAR elements can only handle in-plane loads, therefore they are usually implemented to simulate thin skin panels

Name	**Description**	**m**
RBE2	This MPC, only a single master node can be defined, while it is possible to have multiple slave dependent ones. It is used to simulate a rigid connection. The independent degrees of freedom are the six components of motion at the grid point. The dependent degrees of freedom at the other grid point can be selected by the user instead.	m≥1
RBE3	This kind of elements defines a constraint in which motion at a specific grid point is the least square weighted average of the motion of other grid points [5].	1≤m≤6
RBAR	Simulate a rigid bar connection with six degrees of freedom at each end.	1≤m≤6
EXPLICIT	it is the most customarily by the user. It is a rigid body connection to an arbitrary number of grid points. Furthermore, the independent and dependent degrees of freedom can be freely selected.	m≥1

Table 2.1: MPCs element in MSC Nastran

Since the panels in a satellite's structure must face the harsh space environment and internal and external loads, the CSHELL element are chosen. Since, the geometry of ICEYE-X1 is composed by regular prism, CQUAD4 elements type have been used.

Another important aspect of this thesis is the modeling of the link between the rigid hub and SAR panels. In the real scenario, panels are linked trough hinges, which allow the correct deployment of the antenna. Multi-Point-Constraints (MPC) are the main solution that can be used in FEM to simulate these devices. Basically, MPC allows to de-couple a specific DOF from others, while defining a relation between two or more DOFs. At this aim, it is necessary to define the main node(s), usually called *master*, and the secondary one(s), usually called *slave*. According to this master-slave relationship, many MPCs can be defined and different number of constraint equations (m) are generated. A summary is reported in table 2.1.

2.3.2 Modal Analysis

Modal analysis of flexible structure is one of the most common applications of finite element modeling. This analysis is one of the most important in space industry, because it evaluates the natural frequencies and the mode shapes of the structures, allowing to verify if any resonance phenomenon occurs and to determine the response of the body when subjected to dynamic loads. Modal analysis can be done in various conditions, basing on the needs of the user. In this thesis, a free-free condition is considered in order to determine natural frequencies when no loads or constraints are considered [17].

The frequencies obtained from the FEM analysis when considering a free and non-damped system (i.e $F(t) = 0$ and $\zeta = 0$) are called natural frequencies. In this situation, the inertial forces and the elastic ones are perfectly balanced. The deformation that the body is subjected to when vibrating at one of those frequencies, is called mode shape. In particular, a mode shape is associated to each natural frequency.

Natural frequencies and mode shapes can be easily illustrated by considering the equivalent *mass-spring* system in fig. 2.10.
For this system, the equation of motion can be written as:

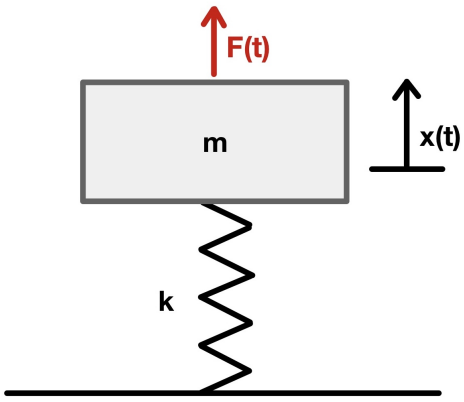

Figure 2.10: Example of a mass-spring system

$$m\ddot{x}(t) + kx(t) = F(t) \tag{2.37}$$

The solution of the differential equation eq. (2.37) is the sum of a particular solution $x_p(t)$ and the solution of the associated homogeneous equation $x_0(t)$, i.e. $x(t) = x_0(t) + x_p(t)$ with:

$$x_0(t) = A\sin\omega t + B\cos\omega t \tag{2.38}$$

Substituting eq. (2.38) into eq. (2.37) and considering $F(t) = 0$, it is obtained as follows:

$$-mA\omega^2\sin\omega t - mB\omega^2\cos\omega t + kA\sin\omega t + kB\cos\omega t = 0 \implies$$

$$\implies A(k - m\omega^2)\sin\omega t + B(k - m\omega^2)\cos\omega t = 0 \tag{2.39}$$

From eq. (2.39), natural frequency can be defined:

$$\omega_n = \sqrt{\frac{k}{m}} \tag{2.40}$$

In finite element method, modal analysis is conducted by resolving the eq. (2.37) in matrix form, as introduced in chapter 2, eq. (2.25):

$$[M]\{\ddot{x}\} + [K]\{x\} = 0 \tag{2.41}$$

It has been already said that this system allows harmonic solution, as:

$$\{x(t)\} = \{\Phi\}e^{i\omega_n t} \tag{2.42}$$

Therefore, eq. 2.41 can be rewritten as:

$$-\lambda[M]\{\Phi\}e^{i\omega_n t} + [K]\{\Phi\}e^{i\omega_n t} = 0, \tag{2.43}$$

where $\lambda = \omega_n^2$ is the eigenvalue and $\{\Phi\}$ the associated eigenvector or mode shape.
Finally, the classic eigenvalue problem can be presented:

$$([K] - \lambda[M])\{\Phi\} = 0 \tag{2.44}$$

It is possible to define the physical displacement as a combination of all its normal modes as:

$$\{x\} = \sum_i (\Phi_i)\xi_i \tag{2.45}$$

Assuming that $[M]$,$[K] \in \mathbb{R}^{N\times N}$ and both symmetric, so that the properties reported in table 2.2 hold. Therefore, the i^{th} generalized mass and stiffness can be defined. The first two

Property		
1.	$\{\Phi_i\}^T$[M]$\{\Phi_J\}$=0	if i≠j
2.	$\{\Phi_i\}^T$[K]$\{\Phi_J\}$=0	if i≠j
3.	$\{\Phi_i\}^T$[M]$\{\Phi_J\}$=m_i	if i=j
4.	$\{\Phi_i\}^T$[K]$\{\Phi_J\}$=k_i=$\omega^2 m_i$	if i=j

Table 2.2: Normal mode's proprieties

relation in tab. 2.2 are known as the orthogonality property of normal modes, ensuring that each mode is distinct from all other, that means that each mode shape can not be obtained through a linear combination of any other mode shapes [5]. While the other lead to the Rayleigh's equation, which is used to compute natural frequencies in MSC Nastran solver.

$$\omega_i^2 = \frac{\{\Phi_i\}^T[K]\{\Phi_i\}}{\{\Phi_i\}^T[M]\{\Phi_i\}} \tag{2.46}$$

2.3.3 FEM Model and Analysis setting

Since the main goal of this thesis is to develop an orbital attitude simulator, the satellite needs to be modelled in its operative configuration, with all the SAR's panels deployed. Furthermore, the model wants to simulate the satellite during its space flight, so when no constraint conditions are present. For this reason the modal analysis has been considered in free-free condition. The initial idea for this thesis was to evaluate if any difference occurs when the flexible appendages are considered as monolithic panels and when a connection interface is modeled. Indeed, the hinges, that guarantee the correct deployment sequence, leave specific DOF free to allow the relative motion between the various parts of the satellite's structure.

Firstly, let introduce the geometry and proprieties of the model without any interface between the rigid hub, the flexible panels, and these panels themselves. In this way, the -y face (according to MSC Patran reference frame) is composed by the base of the main structure and the four flexible SAR's panels, as shown in fig. 2.11. As said in section 1.2, the launch configuration is 70 cm in height × 60 cm in width, so the third dimension is not given. However, after

many investigation of similar satellite configuration and micro-satellite class, a deep of 40 cm has been assumed.
The model has been realized with 2D CSHELL QUAD4 elements, since the shapes of various components are regular and easy to mesh with this kind of elements. The typical materials for satellite's structure are aluminium alloy, in particular *Al 5062*, *6061* and *7075*. In a production process, it is important to take into account various parameters basing on the mission purpose, some purely mechanic while others relative to manufacturability or thermal behaviour. Since in this project the objective is not to produce a satellite, the most common alloy was chosen for modeling ICEYE-X1 structure, which is Aluminium 7075 alloy, whose features are in table 2.3.

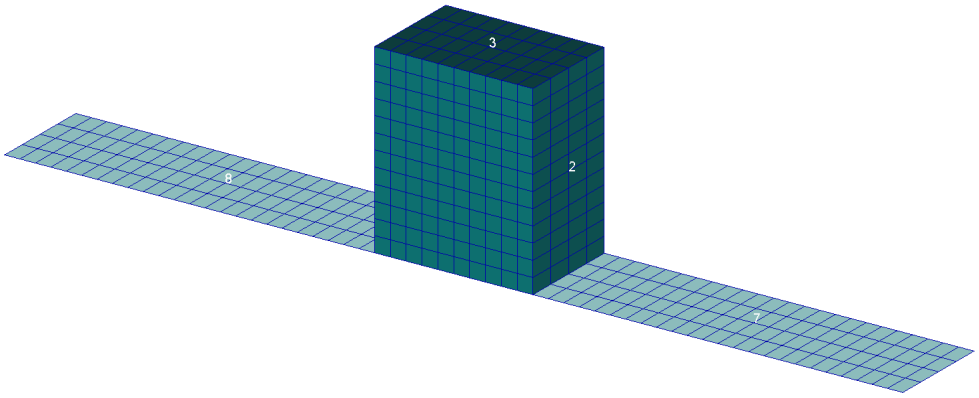

Figure 2.11: FEM model without hinge model

Property	**Value**
E	70 [GPa]
ν	0.33
G	210 [GPa]
ρ	$2.81e^{-3}$ $[kg/m^3]$

Table 2.3: Aluminium 7075 alloy mechanical properties

where E, ν, G, ρ are the Young's modulus, Poisson's ratio, Shear Strength and density, respectively.
Now, let introduce the proprieties of SAR's panels. Antennas are usually built using composite materials, allowing to reduce the total weight while guarantee enough stiffness still.
The ICEYE-X1 SAR panels have been modeled as a laminate with three layers, two aluminium external skin and a central honeycomb core made of NOMEX. The information about the laminate, the properties and the dimensions for the panels are as in [20, 21], because a similar spacecraft model has been here discussed.
It is important to underline that MSC Patran is an a-dimensional pre-processor, so when the length unit is fixed, others quantities must be consider in specific units. The geometrical dimensions of the model are considered in millimeter to better handle decimal values, so the E must be expressed in [MPa] and the density in $[ton/mm^3]$.
To quantify the impact of the flexible-rigid coupling effect, various configurations of the model just presented have been considered. The reason behind this choice is trying to establish a

Layer	**Properties**	**Thickness**
1. Aluminium skin	As seen in tab. 2.3	0.2 [mm]
2. Core	Nomex orthotropic: - E_{11}: 2.5 [GPa] - E_{12}: 1.3 [GPa] - ν_{11}: 0.2 - ν_{12}: 0.3 - G_{11}: 0.7 [GPa] - G_{12}: 0.6 [GPa] - ρ: $0.72e^{-3}$ $[kg/m^3]$	6 [mm]
3. Aluminium skin	As seen in tab. 2.3	0.2 [mm]

Table 2.4: SAR laminate composition

standard procedure separate from the geometry of the satellite. A parametric study of the length of the flexible panels have been conducted, moreover a scaled model of a factor γ = 1.5 has been analyzed. The different configurations considered are reported in tab. 2.5.

Variant	**Length of the panel**	**Total length of the SAR sensor**
Real model	1.4 [m]	3.4 [m]
Var. A	2.0 [m]	4.6 [m]
Var. B	2.5 [m]	5.6 [m]
Var. C	3.0 [m]	6.6 [m]

Table 2.5: Configurations of ICEYE-X1 satellite

Now that the base model is defined, it is possible to introduce the MPC links to simulate the hinges between the rigid hub and panels themselves. In MSC Patran reference frame the

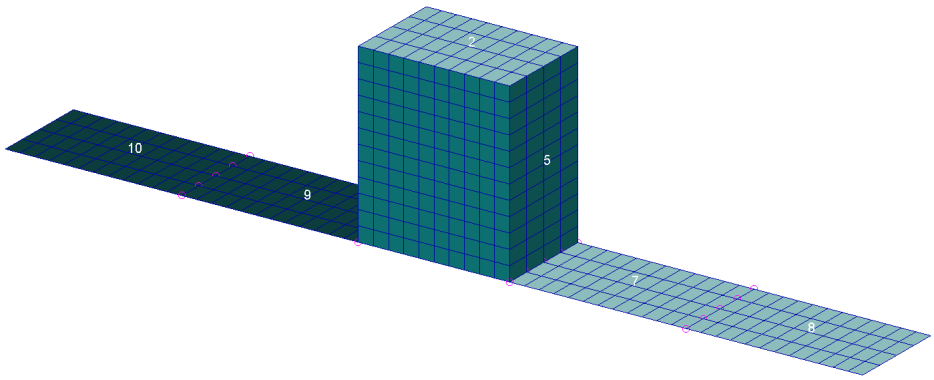

Figure 2.12: FEM Model with MPCs

rotation for the deployment sequence occurs around the z axis, so the DOF which must be not constraint is the one about this axis. In this primary design of the model, according to MSC Nastran user's guide [5], the RBAR element seems suitable for the goal. In fig. 2.13, the hinge connection occurs between nodes 2-3, which must be coincident. The independent

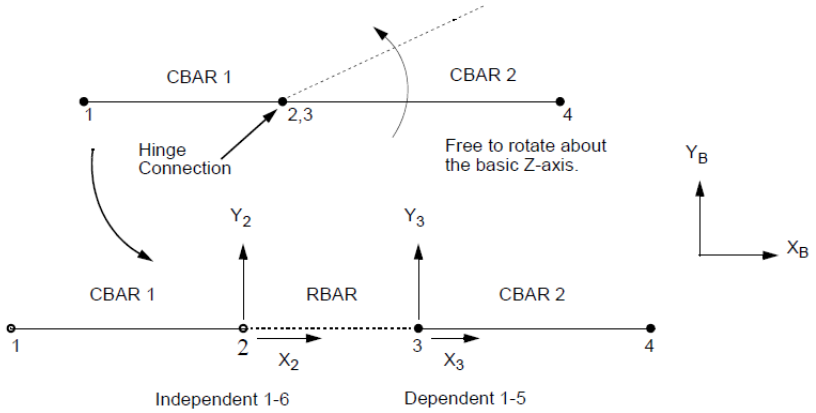

Figure 2.13: RBAR hinge model. [5]

node is the node 2, and all of its DOF (the three translation and the three rotations) are independent, while the node 3 has the five out of six DOF dependent from node 2, the only DOF left free is the rotation around the z axis. Although this situation is exactly the condition wanted to be modeled, various issues occur. Indeed, RBAR elements must be defined between CBAR elements, which are 1D element. Support 1D elements were considered at the beginning, however since each MPC have to be defined between every CBAR grid points, a 1D element should be defined for every mesh nodes considered, so this solution has been discarded.
The Explicit multi-point constraint type is chosen instead. This MPC allows to define an arbitrary number of independent and dependant nodes, and the relationships about DOFs are also user's choice. As in fig. 2.12, the hinge rotation axis in the model is the z axis, so in the definition of the explicit constraint, the independent nodes are constrained in each of them DOF, the dependant nodes have only the rotation about the selected axis left free instead, the first five DOFs depend on the displacement of independent nodes. A difference that can be noticed between the model in fig. 2.12 and fig. 2.11 is that the first one has four different panels to model the SAR array, while the second needs only two panels to properly model the antenna.

Analysis definition

Now that the structure model specification, the various configuration considered and the modeling of hinges connection by MPC elements have been presented, it is possible to proceed to the modal analysis needed. In MSC Nastran the modal analysis corresponds with the *SOL103*, the default settings for this solution regard the extraction method, the number of desired roots and the normalization method for eigenvectors, and are listed below:

- Extraction method: Lanczos
- Number or desired roots: 10
- Normalization method: Mass

The Lanczos method provides an efficient solutions for symmetric matrices and take advantage of the sparsity of the matrix, in fact when a matrix is large and sparse, Jacobi eigenvalue algorithm and other convergence-based iterative methods result computationally inefficient. A detailed view on the Lanczos algorithm is given in [22]. The number of desired roots stand for the number of eigenvalues that will be computed, since the models are free in space, the

number of rigid modes have to be taken into account, in particular for the model with MPC, where the presence of the hinge model adds degree of freedom. In addiction, to evaluate the differences between the order of truncation of δ matrix, for each configuration at least 5, 8 and 10 eigenvalues (excluding the rigid modes) have been considered. Finally, to avoid any singularity problem when the eigenvectors are considered in the orbital simulator, the normalization method selected is based on the maximum value. Finally, the updated analysis settings are as follow:

- Extraction method: Lanczos
- Number or desired roots for each configuration: 10, 15, 20
- Normalization method: Maximum

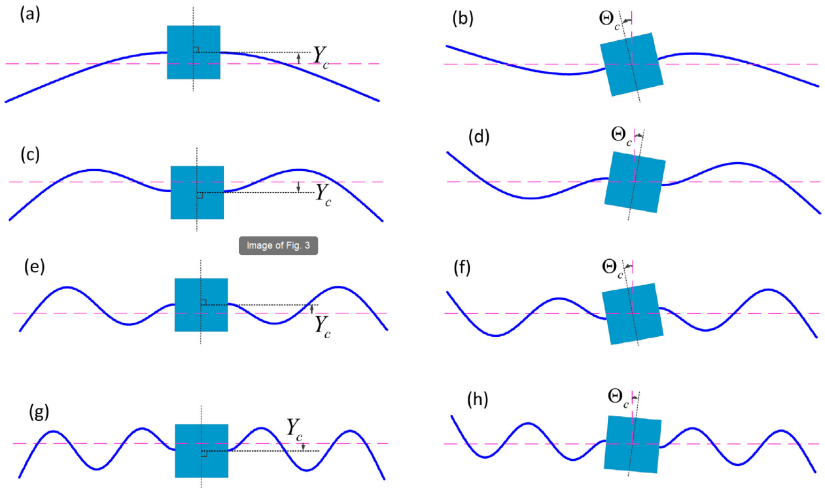

Figure 2.14: The first eight modes expected for the flexible spacecraft

The expected results are shown in fig. 2.14, while the actual results and the relative comments are reported in the first section of chapter 3.

2.4 Control laws

This section will present an overview of the general principles of a Guidance-Navigation-Control (GNC) system. Each aspect will be discussed in turn, with a particular focus on the control element. Subsequently, the control law selected in this thesis will be introduced, accompanied by an analysis of its distinctive features and the factors that led to its selection.

2.4.1 Guidance, Navigation, Control System

The Guidance, Navigation and Control System consists in the whole components used for position management and the components used by Attitude Determination and Control System (ADCS) [23]. Let introduce the three main parts of GNC:

- Guidance: consists of determining the desired position/orientation of the satellite, comparing them with the estimated actual values and then providing the reference for the controller to follow.

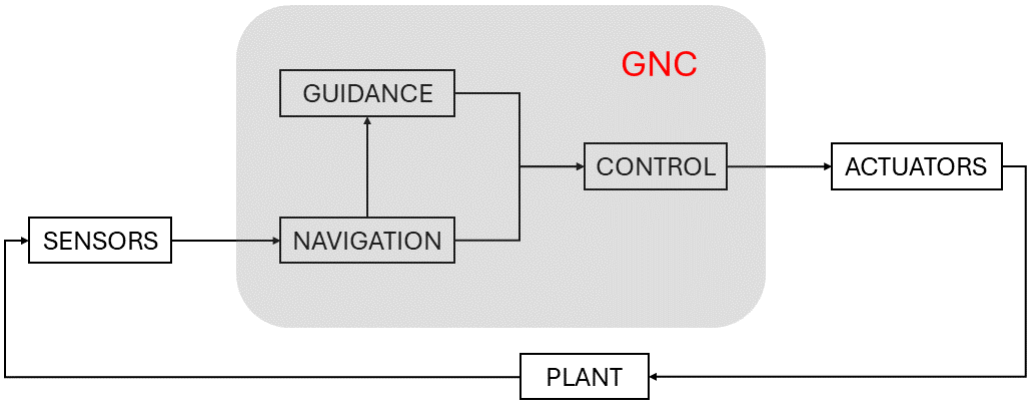

Figure 2.15: Guidance, Navigation and Control scheme

- Navigation: consists of evaluating the position/orientation of the satellite at a given time from the input of sensors, which can determinate the orientation of the satellite with respect to specific reference.
- Control: refers to the algorithms that calculate the necessary control forces and torques basing on the both the actual and desired position and orientation.

A complete scheme of a GNC system is reported in fig. 2.15. The ADCS system includes all the sensors for the navigation function, such star trackers, sun sensors, horizon sensors, and the actuators for providing the correction torques such reaction wheels, momentum wheels, thrusters. Finally, the plant includes the attitude dynamics and kinematics equations and the orbital perturbations. In real application, the actual orientation of the satellite is difficult to evaluate resulting in further complexity in ADCS modeling. For this reason the orientation of the satellite is considered totally known, which allows to omit the navigation function. Even with this strong hypothesis, the design of the ADCS results in an hard task due to non-linearity of the system, various uncertainties and a limited and fixed actuation power.
Control techniques are divided in two main category: the open-loop or feed-forward and the closed-loop or feedback approaches. The main and most relevant difference of these methods is the dependence of an input signal $u(t)$ from the output signal $y(t)$. In open-loop schemes, u(t) is not dependent from y(t), so they require a pre-determined pointing maneuver and are determined using optimal control techniques. They are sensitive to uncertainties and unexpected disturbances, furthermore, it is not possible to stabilize an unstable system. On the other hand, in closed-loop schemes, the signal u(t) takes into account the output signal, so they can handle parameters uncertainties and external disturbances, providing a more robust design method. In fig. 2.16 schemes of both open and closed control approaches are visualized, where $r(t)$ is a generic reference value and d stands for disturbances.

Quaternion feedback control

Satellites are often re-oriented by performing successive rotation around the control axis in order to achieve the desired orientation. However, this solution is not time nor fuel consumption optimal, although is very simple to be executed. The Quaternion feedback control provides a nearly-optimal orientation control, with a control law slightly more complex. Since quaternions

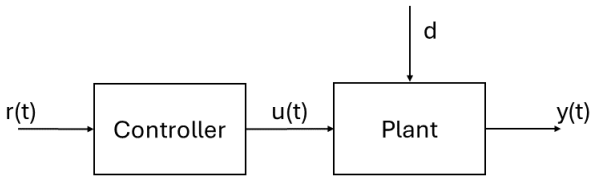

(a) Feed-forward control technique

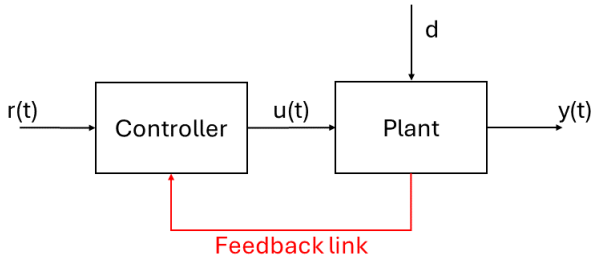

(b) Feedback control technique

Figure 2.16: Open and closed loop design

can be easily computed by modern ADCS, a closed-loop control is easily implemented onboard for autonomous maneuver.
The feedback control law employing the quaternion error q_e is:

$$\mathbf{T_c} = -K_p\mathbf{q_e} - K_d\omega_b \tag{2.47}$$

where $\mathbf{q_e} \in \mathcal{R}^3$ is the quaternion error vector defined in chapter 2, while K_p and K_d are gain matrices, tuned by trial-and-error method by the user. The control law in eq. (2.47) globally asymptotically stabilizes thee satellite into any arbitrary desired attitude for a wide choice of the gain matrices.
Let assume that $\mathbf{q_{des}} = [1, 0, 0, 0]^T$, in the hypothesis of fixed desired attitude. In this case, the inertial reference frame coincides with the desired attitude, so $\mathbf{q_e} = \mathbf{q_v}$, with $\mathbf{q_v}$ is the vectorial part of the true quaternion. In this case the control law become:

$$\mathbf{T_c} = -sign(q_{d_0})K_p\mathbf{q_v} - K_d\omega_b \tag{2.48}$$

where the sign function allow to consider both unit quaternions $\mathbf{q}_1 = [\pm 1, 0, 0, 0]^T$, while the scalar value of q_{d_0} express the magnitude of the rotation. Basing on the definition of the gain matrices, various QFC controllers can be defined, among these the simplest are:

- **Controller 1**
  - K_p=k$\mathbf{1}$
  - K_d=diag(d_1, d_2, d_3)
- **Controller 2**
  - K_p=$\dfrac{k}{q_{true_0}^3}\mathbf{1}$
  - K_d=diag(d_1, d_2, d_3)
- **Controller 3**
  - K_p=k·sign(q_{true_0})$\mathbf{1}$
  - K_d=diag(d_1, d_2, d_3)
- **Controller 4**
  - K_p=$[\alpha\mathbf{I} + \beta\mathbf{1}]^{-1}$
  - K_d=diag(d_1, d_2, d_3)

where k, d_i, α, β are positive scalar constants and $\mathbf{1}$, $\mathbf{I} \in \mathcal{R}^{3\times3}$ are the identity and inertia matrix, respectively. It can be noted that controller 1 is a particular case of controller 4 for $\alpha = 0$.
Before introducing how the tuning of gain matrices impacts the control action, some control entities of a second order system must be introduced.

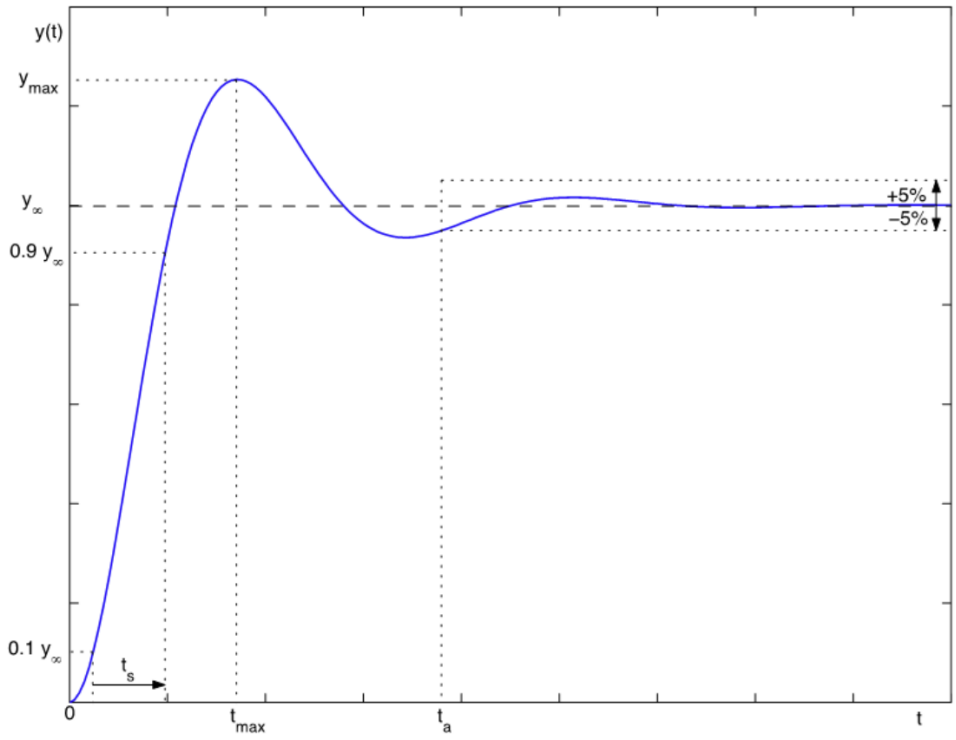

Figure 2.17: Time domain response [6]

where:

- y_∞ is the steady-state error, which correspond to the stationary value of the response
- t_s is the rise time from the 10% to the 90% of y_∞
- t_a is the settling time, and it considers a range of ±5% around the value of y_∞
- y_{max} is the peak value of the response
- $\hat{s} = \dfrac{y_{max} - y_\infty}{y_\infty}$ is the relative overshoot

Since there is not a fixed rule for tuning K_p and K_d, a general guide based on a large number of tests is reported in tab. 2.6. From this table it can be noted that an increasing of K_p matrix entries leads to decrement of the overall stability, while the increasing of the K_d coefficient gives an improvement of the stability of the system. The guidelines is not absolute and there is not certainty that by only increasing K_d values is possible to stabilize the system, it is a trade-off study problem that must be analyzed for the specific case study by trial-and-error method as said before, but the suggestions in tab. 2.6 are some of the best ways to start the tuning process.

The fundamental characteristics of QFC and its corresponding modelling schemes have now been introduced, thereby establishing a clear justification for the selection of this specific con-

	Rise time	Overshoot	Settling time	Steady-state error
Increasing K_p	decrease	increase	small increase	decrease
Increasing K_d	small decrease	decrease	decrease	minor change

Table 2.6: Tuning gain matrices guidelines

troller. The selection of Controller 4 for the orbit simulator employed in this work is particularly justified due to its optimal compatibility with the reaction wheels model, which represents a critical component of the system. This controller has been identified as the optimal choice among the alternatives considered, in terms of achieving the desired performance and stability. Furthermore, the selection of various system parameters, which are critical for the successful operation of the controller, was achieved through an iterative process of trial and error. This approach was necessary to fine-tune the parameters in a way that ensures a stable and reliable system under the operating conditions considered. The following section 3.1.2 will present these parameters in detail, along with their implications for system performance.

Chapter 3

Numerical simulations and results

This chapter presents the findings of the FEM analysis introduced in section 2.3.3 and the simulation presented in section 2.4 are finally shown. Initially, the orbital simulator realized in Simulink is presented, with its sub-systems and key parameters for the tunig process of controller. Then, the modal analysis results will be visualized and commented, with particular consideration given to the differences between the various configuration under consideration. Subsequently, the eigenvectors will be reported and the process for computing the coupling matrix δ will be introduced. Finally, the results of the ACS simulation will be presented.

3.1 Orbital simulator

This section presents the orbital simulator developed in Matlab/Simulink environment in each of its part, in order to understand how various sub-systems are linked together. All fixed input data are here presented and the final parameters adopted to have a stable system are listed. Furthermore, the reaction wheels model adopted is presented with also the simplification considered for the the orbital perturbations.

3.1.1 Reaction Wheels model

In Simulink, the reaction wheels can be modeled as a combination of a first order low pass filter and saturation. The filter is composed of a transfer function while the saturation establishes the maximum value of the actuation torque. ICEYE-X1 satellite is a three-axis stabilized spacecraft but no further information about reaction wheels configuration are reported so a pyramidal one is considered. A filter and saturation blocks are needed for each reaction wheel, in fig. 3.1 is possible to count four reaction wheels, with three wheels are the nominal operation wheels while the fourth is for redundancy, however it has to be considered in the simulator. For this reason a rotation matrix is needed to convert the control torque in four components and then back to three components.
The terms of low pass filter are the numerator and denominator coefficients. Denominators is composed of a term $(\tau_{RW} + 1)$, the value of τ_{RW} express the actuation torque defined in section 2.2. The saturation block limits the maximum torque that actuators should provide,

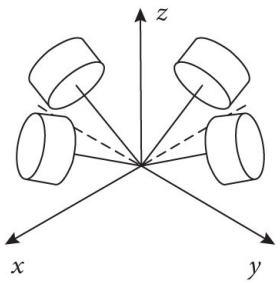

Figure 3.1: Reaction wheels pyramidal configuration

Reaction Wheels parameters	
τ_{RW}	5e-3 [Nm]
$U_{max_{RW}}$	0.01 [Nm]

Table 3.1: Reaction wheels parameter values

the parameter is $U_{max_{RW}}$ and the effective range is $[U_{max_{RW}}; -U_{max_{RW}}]$. The values has been determined after many trial-and-error iterations, the final ones are reported in table 3.1.

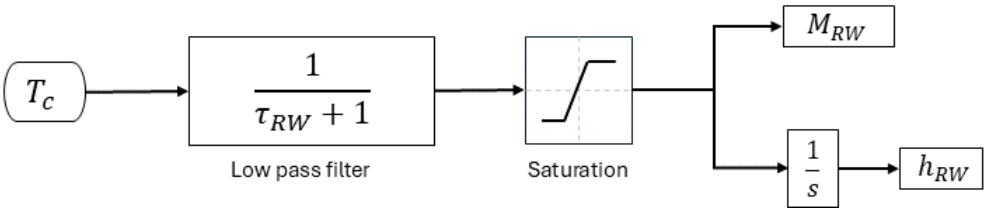

Figure 3.2: Reaction wheel model in Simulink

Finally, the RWs simulator receives the control output as input and giving the control torque M_{RW} as output.

3.1.2 QFC modeling

As introduced in sections above, the QFC controller evaluates the state error vector in terms of quaternions and angular rate to compute the control torque. It receives as inputs the quaternion vector and the angular velocity ω_b, and gives as output the correction torque needed. It's connected to the plant and to the reaction wheels block. The type 4 controller has been chosen and its parameters are reported in tab. 3.2, where d_1, d_2 and d_3 are the diagonal entries of the K_d gain matrix. In accordance with the prevailing literature, the values for α and β have been selected. The computation of K_p involves the inertia matrix, as defined in the previous chapter. Consequently, its entries change for every configuration under consideration. It was therefore considered unnecessary to report every K_p matrix, given that its variation is reflected in the final results of simulations.

QFC parameters	
α	0
β	30
d_1	0.9
d_2	0.9
d_3	0.9

Table 3.2: Quaternion feedback control parameter

3.1.3 Flexible dynamics torque modeling

In this thesis, the flexibility of the SAR panels is considered trough the equations introduced in subsec. 2.2.3. The flexible dynamics block in the simulator is composed of dynamics for each panels considered, so in the model with MPC constraint the block consider each of four panel individually, computing its participation factor and the summing all of them to determinate the global flexible momentum. In the model without MPC only two panels are considered instead, because the absence of connection allows to consider a unique panel as long as the two distinct panel. The input of this block is the angular acceleration vector $\dot{\omega}_b$.

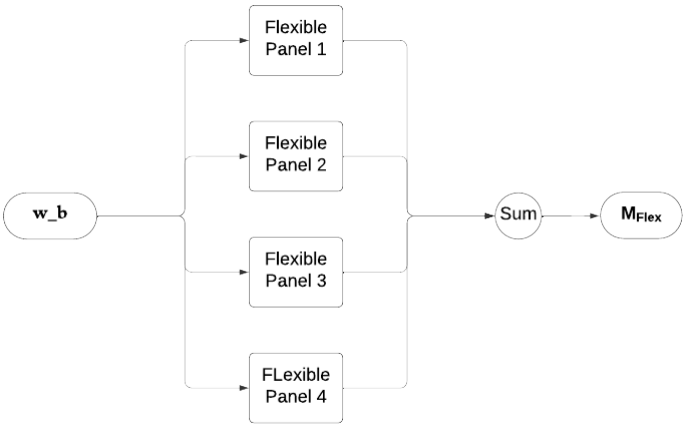

Figure 3.3: Example of the flexible dynamics block in Simulink

3.1.4 Orbital perturbations modeling

Orbital perturbations introduced in subsec. 2.2.4 applies torques on the system, so they have to be taken into account if a robust GNC system is desired. They have little effect on the system, but it must be consider in order to build a complete orbit simulator. The disturbance torques have been consider along the three axis of the spacecraft and have been modeled as harmonic function, considering the effects on each orbit period, exception for the solar radiation pressure. The parameters defined for each perturbation are reported in tables 3.3a to 3.3c [12].

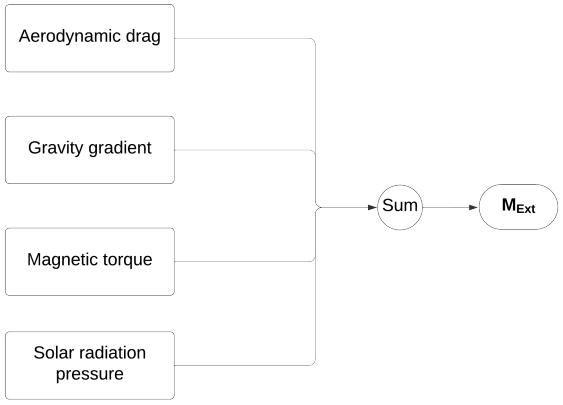

(a) Orbital disturbances sub-system

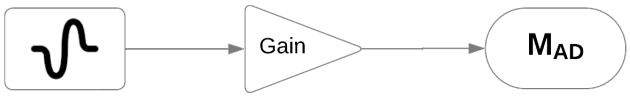

(b) Example of harmonic function for aerodynamic drag

Figure 3.4: Orbital perturbations model in Simulink

Sine wave specification	
Amplitude	1
Bias	1
Frequency	$\pi/200$
Phase	$3\pi/4$

(a) Aerodynamic drag

Sine wave specification	
Amplitude	1
Bias	1
Frequency	$\pi/300$
Phase	$\pi/2$

(b) Gravity Gradient

Sine wave specification	
Amplitude	1
Bias	1
Frequency	$\pi/150$
Phase	$\pi/4$

(c) Magnetic torque

Table 3.3: Orbital perturbations model parameters

3.2 FEM analysis results

This section presents the results of the finite element method (FEM) analysis in terms of modal modes, frequencies and eigenvector components. Subsequently, a further subsection introduces the computation of the coupling matrices and shows the results, which are later used in the orbital simulator.

3.2.1 Real model results

The first set of results are those of the first variant, as detailed in table 2.5, which has no MPC element and the actual dimension of ICEYE-X1 spacecraft. The results about the first ten modal shapes and the eigenvectors of the first three modal modes are shown in figs. 3.5 and 3.6, respectively. Additionally the natural frequencies used for the delta matrix are reported in

table 3.4. In the figs. 3.6a to 3.6c, the *ID POINTs* from 913 to 924 refer to centroid of sub-

λ		λ	
1	0.85874 [Hz]	6	5.69583 [Hz]
2	0.99482 [Hz]	7	14.85316 [Hz]
3	5.31319 [Hz]	8	14.87343 [Hz]
4	5.35647 [Hz]	9	17.63231 [Hz]
5	5.68142 [Hz]	10	17.63767 [Hz]

Table 3.4: Natural frequencies of first case study

panels of one antenna panel, while the ID POINTs from 925 to 936 refer to the other SAR panel, since in this variant the FEM model considers only two panels for the SAR array.

The results in fig. 3.5 are similar to the ones expected and shown in fig. 2.14, however while

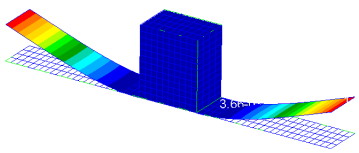

(a) Mode 1

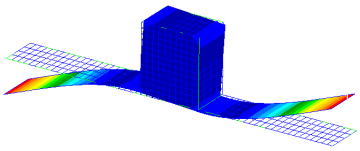

(b) Mode 2

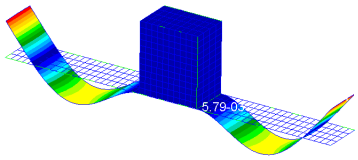

(c) Mode 3

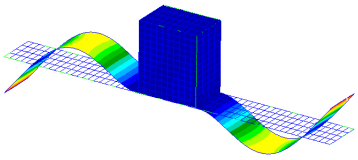

(d) Mode 4

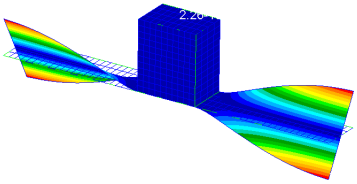

(e) Mode 5

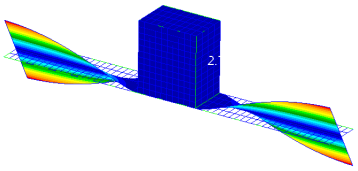

(f) Mode 6

in the latter only flexible modes are observed, the results of this case study show also torsional behaviour, specifically in mode 5, 6, 9 and 10. For this case only, a more comprehensive analysis was performed, specifically focusing on the extracted roots, i.e. eigenvalues, which are three, five and ten. This was done to evaluate the impact of considering a larger number of modes in the orbital simulator.

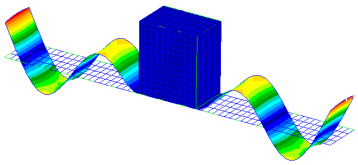

(g) Mode 7

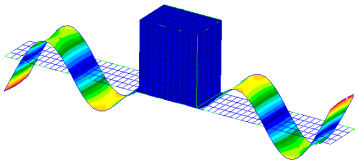

(h) Mode 8

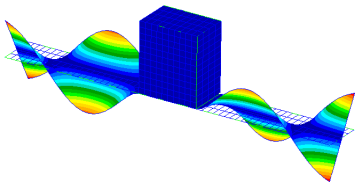

(i) Mode 9

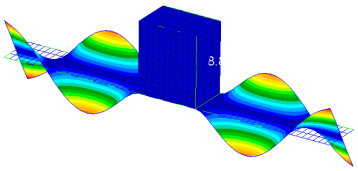

(j) Mode 10

Figure 3.5: First ten modal shapes of the first spacecraft variant

3.2.2 MPC model results

In the the model with MPC, only the first three modal modes are taken into account. Therefore, in the following a detailed comparison will be conducted between the models with and without MPC, with particular attention paid to the distinctions in their dynamic behaviour. The eigenvalues and corresponding eigenvectors have been computed and are presented in figs. 3.7 and 3.8, while the frequency for this case are provided in table 3.5.

The results reveal sharp differences between the two models, particularly with regard to both the modal frequencies and the corresponding modal shapes. Specifically, the frequencies in the MPC model are observed to be an order of magnitude higher compared to the model without MPC. Additionally, an significant distinction can be observed in the nature of the first non-rigid modes: in the MPC-based model, these modes show torsional behaviour, whereas in the model without MPC, they demonstrate flexible behaviour. This outcome is somewhat counter-intuitive, as the inclusion of additional degrees of freedom would typically be expected to reduce the global stiffness of the system. The increased stiffness observed in this case, however, can be attributed to the rigidity of the chosen MPC elements. It is important to note that the

λ	
1	5.29184 [Hz]
2	5.30608 [Hz]
3	11.0332 [Hz]

Table 3.5: Natural frequencies of MPC model

stiffness properties of the MPC elements in this model are not customisable by the user, which represents a limitation in the context of this study. As a result, the selected solution may not be the most suitable for accurately capturing the effects of hinges or flexible connections within the

EIGENVALUE = 2.911278E+01
CYCLES = 8.587405E-01 REAL EIGENVECTOR NO. 7

POINT ID.	TYPE	T1	T2	T3	R1	R2	R3
913	G	1.298017E-07	-4.117647E-03	1.187916E-08	-9.622864E-06	9.233436E-11	1.940478E-04
914	G	1.297063E-07	8.073454E-02	-3.055658E-10	-2.924998E-05	7.622752E-12	5.194118E-04
915	G	1.294643E-07	2.314817E-01	-8.859785E-11	-2.398108E-05	-4.945313E-13	7.577090E-04
916	G	1.294657E-07	4.274522E-01	-3.911009E-13	-1.494309E-05	-6.249429E-14	9.082199E-04
917	G	1.294673E-07	6.494205E-01	6.555691E-13	-7.304231E-06	-3.679882E-15	9.835193E-04
918	G	1.294673E-07	8.823225E-01	1.536515E-12	-2.993949E-06	-5.744284E-15	1.006559E-03
919	G	1.294661E-07	8.823225E-01	1.531576E-12	2.993949E-06	-6.774055E-15	1.006559E-03
920	G	1.294660E-07	6.494205E-01	-5.084354E-13	7.304231E-06	-8.838450E-15	9.835193E-04
921	G	1.294644E-07	4.274522E-01	-2.382688E-12	1.494309E-05	4.997595E-14	9.082199E-04
922	G	1.294631E-07	2.314817E-01	8.290309E-11	2.398108E-05	4.820129E-13	7.577090E-04
923	G	1.297050E-07	8.073454E-02	2.969502E-10	2.924998E-05	-7.635270E-12	5.194118E-04
924	G	1.298004E-07	-4.117647E-03	-1.189070E-08	9.622864E-06	-9.234688E-11	1.940478E-04
925	G	-1.297810E-07	-4.117647E-03	1.187395E-08	-9.622864E-06	-9.234687E-11	-1.940478E-04
926	G	-1.296856E-07	8.073454E-02	-3.137013E-10	-2.924998E-05	-7.635270E-12	-5.194118E-04
927	G	-1.294437E-07	2.314817E-01	-9.965401E-11	-2.398108E-05	4.820141E-13	-7.577090E-04
928	G	-1.294450E-07	4.274522E-01	-1.436794E-11	-1.494309E-05	4.997706E-14	-9.082199E-04
929	G	-1.294466E-07	6.494205E-01	-1.624198E-11	-7.304231E-06	-8.837493E-15	-9.835193E-04
930	G	-1.294467E-07	8.823225E-01	-1.828172E-11	-2.993949E-06	-6.773084E-15	-1.006559E-03
931	G	-1.294479E-07	8.823225E-01	-1.828668E-11	2.993949E-06	-5.743178E-15	-1.006559E-03
932	G	-1.294479E-07	6.494205E-01	-1.740595E-11	7.304231E-06	-3.678892E-15	-9.835193E-04
933	G	-1.294462E-07	4.274522E-01	-1.635954E-11	1.494309E-05	-6.249317E-14	-9.082199E-04
934	G	-1.294449E-07	2.314817E-01	7.184696E-11	2.398108E-05	-4.945301E-13	-7.577090E-04
935	G	-1.296868E-07	8.073454E-02	2.888147E-10	2.924998E-05	7.622754E-12	-5.194118E-04
936	G	-1.297823E-07	-4.117647E-03	-1.189591E-08	9.622864E-06	9.233435E-11	-1.940478E-04

(a) Eigenvector for λ_1

EIGENVALUE = 3.888694E+01
CYCLES = 9.924806E-01 REAL EIGENVECTOR NO. 8

POINT ID.	TYPE	T1	T2	T3	R1	R2	R3
913	G	-5.618884E-02	-5.488657E-02	7.434352E-09	-1.217235E-05	9.527703E-11	7.424112E-05
914	G	-5.618887E-02	1.210593E-02	-3.062166E-09	-3.707693E-05	4.042198E-12	4.835504E-04
915	G	-5.618888E-02	1.625587E-01	-2.159092E-09	-3.070415E-05	-3.116202E-12	7.876026E-04
916	G	-5.618890E-02	3.710732E-01	-1.472290E-09	-1.932654E-05	-2.646284E-12	9.821997E-04
917	G	-5.618891E-02	6.133798E-01	-8.670978E-10	-9.527761E-06	-2.594051E-12	1.080696E-03
918	G	-5.618891E-02	8.700459E-01	-2.633109E-10	-3.927899E-06	-2.529279E-12	1.111114E-03
919	G	-5.618891E-02	8.700459E-01	3.352976E-10	3.927899E-06	2.454164E-12	1.111114E-03
920	G	-5.618891E-02	6.133798E-01	9.215578E-10	9.527761E-06	2.518935E-12	1.080696E-03
921	G	-5.618890E-02	3.710732E-01	1.509223E-09	1.932654E-05	2.571166E-12	9.821997E-04
922	G	-5.618888E-02	1.625587E-01	2.178497E-09	3.070415E-05	3.041077E-12	7.876026E-04
923	G	-5.618887E-02	1.210593E-02	3.064040E-09	3.707693E-05	-4.117331E-12	4.835504E-04
924	G	-5.618884E-02	-5.488657E-02	-7.450010E-09	1.217235E-05	-9.535217E-11	7.424112E-05
925	G	-5.618884E-02	5.488657E-02	-7.481325E-09	1.217235E-05	9.527701E-11	7.424112E-05
926	G	-5.618887E-02	-1.210593E-02	3.015192E-09	3.707693E-05	4.042181E-12	4.835504E-04
927	G	-5.618888E-02	-1.625587E-01	2.112113E-09	3.070415E-05	-3.116227E-12	7.876026E-04
928	G	-5.618890E-02	-3.710732E-01	1.425304E-09	1.932654E-05	-2.646314E-12	9.821997E-04
929	G	-5.618891E-02	-6.133798E-01	8.201049E-10	9.527761E-06	-2.594082E-12	1.080696E-03
930	G	-5.618891E-02	-8.700459E-01	2.163105E-10	3.927899E-06	-2.529311E-12	1.111114E-03
931	G	-5.618891E-02	-8.700459E-01	-3.822981E-10	-3.927899E-06	2.454131E-12	1.111114E-03
932	G	-5.618891E-02	-6.133798E-01	-9.685506E-10	-9.527761E-06	2.518903E-12	1.080696E-03
933	G	-5.618890E-02	-3.710732E-01	-1.556208E-09	-1.932654E-05	2.571136E-12	9.821997E-04
934	G	-5.618888E-02	-1.625587E-01	-2.225476E-09	-3.070415E-05	3.041052E-12	7.876026E-04
935	G	-5.618887E-02	-1.210593E-02	-3.111014E-09	-3.707693E-05	-4.117351E-12	4.835504E-04
936	G	-5.618884E-02	5.488657E-02	7.403041E-09	-1.217235E-05	-9.535217E-11	7.424112E-05

(b) Eigenvector for λ_2

EIGENVALUE = 1.114475E+03
CYCLES = 5.313189E+00 REAL EIGENVECTOR NO. 9

POINT ID.	TYPE	T1	T2	T3	R1	R2	R3
913	G	-9.105757E-07	-5.721793E-02	-9.695068E-08	-3.354200E-06	-3.752956E-10	-1.020543E-03
914	G	-9.186092E-07	-4.027434E-01	-9.714971E-10	-4.584191E-05	-7.279649E-11	-1.627096E-03
915	G	-9.168283E-07	-6.873595E-01	6.528869E-10	-1.596468E-04	1.455538E-12	-5.968176E-04
916	G	-9.167846E-07	-6.194225E-01	1.345955E-11	-1.918235E-04	4.982639E-13	1.218147E-03
917	G	-9.168003E-07	-1.414292E-01	-4.522083E-12	-1.378657E-04	-4.868637E-15	2.758848E-03
918	G	-9.168030E-07	5.957530E-01	-2.599632E-13	-7.005385E-05	-5.055536E-15	3.406245E-03
919	G	-9.168029E-07	5.957530E-01	3.324271E-13	7.005385E-05	5.334798E-15	3.406245E-03
920	G	-9.168003E-07	-1.414292E-01	4.659695E-12	1.378657E-04	5.147857E-15	2.758848E-03
921	G	-9.167846E-07	-6.194225E-01	-1.325678E-11	1.918235E-04	-4.979846E-13	1.218147E-03
922	G	-9.168283E-07	-6.873595E-01	-6.526189E-10	1.596468E-04	-1.455259E-12	-5.968176E-04
923	G	-9.186092E-07	-4.027434E-01	9.718301E-10	4.584191E-05	7.279677E-11	-1.627096E-03
924	G	-9.105757E-07	-5.721793E-02	9.695108E-08	3.354200E-06	3.752959E-10	-1.020543E-03
925	G	9.105628E-07	-5.721793E-02	-9.695057E-08	-3.354200E-06	3.752959E-10	1.020543E-03
926	G	9.185962E-07	-4.027434E-01	-9.713253E-10	-4.584191E-05	7.279677E-11	1.627096E-03
927	G	9.168153E-07	-6.873595E-01	6.531213E-10	-1.596468E-04	-1.455269E-12	5.968176E-04
928	G	9.167717E-07	-6.194225E-01	1.375669E-11	-1.918235E-04	-4.979947E-13	-1.218147E-03
929	G	9.167873E-07	-1.414292E-01	-4.162124E-12	-1.378657E-04	5.137791E-15	-2.758848E-03
930	G	9.167900E-07	5.957530E-01	1.628013E-13	-7.005385E-05	5.324737E-15	-3.406245E-03
931	G	9.167900E-07	5.957530E-01	7.551834E-13	7.005385E-05	-5.065538E-15	-3.406245E-03
932	G	9.167874E-07	-1.414292E-01	5.019645E-12	1.378657E-04	-4.878693E-15	-2.758848E-03
933	G	9.167717E-07	-6.194225E-01	-1.295965E-11	1.918235E-04	4.982538E-13	-1.218147E-03
934	G	9.168154E-07	-6.873595E-01	-6.523847E-10	1.596468E-04	1.455528E-12	5.968176E-04
935	G	9.185963E-07	-4.027434E-01	9.720015E-10	4.584191E-05	-7.279651E-11	1.627096E-03
936	G	9.105628E-07	-5.721793E-02	9.695119E-08	3.354200E-06	-3.752956E-10	1.020543E-03

(c) Eigenvector for λ_3

Figure 3.6: First three eigenvectors for first case study

system. Nevertheless, the separation of degrees of freedom (DOFs) around the z-axis, enabled by the MPC formulation, offers the advantage by allowing the structural panels to behave as independent entities. This decoupling of the panels aligns with one of the primary objectives of this thesis, which aimed to model the panels independently while accounting for their dynamic interactions.

Given the specific goals of this work, particularly the need to achieve independent panel behavior, the MPC-based approach has been retained despite its limitations. Although the rigid nature of the MPC elements might not fully capture the flexibility introduced by hinges, the overall framework provides a sufficient representation of the system's dynamics for the purposes of this investigation.

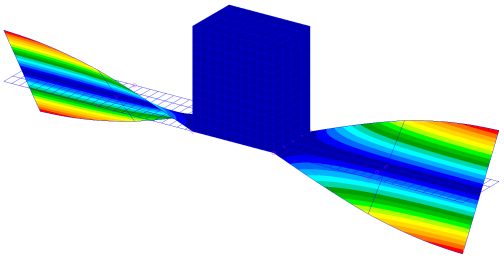

(a) Mode 1

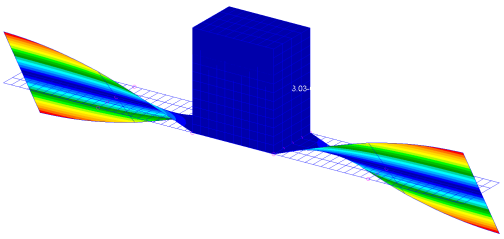

(b) Mode 2

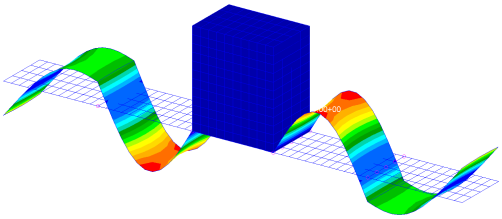

(c) Mode 3

Figure 3.7: MPC model modal shapes

3.2.3 Results of variant A, B and C

The results of the remaining analysed variants are here presented. In order to estimate the effect of larger flexible panels in rigid-flexible coupling, the panels of the three variants are progressively longer, while the rigid hub remains unchanged. All of these configurations consider the model without MPCs, and the specifications of each variant are reported in table 2.5. Moreover, the results of an additional variant that implements a scale factor for the entire structure are also introduced here.
For each of these case studies, only the first three modal modes are considered. As the modal shapes are comparable to those of the initial configuration, only the natural frequencies and eigenvectors will be reported, as they are directly utilised for the orbital simulator, in table 3.6 and in figs. 3.9 to 3.11, respectively.

λ	
1	0.42231 [Hz]
2	0.57004 [Hz]
3	2.60653 [Hz]

(a) Variant A

λ	
1	0.27070 [Hz]
2	0.42142 [Hz]
3	1.66691 [Hz]

(b) Variant B

λ	
1	0.18842 [Hz]
2	0.33677 [Hz]
3	1.15734 [Hz]

(c) Variant C

Table 3.6: Natural frequencies of variant configurations

Scaled model

As introduced in section 2.3.3, an additional variant is studied. This one differs from the others since it applies a scale factor γ = 1.5 across the whole structure rather than only to flexible panels. This decision is driven by the objective of evaluating the implications of using flexible appendages in smaller satellite classes.
To quantify the effect of the scale factor on the dimensions of the model, the corresponding values are presented in the following table.

Scale factor γ = 1.5	
Height	46.67 [cm]
Length	40.00 [cm]
Depth	26.67 [cm]
Panels' length	46.67 [cm]
Total mass	56.67 [kg]

Table 3.7: Dimensions of the scaled model

The modal shapes are again equivalent to those of the original model, so only the first natural frequencies and corresponding eigenvectors are reported.

λ	
1	1.94289 [Hz]
2	2.26938 [Hz]
3	11.9989 [Hz]

Table 3.8: Natural frequencies of scaled model

3.2.4 Coupling matrix determination

In order to compute the requisite δ matrices, a Matlab script has been developed. Given the necessity to consider a variety of configurations, it is essential that the code be as generic as possible. This approach allows the matrix for each case to be obtained with minimal modification of the data inputs.
This approach involves consolidating the entire process into a single script designed to handle multiple case studies, with each case study represented by its own section. In each section, only two key parameters - the length of the antenna panel and the mesh size - are modified

to reflect the specific configuration of the spacecraft variant being analysed. Once these two parameters have been updated, the script is able to automatically calculate the main characteristics of the system, such as the mass of the panel, moments of inertia and other essential physical characteristics. However, the only exception to this approach is the stiffness matrix K, which requires manual input for each variant of the spacecraft. The stiffness matrix must be provided for each individual configuration because, together with the damping matrix D, it reflects the mechanical properties and structural behaviour of the spacecraft in each case, and both matrices are essential for the calculation of the δ matrix. Furthermore, the rotational transformations necessary to align the sub-panels' local frames with the spacecraft's body frame remain consistent across all configurations, as the reference frame used in Patran remains unaltered. In order to facilitate the implementation of these transformations, a custom MATLAB function has been written. The function is responsible for calculating the rotation matrix, represented by $L = R_z \times R_y \times R_x$. Moreover, another MATLAB function is utilised to derive the skew-symmetric matrix from a given 3x1 vector. By automating these processes with dedicated functions, the code becomes more modular, reducing redundancy and improving readability, while ensuring that the transformations and matrix manipulations are consistent and accurate across all configurations.
The final matrices are now ready for reporting. The matrices for all the variants without MPC elements are presented first, followed by the matrices for the model with MPC.

Delta matrices for the first case study (first three modes)

$$\delta_1 = \begin{bmatrix} 0.00 & 0.00 & -0.3568 \\ 0.00 & 0.00 & -0.2488 \\ 0.00 & 0.00 & 0.2066 \end{bmatrix} \quad \delta_2 = \begin{bmatrix} 0.00 & 0.00 & 0.3568 \\ 0.00 & 0.00 & -0.2488 \\ 0.00 & 0.00 & -0.2066 \end{bmatrix}$$

Delta matrices for the first case study (first five modes)

$$\delta_1 = \begin{bmatrix} 0.00 & 0.00 & -0.3568 \\ 0.00 & 0.00 & -0.2488 \\ 0.00 & 0.00 & 0.2066 \\ 0.00 & 0.00 & 0.1873 \\ 0.00 & 0.00 & 0.00 \end{bmatrix} \quad \delta_2 = \begin{bmatrix} 0.00 & 0.00 & 0.3568 \\ 0.00 & 0.00 & -0.2488 \\ 0.00 & 0.00 & -0.2066 \\ 0.00 & 0.00 & 0.1873 \\ 0.00 & 0.00 & 0.00 \end{bmatrix}$$

Delta matrices for the first case study (first ten modes)

$$\delta_1 = \begin{bmatrix} 0.00 & 0.00 & -0.3568 \\ 0.00 & 0.00 & -0.2488 \\ 0.00 & 0.00 & 0.2066 \\ 0.00 & 0.00 & 0.1873 \\ 0.00 & 0.00 & 0.00 \\ -0.0072 & -0.0062 & 0.00 \\ 0.00 & 0.00 & -0.1115 \\ 0.00 & 0.00 & -0.1031 \\ 0.00 & 0.00 & -0.00 \\ 0.0024 & 0.0020 & 0.00 \end{bmatrix} \quad \delta_2 = \begin{bmatrix} 0.00 & 0.00 & 0.3568 \\ 0.00 & 0.00 & -0.2488 \\ 0.00 & 0.00 & -0.2066 \\ 0.00 & 0.00 & 0.1873 \\ 0.00 & 0.00 & 0.00 \\ -0.0072 & 0.0062 & 0.00 \\ 0.00 & 0.00 & 0.1115 \\ 0.00 & 0.00 & -0.1031 \\ 0.00 & 0.00 & -0.00 \\ 0.0024 & -0.0020 & 0.00 \end{bmatrix}$$

Delta matrices for the variant A

$$\delta_1 = \begin{bmatrix} 0.00 & 0.00 & 0.5038 \\ 0.00 & 0.00 & 0.2169 \\ 0.00 & 0.00 & -0.2956 \end{bmatrix} \quad \delta_2 = \begin{bmatrix} 0.00 & 0.00 & -0.5038 \\ 0.00 & 0.00 & 0.2169 \\ 0.00 & 0.00 & 0.2956 \end{bmatrix}$$

Delta matrices for the variant B

$$\delta_1 = \begin{bmatrix} 0.00 & 0.00 & -0.6244 \\ 0.00 & 0.00 & -0.1154 \\ 0.00 & 0.00 & 0.3690 \end{bmatrix} \quad \delta_2 = \begin{bmatrix} 0.00 & 0.00 & 0.6244 \\ 0.00 & 0.00 & -0.1154 \\ 0.00 & 0.00 & -0.3690 \end{bmatrix}$$

Delta matrices for the variant C

$$\delta_1 = \begin{bmatrix} 0.00 & 0.00 & -0.7429 \\ 0.00 & 0.00 & 0.0393 \\ 0.00 & 0.00 & 0.4415 \end{bmatrix} \quad \delta_2 = \begin{bmatrix} 0.00 & 0.00 & 0.7429 \\ 0.00 & 0.00 & 0.0393 \\ 0.00 & 0.00 & -0.4415 \end{bmatrix}$$

Delta matrices for the scaled model

$$\delta_1 = \begin{bmatrix} 0.00 & 0.00 & -0.1051 \\ 0.00 & 0.00 & -0.0706 \\ 0.00 & 0.00 & 0.0610 \end{bmatrix} \quad \delta_2 = \begin{bmatrix} 0.00 & 0.00 & 0.1051 \\ 0.00 & 0.00 & -0.0706 \\ 0.00 & 0.00 & -0.0610 \end{bmatrix}$$

Delta matrices for the MPC model

$$\delta_1 = \begin{bmatrix} 0.00 & 0.00 & 0.00 \\ -0.0039 & -0.0033 & 0.00 \\ 0.00 & 0.00 & -0.2470 \end{bmatrix} \quad \delta_2 = \begin{bmatrix} 0.00 & 0.00 & 0.00 \\ -0.0039 & -0.0111 & 0.00 \\ 0.00 & 0.00 & 0.3487 \end{bmatrix}$$

$$\delta_3 = \begin{bmatrix} 0.00 & 0.00 & 0.00 \\ -0.0039 & 0.0033 & 0.00 \\ 0.00 & 0.00 & -0.2470 \end{bmatrix} \quad \delta_4 = \begin{bmatrix} 0.00 & 0.00 & 0.00 \\ -0.0039 & 0.0111 & 0.00 \\ 0.00 & 0.00 & 0.3487 \end{bmatrix}$$

3.3 Simulation results

This section will present and analyse the results obtained from the orbital simulator presented in section 3.1 for an inertial pointing manoeuvrer. The results include comprehensive diagrams and figures that illustrate the main entities, such as the actuation torque required for successful manoeuvring and the corresponding time needed to achieve a stable orbital condition or the perturbation given by the flexible panels. The analysis will encompass the dynamics of the spacecraft during its transition to stability, with particular attention paid to key factors such as torque magnitudes, the timing of manoeuvres, and any perturbations encountered throughout the process. In the following series of results, the selected integrator is ode4 with a fixed step size of 0.01 seconds. The simulation time was set according to the time required to reach a stable condition.

As was done in the previous section, the present section will be divided into sub-sections, thus facilitating a more accurate visualisation of the results obtained in each case study. Firstly, the model representing the actual dimensions of the ICEYE spacecraft is presented. Subsequently, for a more comprehensive and rapid comparison, the model with multi-point constraint is reported to determine the effect of the hinge model on the control strategy. Finally, the results of the other case study will be displayed.

3.3.1 Real model simulation results

In order to evaluate how the modal base is a function of the number of normal modes considered, a series of simulations was conducted using three distinct modal configurations: three modes, five modes, and ten modes. The primary focus of this analysis is to understand how the number of modes influences key system parameters. In particular, the main outcomes relate to the angular velocities of the system, the perturbation momentum generated by the flexible appendages, and the control torque required to achieve and maintain the desired orientation. By comparing these results across the different modal sets, the aim is to identify how increasing the number of normal modes impacts the overall system dynamics, basing on the participation factor of higher order modes, including the control effort needed for stabilization and maneuvering. This analysis provides insights into the trade-offs between computational complexity and performance in systems with flexible components.

As illustrated in fig. 3.13, the main disturbance of angular velocities is observed along the z-axis, due to the flexible behaviour exhibited by the first three modal modes, highlighted by the flexible torque acting only around z-axis showed in fig. 3.14. This results in the occurrence of vibration phenomena throughout the duration of the simulation. It is evident that the residual error remains uncorrected, as it is of an equivalent order of magnitude to the control action. In fig. 3.16 the evolution of quaternions is shown, demonstrating the successful achievement of the desired orientation. Finally, the torque given by reaction wheels are reported in fig. 3.15. Once again, it possible to notice that the main action is performed by the wheel aligned with z-axis.

Now the other sets of results for five and ten modes will be reported in figs. 3.18 to 3.22 and figs. 3.23 to 3.27, respectively.

These results indicate that only the most energetic modes, specifically the first five or so modes, have a significant impact on control effort. This suggests that beyond these dominant modes, the influence on control effort becomes negligible, meaning that focusing on them is sufficient to achieve effective control. The less energetic modes contribute very little, if anything, to the overall control dynamics, allowing a more efficient and targeted approach to the design of control strategies.

3.3.2 MPC model simulation results

For MPC model, the simulation results are shown in figs. 3.28 to 3.32. As demonstrated in fig. 3.28, the stability of quaternions is achieved. This confirms the functionality of the orbital simulator. The trends for angular velocities are similar to those observed in the absence of MPC, exhibiting a persistent error in the component oriented along the z-axis. The initial three modes of the MPC case study, as seen in fig. 3.7 , include the first two modes with torsional behaviour, resulting in the perturbation momentum acting on all three axes, as illustrated in fig. 3.30. This contrasts with the observations made in the case study without MPCs and only three modes considered. Finally, in fig. 3.32 the modal coordinates of each SAR panels are shown.

The effect of hinge model based on MPCs can be immediately noted in a more stable evolution for angular velocities and control torques, but mostly in the perturbation momentum by the flexible panels, as show in fig. 3.30. This figure shows an effect around the x and y axes due to the torsional behaviour of the first two modal modes. Unlike the case without the MPC elements, where the flexible perturbation momentum is zero throughout the simulation, in this case it is present, although with a magnitude of 10^{-7}. Further evidence of the effect of the MPCs can be seen in the modal coordinates, which show a symmetrical evolution for the couples of panels 1-3 and 2-4. In this case, the evolution around the x-axis is zero, because the panel oscillation occurs around the hinge axis, with no perturbation along this axis.

3.3.3 Simulation results of other variants

In conclusion, the simulation results for the remaining variants of the model without MPC elements are presented. As previously, the results include the evolution of quaternions and angular velocities, the magnitude of external and flexible perturbation momentum, and the modal coordinates for flexible appendages. It should be noted that the specifications of these variants are reported in table 2.5. The main difference between variants A, B and C and the base model is the total length of SAR panels. In contrast, for the scaled model, the scale factor is applied to the entire structure.
The results for variants A, B and C are firstly presented in figs. 3.33 to 3.37, figs. 3.38 to 3.42 and figs. 3.43 to 3.47, respectively. Then, the results for scaled model are in figs. 3.48 to 3.52.

Despite the progressive increase in panel length, which results in an overall increase in the system's total mass, as evidenced by the observed decline in frequencies in table 3.6, in accordance with the eq. (2.40), the evolution observed in the various results remain consistent across all variants under consideration and with the actual model. However, it must be noted

that the oscillation on angular rates, as shown in fig. 3.44b, while the perturbation momentum by the flexible appendages around the z-axis showed an increase in oscillation. This is easily explained by the increasing size of the panels, which logically increases the amount of disturbance generated.

EIGENVALUE = 1.105538E+03
CYCLES = 5.291844E+00 REAL EIGENVECTOR NO. 11

POINT ID.	TYPE	T1	T2	T3	R1	R2	R3
917	G	1.652423E-06	6.458447E-02	6.607048E-06	6.449440E-04	-1.653202E-08	5.467789E-04
918	G	1.655782E-06	1.893113E-01	1.047210E-05	1.890069E-03	-1.655944E-08	5.106075E-04
919	G	1.656551E-06	3.023343E-01	1.433722E-05	3.017353E-03	-1.656711E-08	4.524377E-04
920	G	-1.656551E-06	-3.023343E-01	1.433722E-05	3.017353E-03	-1.656711E-08	-4.524377E-04
921	G	-1.655782E-06	-1.893113E-01	1.047210E-05	1.890069E-03	-1.655944E-08	-5.106075E-04
922	G	-1.652422E-06	-6.458447E-02	6.607048E-06	6.449440E-04	-1.653202E-08	-5.467789E-04
923	G	1.657022E-06	3.935621E-01	1.820366E-05	3.928125E-03	-1.657147E-08	3.207049E-04
924	G	1.657254E-06	4.569150E-01	2.207074E-05	4.561724E-03	-1.657336E-08	2.114849E-04
925	G	1.657332E-06	4.920330E-01	2.593798E-05	4.910787E-03	-1.657362E-08	9.313924E-05
926	G	-1.657331E-06	-4.920330E-01	2.593798E-05	4.910787E-03	-1.657362E-08	-9.313924E-05
927	G	-1.657254E-06	-4.569150E-01	2.207074E-05	4.561724E-03	-1.657336E-08	-2.114849E-04
928	G	-1.657021E-06	-3.935621E-01	1.820366E-05	3.928125E-03	-1.657147E-08	-3.207049E-04
929	G	1.652422E-06	-6.458463E-02	-6.606993E-06	-6.449457E-04	-1.653202E-08	5.467789E-04
930	G	1.655782E-06	-1.893113E-01	-1.047204E-05	-1.890069E-03	-1.655944E-08	5.106075E-04
931	G	1.656551E-06	-3.023342E-01	-1.433715E-05	-3.017351E-03	-1.656711E-08	4.524377E-04
932	G	-1.656551E-06	3.023342E-01	-1.433715E-05	-3.017351E-03	-1.656711E-08	-4.524377E-04
933	G	-1.655782E-06	1.893113E-01	-1.047204E-05	-1.890069E-03	-1.655944E-08	-5.106075E-04
934	G	-1.652422E-06	6.458463E-02	-6.606993E-06	-6.449457E-04	-1.653202E-08	-5.467789E-04
935	G	1.657022E-06	-3.935631E-01	-1.820365E-05	-3.928135E-03	-1.657147E-08	3.207040E-04
936	G	1.657254E-06	-4.569150E-01	-2.207068E-05	-4.561724E-03	-1.657336E-08	2.114849E-04
937	G	1.657332E-06	-4.920327E-01	-2.593787E-05	-4.910784E-03	-1.657362E-08	9.314029E-05
938	G	-1.657331E-06	4.920327E-01	-2.593787E-05	-4.910784E-03	-1.657362E-08	-9.314029E-05
939	G	-1.657254E-06	4.569150E-01	-2.207068E-05	-4.561724E-03	-1.657336E-08	-2.114849E-04
940	G	-1.657021E-06	3.935631E-01	-1.820365E-05	-3.928135E-03	-1.657147E-08	-3.207040E-04

(a) Eigenvector for λ_1

EIGENVALUE = 1.111495E+03
CYCLES = 5.306081E+00 REAL EIGENVECTOR NO. 12

POINT ID.	TYPE	T1	T2	T3	R1	R2	R3
917	G	-3.476653E-07	-6.268924E-02	-7.051263E-03	-6.260017E-04	4.366855E-09	-5.485512E-04
918	G	-7.219486E-07	-1.878620E-01	-7.052838E-03	-1.875581E-03	7.913412E-09	-5.126093E-04
919	G	-9.609588E-07	-3.013599E-01	-7.055057E-03	-3.007595E-03	1.014947E-08	-4.544500E-04
920	G	9.609587E-07	3.013599E-01	-7.055057E-03	-3.007595E-03	1.014947E-08	4.544500E-04
921	G	7.219484E-07	1.878620E-01	-7.052838E-03	-1.875581E-03	7.913412E-09	5.126093E-04
922	G	3.476651E-07	6.268924E-02	-7.051263E-03	-6.260017E-04	4.366855E-09	5.485512E-04
923	G	-1.097841E-06	-3.930159E-01	-7.057651E-03	-3.922635E-03	1.136411E-08	-3.222984E-04
924	G	-1.161762E-06	-4.566892E-01	-7.060415E-03	-4.559431E-03	1.184909E-08	-2.125763E-04
925	G	-1.181717E-06	-4.919907E-01	-7.063213E-03	-4.910315E-03	1.189696E-08	-9.363223E-05
926	G	1.181717E-06	4.919907E-01	-7.063213E-03	-4.910315E-03	1.189696E-08	9.363223E-05
927	G	1.161762E-06	4.566892E-01	-7.060415E-03	-4.559431E-03	1.184909E-08	2.125763E-04
928	G	1.097841E-06	3.930159E-01	-7.057651E-03	-3.922635E-03	1.136411E-08	3.222984E-04
929	G	3.476719E-07	-6.268941E-02	-7.051263E-03	-6.260034E-04	-4.366919E-09	5.485512E-04
930	G	7.219546E-07	-1.878620E-01	-7.052838E-03	-1.875581E-03	-7.913474E-09	5.126093E-04
931	G	9.609646E-07	-3.013598E-01	-7.055057E-03	-3.007594E-03	-1.014953E-08	4.544500E-04
932	G	-9.609648E-07	3.013598E-01	-7.055057E-03	-3.007594E-03	-1.014953E-08	-4.544500E-04
933	G	-7.219548E-07	1.878620E-01	-7.052838E-03	-1.875581E-03	-7.913474E-09	-5.126093E-04
934	G	-3.476721E-07	6.268941E-02	-7.051263E-03	-6.260034E-04	-4.366919E-09	-5.485512E-04
935	G	1.097848E-06	-3.930169E-01	-7.057651E-03	-3.922645E-03	-1.136418E-08	3.222975E-04
936	G	1.161768E-06	-4.566892E-01	-7.060415E-03	-4.559431E-03	-1.184915E-08	2.125764E-04
937	G	1.181723E-06	-4.919904E-01	-7.063213E-03	-4.910312E-03	-1.189702E-08	9.363329E-05
938	G	-1.181723E-06	4.919904E-01	-7.063213E-03	-4.910312E-03	-1.189702E-08	-9.363329E-05
939	G	-1.161768E-06	4.566892E-01	-7.060415E-03	-4.559431E-03	-1.184915E-08	-2.125764E-04
940	G	-1.097848E-06	3.930169E-01	-7.057651E-03	-3.922645E-03	-1.136418E-08	-3.222975E-04

(b) Eigenvector for λ_2

EIGENVALUE = 4.805726E+03
CYCLES = 1.103315E+01 REAL EIGENVECTOR NO. 13

POINT ID.	TYPE	T1	T2	T3	R1	R2	R3
917	G	-5.328627E-03	5.060279E-01	6.728854E-08	2.356044E-04	1.289715E-09	3.883697E-03
918	G	-5.328920E-03	9.183390E-01	-3.999744E-08	4.682986E-04	1.531124E-11	-7.926010E-04
919	G	-5.329140E-03	1.641114E-01	-2.528391E-08	2.649312E-04	-3.849208E-11	-5.150195E-03
920	G	-5.329140E-03	1.641114E-01	2.528835E-08	-2.649312E-04	3.848831E-11	-5.150195E-03
921	G	-5.328920E-03	9.183390E-01	4.000099E-08	-4.682986E-04	-1.531500E-11	-7.926010E-04
922	G	-5.328627E-03	5.060279E-01	-6.728586E-08	-2.356044E-04	-1.289719E-09	3.883697E-03
923	G	-5.329303E-03	-5.560927E-01	-1.744259E-08	-7.058153E-05	-3.039196E-11	-3.301196E-04
924	G	-5.329412E-03	-3.810824E-01	-1.048046E-08	-1.945006E-04	-2.994988E-11	1.933819E-03
925	G	-5.329466E-03	2.780360E-01	-3.505025E-09	-1.379347E-04	-2.921009E-11	3.418979E-03
926	G	-5.329466E-03	2.780360E-01	3.512106E-09	1.379347E-04	2.920631E-11	3.418979E-03
927	G	-5.329412E-03	-3.810824E-01	1.048666E-08	1.945006E-04	2.994610E-11	1.933819E-03
928	G	-5.329303E-03	-5.560927E-01	1.744791E-08	7.058153E-05	3.038818E-11	-3.301196E-04
929	G	-5.328627E-03	-5.060262E-01	-6.728613E-08	-2.356037E-04	1.289709E-09	3.883672E-03
930	G	-5.328920E-03	-9.183339E-01	3.999854E-08	-4.682960E-04	1.531079E-11	-7.925967E-04
931	G	-5.329140E-03	-1.641120E-01	2.528509E-08	-2.649302E-04	-3.849195E-11	-5.150164E-03
932	G	-5.329140E-03	-1.641120E-01	-2.528719E-08	2.649302E-04	3.848830E-11	-5.150164E-03
933	G	-5.328920E-03	-9.183339E-01	-3.999979E-08	4.682960E-04	-1.531445E-11	-7.925967E-04
934	G	-5.328627E-03	-5.060262E-01	6.728574E-08	2.356037E-04	-1.289712E-09	3.883672E-03
935	G	-5.329303E-03	5.560906E-01	1.744369E-08	7.058461E-05	-3.039191E-11	-3.300974E-04
936	G	-5.329412E-03	3.810803E-01	1.048166E-08	1.944995E-04	-2.994979E-11	1.933808E-03
937	G	-5.329466E-03	-2.780242E-01	3.506328E-09	1.379348E-04	-2.921008E-11	3.418953E-03
938	G	-5.329466E-03	-2.780242E-01	-3.510987E-09	-1.379348E-04	2.920640E-11	3.418953E-03
939	G	-5.329412E-03	3.810803E-01	-1.048546E-08	-1.944995E-04	2.994611E-11	1.933808E-03
940	G	-5.329303E-03	5.560906E-01	-1.744663E-08	-7.058461E-05	3.038826E-11	-3.300974E-04

(c) Eigenvector for λ_3

Figure 3.8: First three eigenvectors for MPC Model

EIGENVALUE = 7.040863E+00
CYCLES = 4.223117E-01 REAL EIGENVECTOR NO. 7

POINT ID.	TYPE	T1	T2	T3	R1	R2	R3
913	G	6.238903E-08	-1.098762E-02	1.899927E-09	-1.068848E-05	4.256363E-11	1.339190E-04
914	G	6.188469E-08	7.403030E-02	-1.449015E-10	-1.863050E-05	-4.810457E-13	3.659184E-04
915	G	6.188284E-08	2.259253E-01	-3.499263E-11	-1.352476E-05	6.572266E-15	5.346658E-04
916	G	6.188348E-08	4.234540E-01	-4.401400E-11	-7.916092E-06	2.071563E-14	6.407071E-04
917	G	6.188347E-08	6.470983E-01	-5.061064E-11	-3.491726E-06	1.974181E-14	6.934936E-04
918	G	6.188347E-08	8.816345E-01	-5.719717E-11	-1.007028E-06	1.976695E-14	7.093232E-04
919	G	6.188742E-08	8.816345E-01	-5.719753E-11	1.007028E-06	1.976562E-14	7.093232E-04
920	G	6.188742E-08	6.470983E-01	-5.060655E-11	3.491726E-06	1.979069E-14	6.934936E-04
921	G	6.188744E-08	4.234540E-01	-4.402568E-11	7.916092E-06	1.881665E-14	6.407071E-04
922	G	6.188680E-08	2.259253E-01	-3.986960E-11	1.352476E-05	3.295982E-14	5.346658E-04
923	G	6.188864E-08	7.403030E-02	8.321651E-11	1.863050E-05	5.205772E-13	3.659184E-04
924	G	6.239298E-08	-1.098762E-02	-1.948435E-09	1.068848E-05	-4.252410E-11	1.339190E-04
925	G	-6.265971E-08	-1.098758E-02	1.918362E-09	-1.068850E-05	-4.252410E-11	-1.339192E-04
926	G	-6.215538E-08	7.403030E-02	-1.132787E-10	-1.863050E-05	5.205769E-13	-3.659184E-04
927	G	-6.215353E-08	2.259237E-01	9.806616E-12	-1.352481E-05	3.295811E-14	-5.346646E-04
928	G	-6.215417E-08	4.234559E-01	1.396201E-11	-7.916042E-06	1.881415E-14	-6.407078E-04
929	G	-6.215415E-08	6.470983E-01	2.054196E-11	-3.491726E-06	1.978820E-14	-6.934935E-04
930	G	-6.215415E-08	8.816323E-01	2.713204E-11	-1.007041E-06	1.976309E-14	-7.093232E-04
931	G	-6.215020E-08	8.816323E-01	2.713168E-11	1.007041E-06	1.976442E-14	-7.093232E-04
932	G	-6.215020E-08	6.470983E-01	2.054607E-11	3.491726E-06	1.973937E-14	-6.934935E-04
933	G	-6.215022E-08	4.234559E-01	1.395032E-11	7.916042E-06	2.071313E-14	-6.407078E-04
934	G	-6.214958E-08	2.259237E-01	4.929649E-12	1.352481E-05	6.569160E-15	-5.346646E-04
935	G	-6.215142E-08	7.403030E-02	1.148394E-10	1.863050E-05	-4.810499E-13	-3.659184E-04
936	G	-6.265576E-08	-1.098758E-02	-1.929976E-09	1.068850E-05	4.256362E-11	-1.339192E-04

(a) Eigenvector for λ_1

EIGENVALUE = 1.282851E+01
CYCLES = 5.700439E-01 REAL EIGENVECTOR NO. 8

POINT ID.	TYPE	T1	T2	T3	R1	R2	R3
913	G	9.219546E-02	1.123078E-01	1.103103E-09	1.690625E-05	-5.566565E-11	7.196822E-05
914	G	9.219549E-02	7.256830E-02	2.373817E-09	3.004494E-05	2.463490E-12	-2.961994E-04
915	G	9.219551E-02	-7.501128E-02	1.686860E-09	2.244607E-05	1.636788E-12	-5.730735E-04
916	G	9.219552E-02	-2.985700E-01	1.148234E-09	1.350022E-05	1.625397E-12	-7.525585E-04
917	G	9.219553E-02	-5.668847E-01	6.059542E-10	6.090441E-06	1.627886E-12	-8.443652E-04
918	G	9.219554E-02	-8.543217E-01	6.246100E-11	1.783856E-06	1.583070E-12	-8.725092E-04
919	G	9.219554E-02	-8.543217E-01	-4.425269E-10	-1.783857E-06	-1.376467E-12	-8.725092E-04
920	G	9.219553E-02	-5.668847E-01	-9.171527E-10	-6.090442E-06	-1.421286E-12	-8.443652E-04
921	G	9.219552E-02	-2.985700E-01	-1.390567E-09	-1.350022E-05	-1.418806E-12	-7.525585E-04
922	G	9.219551E-02	-7.501128E-02	-1.860331E-09	-2.244607E-05	-1.430210E-12	-5.730735E-04
923	G	9.219549E-02	7.256830E-02	-2.478431E-09	-3.004494E-05	-2.256929E-12	-2.961994E-04
924	G	9.219546E-02	1.123078E-01	-1.138868E-09	-1.690625E-05	5.587219E-11	7.196822E-05
925	G	9.219546E-02	-1.123078E-01	-1.042505E-09	-1.690629E-05	-5.566564E-11	7.196787E-05
926	G	9.219549E-02	-7.256831E-02	-2.313210E-09	-3.004494E-05	2.463470E-12	-2.961994E-04
927	G	9.219551E-02	7.500956E-02	-1.626266E-09	-2.244615E-05	1.636756E-12	-5.730714E-04
928	G	9.219552E-02	2.985723E-01	-1.087643E-09	-1.350014E-05	1.625358E-12	-7.525597E-04
929	G	9.219553E-02	5.668847E-01	-5.453810E-10	-6.090442E-06	1.627845E-12	-8.443652E-04
930	G	9.219554E-02	8.543191E-01	-1.907089E-12	-1.783879E-06	1.583027E-12	-8.725092E-04
931	G	9.219554E-02	8.543191E-01	5.030895E-10	1.783879E-06	-1.376512E-12	-8.725092E-04
932	G	9.219553E-02	5.668847E-01	9.777259E-10	6.090441E-06	-1.421329E-12	-8.443652E-04
933	G	9.219552E-02	2.985723E-01	1.451150E-09	1.350014E-05	-1.418843E-12	-7.525597E-04
934	G	9.219551E-02	7.500956E-02	1.920933E-09	2.244615E-05	-1.430240E-12	-5.730714E-04
935	G	9.219549E-02	-7.256831E-02	2.539039E-09	3.004494E-05	-2.256954E-12	-2.961994E-04
936	G	9.219546E-02	-1.123078E-01	1.199495E-09	1.690629E-05	5.587216E-11	7.196787E-05

(b) Eigenvector for λ_2

EIGENVALUE = 2.682172E+02
CYCLES = 2.606534E+00 REAL EIGENVECTOR NO. 9

POINT ID.	TYPE	T1	T2	T3	R1	R2	R3
913	G	-4.280383E-07	-5.257129E-02	-1.979486E-08	2.497487E-05	-2.410429E-10	-7.092273E-04
914	G	-4.264504E-07	-4.004619E-01	7.388123E-10	-1.894694E-05	6.139503E-13	-1.153472E-03
915	G	-4.263757E-07	-6.900525E-01	-9.056839E-12	-9.729971E-05	1.578457E-13	-4.302645E-04
916	G	-4.263823E-07	-6.242376E-01	2.993115E-13	-1.153549E-04	-7.106318E-15	8.530314E-04
917	G	-4.263831E-07	-1.442710E-01	7.462732E-13	-7.619560E-05	-3.343595E-16	1.941389E-03
918	G	-4.263836E-07	5.964208E-01	8.777061E-13	-2.755147E-05	-4.465125E-16	2.393462E-03
919	G	-4.263837E-07	5.964208E-01	9.274907E-13	2.755147E-05	-1.632165E-16	2.393462E-03
920	G	-4.263832E-07	-1.442710E-01	8.556999E-13	7.619560E-05	-2.753383E-16	1.941389E-03
921	G	-4.263823E-07	-6.242376E-01	1.099404E-12	1.153549E-04	6.496689E-15	8.530314E-04
922	G	-4.263757E-07	-6.900525E-01	1.025238E-11	9.729971E-05	-1.584551E-13	-4.302645E-04
923	G	-4.264505E-07	-4.004619E-01	-7.378198E-10	1.894694E-05	-6.145593E-13	-1.153472E-03
924	G	-4.280384E-07	-5.257129E-02	1.979565E-08	-2.497487E-05	2.410423E-10	-7.092273E-04
925	G	4.299944E-07	-5.257150E-02	-1.979506E-08	2.497492E-05	2.410424E-10	7.092282E-04
926	G	4.284066E-07	-4.004618E-01	7.383369E-10	-1.894695E-05	-6.145580E-13	1.153471E-03
927	G	4.283319E-07	-6.900512E-01	-9.730076E-12	-9.729921E-05	-1.584423E-13	4.302746E-04
928	G	4.283385E-07	-6.242350E-01	-5.720135E-13	-1.153548E-04	6.512777E-15	-8.530430E-04
929	G	4.283393E-07	-1.442710E-01	-3.229428E-13	-7.619560E-05	-2.592740E-16	-1.941388E-03
930	G	4.283398E-07	5.964135E-01	-3.894060E-13	-2.755178E-05	-1.471782E-16	-2.393460E-03
931	G	4.283398E-07	5.964135E-01	-3.393860E-13	2.755178E-05	-4.317483E-16	-2.393460E-03
932	G	4.283393E-07	-1.442710E-01	-2.128718E-13	7.619560E-05	-3.196721E-16	-1.941388E-03
933	G	4.283384E-07	-6.242350E-01	2.291793E-13	1.153548E-04	-7.091659E-15	-8.530430E-04
934	G	4.283318E-07	-6.900512E-01	9.580188E-12	9.729921E-05	1.578635E-13	4.302746E-04
935	G	4.284065E-07	-4.004618E-01	-7.382939E-10	1.894695E-05	6.139793E-13	1.153471E-03
936	G	4.299944E-07	-5.257150E-02	1.979529E-08	-2.497492E-05	-2.410429E-10	7.092282E-04

(c) Eigenvector for λ_3

Figure 3.9: First three eigenvectors for variant A

EIGENVALUE = 2.892920E+00
CYCLES = 2.707000E-01 REAL EIGENVECTOR NO. 7

POINT ID.	TYPE	T1	T2	T3	R1	R2	R3
913	G	3.930460E-08	-1.647401E-02	-2.290028E-10	-9.444220E-06	2.151209E-11	1.073600E-04
914	G	3.912156E-08	6.914440E-02	-3.728353E-10	-1.245704E-05	-2.704076E-13	2.948816E-04
915	G	3.912641E-08	2.220607E-01	-3.541641E-10	-8.697956E-06	-2.195526E-14	4.303462E-04
916	G	3.912635E-08	4.207073E-01	-3.437314E-10	-5.011218E-06	-2.541536E-14	5.152912E-04
917	G	3.912635E-08	6.454880E-01	-3.331587E-10	-2.131815E-06	-2.536838E-14	5.574992E-04
918	G	3.912635E-08	8.811272E-01	-3.225883E-10	-5.051514E-07	-2.536897E-14	5.700297E-04
919	G	3.912128E-08	8.811272E-01	-3.225884E-10	5.051537E-07	-2.536919E-14	5.700297E-04
920	G	3.912128E-08	6.454880E-01	-3.331590E-10	2.131817E-06	-2.536984E-14	5.574992E-04
921	G	3.912128E-08	4.207073E-01	-3.437272E-10	5.011220E-06	-2.532335E-14	5.152912E-04
922	G	3.912133E-08	2.220607E-01	-3.544358E-10	8.697958E-06	-2.878484E-14	4.303462E-04
923	G	3.911649E-08	6.914440E-02	-3.569067E-10	1.245704E-05	2.196650E-13	2.948816E-04
924	G	3.929952E-08	-1.647401E-02	-5.218827E-10	9.444222E-06	-2.156284E-11	1.073600E-04
925	G	-4.014495E-08	-1.647404E-02	-2.547959E-10	-9.444206E-06	-2.156285E-11	-1.073598E-04
926	G	-3.996191E-08	6.914440E-02	-4.197806E-10	-1.245704E-05	2.196532E-13	-2.948816E-04
927	G	-3.996676E-08	2.220620E-01	-4.222565E-10	-8.697925E-06	-2.879778E-14	-4.303470E-04
928	G	-3.996670E-08	4.207058E-01	-4.329707E-10	-5.011244E-06	-2.533791E-14	-5.152908E-04
929	G	-3.996670E-08	6.454880E-01	-4.435453E-10	-2.131815E-06	-2.538506E-14	-5.574992E-04
930	G	-3.996671E-08	8.811289E-01	-4.541223E-10	-5.051447E-07	-2.538455E-14	-5.700297E-04
931	G	-3.997178E-08	8.811289E-01	-4.541224E-10	5.051470E-07	-2.538427E-14	-5.700297E-04
932	G	-3.997178E-08	6.454880E-01	-4.435456E-10	2.131817E-06	-2.538355E-14	-5.574992E-04
933	G	-3.997178E-08	4.207058E-01	-4.329665E-10	5.011246E-06	-2.542990E-14	-5.152908E-04
934	G	-3.997184E-08	2.220620E-01	-4.225281E-10	8.697927E-06	-2.196809E-14	-4.303470E-04
935	G	-3.996699E-08	6.914440E-02	-4.038520E-10	1.245705E-05	-2.704155E-13	-2.948816E-04
936	G	-4.015003E-08	-1.647404E-02	-5.476868E-10	9.444209E-06	2.151210E-11	-1.073598E-04

(a) Eigenvector for λ_1

EIGENVALUE = 7.011163E+00
CYCLES = 4.214200E-01 REAL EIGENVECTOR NO. 8

POINT ID.	TYPE	T1	T2	T3	R1	R2	R3
913	G	-1.190341E-01	-1.645265E-01	-2.670494E-09	-1.794584E-05	3.190432E-11	-1.672785E-04
914	G	-1.190341E-01	-1.561170E-01	-1.521688E-09	-2.469187E-05	-2.421936E-12	1.943399E-04
915	G	-1.190341E-01	-1.433103E-02	-6.624849E-10	-1.815711E-05	-2.040776E-12	4.708663E-04
916	G	-1.190341E-01	2.231478E-01	1.899361E-10	-1.096599E-05	-2.046192E-12	6.535775E-04
917	G	-1.190341E-01	5.180107E-01	1.042472E-09	-4.848933E-06	-2.046450E-12	7.485408E-04
918	G	-1.190342E-01	8.376855E-01	1.897189E-09	-1.180570E-06	-2.019497E-12	7.777750E-04
919	G	-1.190342E-01	8.376855E-01	2.340757E-09	1.180573E-06	7.695310E-14	7.777750E-04
920	G	-1.190341E-01	5.180107E-01	2.386080E-09	4.848937E-06	1.039038E-13	7.485408E-04
921	G	-1.190341E-01	2.231478E-01	2.429220E-09	1.096599E-05	1.036397E-13	6.535775E-04
922	G	-1.190341E-01	-1.433103E-02	2.472244E-09	1.815712E-05	9.821251E-14	4.708663E-04
923	G	-1.190341E-01	-1.561170E-01	2.522043E-09	2.469187E-05	4.793539E-13	1.943399E-04
924	G	-1.190341E-01	-1.645265E-01	2.861434E-09	1.794584E-05	-3.384693E-11	-1.672785E-04
925	G	-1.190341E-01	1.645265E-01	1.873911E-09	1.794581E-05	3.190430E-11	-1.672787E-04
926	G	-1.190341E-01	1.561170E-01	7.250777E-10	2.469187E-05	-2.422041E-12	1.943399E-04
927	G	-1.190341E-01	1.432962E-02	-1.341864E-10	1.815706E-05	-2.040924E-12	4.708679E-04
928	G	-1.190341E-01	-2.231458E-01	-9.866629E-10	1.096604E-05	-2.046362E-12	6.535765E-04
929	G	-1.190341E-01	-5.180107E-01	-1.839278E-09	4.848937E-06	-2.046626E-12	7.485408E-04
930	G	-1.190342E-01	-8.376878E-01	-2.694077E-09	1.180558E-06	-2.019680E-12	7.777751E-04
931	G	-1.190342E-01	-8.376878E-01	-3.137639E-09	-1.180554E-06	7.677044E-14	7.777751E-04
932	G	-1.190341E-01	-5.180107E-01	-3.182886E-09	-4.848933E-06	1.037214E-13	7.485408E-04
933	G	-1.190341E-01	-2.231458E-01	-3.225952E-09	-1.096604E-05	1.034721E-13	6.535765E-04
934	G	-1.190341E-01	1.432962E-02	-3.268909E-09	-1.815705E-05	9.806678E-14	4.708679E-04
935	G	-1.190341E-01	1.561170E-01	-3.318653E-09	-2.469187E-05	4.792397E-13	1.943399E-04
936	G	-1.190341E-01	1.645265E-01	-3.658000E-09	-1.794581E-05	-3.384701E-11	-1.672787E-04

(b) Eigenvector for λ_2

EIGENVALUE = 1.096948E+02
CYCLES = 1.666914E+00 REAL EIGENVECTOR NO. 9

POINT ID.	TYPE	T1	T2	T3	R1	R2	R3
913	G	-2.680191E-07	-4.910652E-02	-4.124657E-09	2.980075E-05	-1.352436E-10	-5.681122E-04
914	G	-2.671542E-07	-3.991121E-01	9.747638E-11	-1.155372E-05	1.499920E-12	-9.293385E-04
915	G	-2.671801E-07	-6.910439E-01	3.761239E-12	-6.560472E-05	-1.980109E-14	-3.479469E-04
916	G	-2.671804E-07	-6.258256E-01	5.017998E-12	-7.694654E-05	6.797491E-16	6.832230E-04
917	G	-2.671808E-07	-1.449103E-01	4.822851E-12	-4.924823E-05	4.124198E-16	1.556279E-03
918	G	-2.671810E-07	5.968691E-01	4.649981E-12	-1.474780E-05	4.168320E-16	1.916096E-03
919	G	-2.671809E-07	5.968691E-01	4.665548E-12	1.474780E-05	4.903314E-16	1.916096E-03
920	G	-2.671807E-07	-1.449103E-01	4.870690E-12	4.924823E-05	4.947930E-16	1.556279E-03
921	G	-2.671803E-07	-6.258256E-01	5.053557E-12	7.694654E-05	2.276698E-16	6.832230E-04
922	G	-2.671800E-07	-6.910439E-01	6.688527E-12	6.560472E-05	2.070930E-14	-3.479469E-04
923	G	-2.671542E-07	-3.991121E-01	-8.664800E-11	1.155372E-05	-1.499011E-12	-9.293385E-04
924	G	-2.680190E-07	-4.910652E-02	4.135864E-09	-2.980075E-05	1.352445E-10	-5.681122E-04
925	G	2.676357E-07	-4.910635E-02	-4.124223E-09	2.980071E-05	1.352445E-10	5.681115E-04
926	G	2.667708E-07	-3.991121E-01	9.832944E-11	-1.155371E-05	-1.498983E-12	9.293385E-04
927	G	2.667967E-07	-6.910449E-01	4.999361E-12	-6.560499E-05	2.072472E-14	3.479404E-04
928	G	2.667970E-07	-6.258277E-01	6.640789E-12	-7.694663E-05	2.437801E-16	-6.832155E-04
929	G	2.667974E-07	-1.449103E-01	6.830475E-12	-4.924823E-05	5.111404E-16	-1.556279E-03
930	G	2.667976E-07	5.968748E-01	7.042454E-12	-1.474763E-05	5.068223E-16	-1.916097E-03
931	G	2.667977E-07	5.968748E-01	7.057991E-12	1.474763E-05	4.333876E-16	-1.916097E-03
932	G	2.667975E-07	-1.449103E-01	6.878232E-12	4.924823E-05	4.289416E-16	-1.556279E-03
933	G	2.667971E-07	-6.258277E-01	6.676240E-12	7.694663E-05	6.959010E-16	-6.832155E-04
934	G	2.667968E-07	-6.910449E-01	7.926364E-12	6.560499E-05	-1.978623E-14	3.479404E-04
935	G	2.667709E-07	-3.991121E-01	-8.579447E-11	1.155371E-05	1.499920E-12	9.293385E-04
936	G	2.676358E-07	-4.910635E-02	4.136368E-09	-2.980071E-05	-1.352436E-10	5.681115E-04

(c) Eigenvector for λ_3

Figure 3.10: First three eigenvectors for variant B

EIGENVALUE = 1.40149/E+00
CYCLES = 1.884153E-01 REAL EIGENVECTOR NO. 7

POINT ID.	TYPE	T1	T2	T3	R1	R2	R3
913	G	2.640343E-08	-2.182203E-02	-1.241476E-09	-8.110267E-06	1.146209E-11	8.989530E-05
914	G	2.643118E-08	6.438805E-02	-8.534147E-10	-8.799380E-06	-7.463131E-14	2.473335E-04
915	G	2.643249E-08	2.182240E-01	-8.348155E-10	-6.048218E-06	-4.705000E-14	3.606064E-04
916	G	2.643249E-08	4.179208E-01	-8.113239E-10	-3.464307E-06	-4.688844E-14	4.315938E-04
917	G	2.643249E-08	6.438180E-01	-7.878785E-10	-1.444667E-06	-4.689114E-14	4.668426E-04
918	G	2.643249E-08	8.805825E-01	-7.644330E-10	-2.974336E-07	-4.689097E-14	4.772507E-04
919	G	2.642312E-08	8.805825E-01	-7.644330E-10	2.974392E-07	-4.689103E-14	4.772507E-04
920	G	2.642311E-08	6.438180E-01	-7.878785E-10	1.444673E-06	-4.689119E-14	4.668426E-04
921	G	2.642311E-08	4.179208E-01	-8.113245E-10	3.464313E-06	-4.689512E-14	4.315938E-04
922	G	2.642311E-08	2.182240E-01	-8.347252E-10	6.048223E-06	-4.673669E-14	3.606064E-04
923	G	2.642180E-08	6.438805E-02	-8.630205E-10	8.799386E-06	-1.916097E-14	2.473335E-04
924	G	2.639405E-08	-2.182203E-02	-5.218575E-10	8.110273E-06	-1.155590E-11	8.989530E-05
925	G	-2.851221E-08	-2.182203E-02	-1.293071E-09	-8.110267E-06	-1.155590E-11	-8.989530E-05
926	G	-2.853995E-08	6.438805E-02	-9.519151E-10	-8.799380E-06	-1.918019E-14	-2.473335E-04
927	G	-2.854127E-08	2.182240E-01	-9.802220E-10	-6.048218E-06	-4.676259E-14	-3.606064E-04
928	G	-2.854127E-08	4.179208E-01	-1.003637E-09	-3.464307E-06	-4.692470E-14	-4.315938E-04
929	G	-2.854127E-08	6.438180E-01	-1.027098E-09	-1.444667E-06	-4.692231E-14	-4.668426E-04
930	G	-2.854127E-08	8.805825E-01	-1.050559E-09	-2.974336E-07	-4.692255E-14	-4.772507E-04
931	G	-2.855065E-08	8.805825E-01	-1.050559E-09	2.974392E-07	-4.692248E-14	-4.772507E-04
932	G	-2.855065E-08	6.438180E-01	-1.027098E-09	1.444673E-06	-4.692228E-14	-4.668426E-04
933	G	-2.855065E-08	4.179208E-01	-1.003637E-09	3.464313E-06	-4.691797E-14	-4.315938E-04
934	G	-2.855065E-08	2.182240E-01	-9.801317E-10	6.048223E-06	-4.707589E-14	-3.606064E-04
935	G	-2.854933E-08	6.438805E-02	-9.615209E-10	8.799386E-06	-7.465056E-14	-2.473335E-04
936	G	-2.852159E-08	-2.182203E-02	-5.734526E-10	8.110273E-06	1.146209E-11	-8.989530E-05

(a) Eigenvector for λ_1

EIGENVALUE = 4.477313E+00
CYCLES = 3.367665E-01 REAL EIGENVECTOR NO. 8

POINT ID.	TYPE	T1	T2	T3	R1	R2	R3
913	G	-1.392049E-01	-2.139464E-01	-3.145765E-09	-1.791121E-05	1.946063E-11	-2.419705E-04
914	G	-1.392050E-01	-2.422994E-01	-1.700185E-09	-2.093055E-05	-9.116889E-13	1.166437E-04
915	G	-1.392050E-01	-1.099750E-01	-1.267867E-09	-1.559864E-05	-8.845268E-13	3.981881E-04
916	G	-1.392050E-01	1.406902E-01	-8.257275E-10	-9.593765E-06	-8.841265E-13	5.890457E-04
917	G	-1.392050E-01	4.639848E-01	-3.836697E-10	-4.239170E-06	-8.840750E-13	6.903102E-04
918	G	-1.392050E-01	8.192129E-01	6.072359E-11	-9.095584E-07	-8.701576E-13	7.218343E-04
919	G	-1.392050E-01	8.192129E-01	4.574845E-10	9.095593E-07	7.072641E-13	7.218343E-04
920	G	-1.392050E-01	4.639848E-01	8.204318E-10	4.239170E-06	7.211907E-13	6.903102E-04
921	G	-1.392050E-01	1.406902E-01	1.181054E-09	9.593766E-06	7.212780E-13	5.890457E-04
922	G	-1.392050E-01	-1.099750E-01	1.541785E-09	1.559864E-05	7.217596E-13	3.981881E-04
923	G	-1.392050E-01	-2.422994E-01	1.892751E-09	2.093056E-05	7.490700E-13	1.166437E-04
924	G	-1.392049E-01	-2.139464E-01	3.257071E-09	1.791121E-05	-1.962302E-11	-2.419705E-04
925	G	-1.392049E-01	2.139464E-01	3.167850E-09	1.791121E-05	1.946081E-11	-2.419705E-04
926	G	-1.392050E-01	2.422994E-01	1.722419E-09	2.093056E-05	-9.112958E-13	1.166437E-04
927	G	-1.392050E-01	1.099750E-01	1.290338E-09	1.559864E-05	-8.839907E-13	3.981881E-04
928	G	-1.392050E-01	-1.406902E-01	8.484906E-10	9.593766E-06	-8.835119E-13	5.890457E-04
929	G	-1.392050E-01	-4.639848E-01	4.067515E-10	4.239170E-06	-8.834260E-13	6.903102E-04
930	G	-1.392050E-01	-8.192129E-01	-3.731411E-11	9.095593E-07	-8.695008E-13	7.218343E-04
931	G	-1.392050E-01	-8.192129E-01	-4.340750E-10	-9.095584E-07	7.079208E-13	7.218343E-04
932	G	-1.392050E-01	-4.639848E-01	-7.973501E-10	-4.239170E-06	7.218389E-13	6.903102E-04
933	G	-1.392050E-01	-1.406902E-01	-1.158290E-09	-9.593765E-06	7.218926E-13	5.890457E-04
934	G	-1.392050E-01	1.099750E-01	-1.519314E-09	-1.559864E-05	7.222953E-13	3.981881E-04
935	G	-1.392050E-01	2.422994E-01	-1.870517E-09	-2.093055E-05	7.494633E-13	1.166437E-04
936	G	-1.392049E-01	2.139464E-01	-3.234986E-09	-1.791121E-05	-1.962285E-11	-2.419705E-04

(b) Eigenvector for λ_2

EIGENVALUE = 5.287835E+01
CYCLES = 1.157335E+00 REAL EIGENVECTOR NO. 9

POINT ID.	TYPE	T1	T2	T3	R1	R2	R3
913	G	-1.824828E-07	-4.580446E-02	8.850438E-10	2.918246E-05	-7.669456E-11	-4.746688E-04
914	G	-1.826411E-07	-3.975893E-01	-1.102569E-11	-8.215879E-06	2.750517E-13	-7.784793E-04
915	G	-1.826510E-07	-6.912703E-01	1.289780E-11	-4.702465E-05	8.890704E-16	-2.923289E-04
916	G	-1.826513E-07	-6.266444E-01	1.225720E-11	-5.473802E-05	6.815896E-16	5.693718E-04
917	G	-1.826514E-07	-1.453071E-01	1.190931E-11	-3.443145E-05	6.994307E-16	1.298286E-03
918	G	-1.826515E-07	5.970606E-01	1.155974E-11	-9.022122E-06	6.994888E-16	1.597331E-03
919	G	-1.826514E-07	5.970606E-01	1.156590E-11	9.022121E-06	7.239539E-16	1.597331E-03
920	G	-1.826513E-07	-1.453071E-01	1.192798E-11	3.443145E-05	7.239526E-16	1.298286E-03
921	G	-1.826511E-07	-6.266444E-01	1.229179E-11	5.473802E-05	7.417759E-16	5.693718E-04
922	G	-1.826509E-07	-6.912703E-01	1.236290E-11	4.702465E-05	5.346383E-16	-2.923289E-04
923	G	-1.826409E-07	-3.975893E-01	3.699841E-11	8.215879E-06	-2.736271E-13	-7.784793E-04
924	G	-1.824827E-07	-4.580446E-02	-8.583583E-10	-2.918246E-05	7.669599E-11	-4.746688E-04
925	G	1.825196E-07	-4.580446E-02	8.858312E-10	2.918246E-05	7.669600E-11	4.746688E-04
926	G	1.826778E-07	-3.975893E-01	-9.519449E-12	-8.215879E-06	-2.736162E-13	7.784793E-04
927	G	1.826878E-07	-6.912703E-01	1.512214E-11	-4.702465E-05	5.474156E-16	2.923289E-04
928	G	1.826880E-07	-6.266444E-01	1.519991E-11	-5.473802E-05	7.553963E-16	-5.693718E-04
929	G	1.826882E-07	-1.453071E-01	1.557062E-11	-3.443145E-05	7.377958E-16	-1.298286E-03
930	G	1.826883E-07	5.970606E-01	1.593967E-11	-9.022122E-06	7.378415E-16	-1.597331E-03
931	G	1.826885E-07	5.970606E-01	1.594581E-11	9.022121E-06	7.133439E-16	-1.597331E-03
932	G	1.826884E-07	-1.453071E-01	1.558929E-11	3.443145E-05	7.132667E-16	-1.298286E-03
933	G	1.826882E-07	-6.266444E-01	1.523453E-11	5.473802E-05	6.952551E-16	-5.693718E-04
934	G	1.826879E-07	-6.912703E-01	1.458724E-11	4.702465E-05	9.018205E-16	2.923289E-04
935	G	1.826780E-07	-3.975893E-01	3.850467E-11	8.215879E-06	2.750631E-13	7.784793E-04
936	G	1.825197E-07	-4.580446E-02	-8.575685E-10	-2.918246E-05	-7.669456E-11	4.746688E-04

(c) Eigenvector for λ_3

Figure 3.11: First three eigenvectors for variant C

EIGENVALUE = 1.490241E+02
CYCLES = 1.942891E+00 REAL EIGENVECTOR NO. 7

POINT ID.	TYPE	T1	T2	T3	R1	R2	R3
913	G	2.892161E-07	-6.809501E-03	2.245463E-08	-1.638898E-05	3.692477E-10	2.894364E-04
914	G	2.873086E-07	7.780222E-02	-1.200087E-09	-4.893984E-05	1.865104E-11	7.783324E-04
915	G	2.867964E-07	2.286547E-01	-1.944104E-10	-4.001927E-05	-1.987850E-12	1.138589E-03
916	G	2.868068E-07	4.251423E-01	-2.142325E-11	-2.488943E-05	-1.374937E-13	1.366653E-03
917	G	2.868104E-07	6.479188E-01	-2.742077E-11	-1.212360E-05	2.121500E-14	1.481018E-03
918	G	2.868104E-07	8.817921E-01	-3.016497E-11	-4.917976E-06	1.137182E-14	1.516301E-03
919	G	2.868118E-07	8.817921E-01	-3.013339E-11	4.917977E-06	8.381405E-15	1.516301E-03
920	G	2.868117E-07	6.479188E-01	-2.980458E-11	1.212360E-05	-1.461888E-15	1.481018E-03
921	G	2.868081E-07	4.251423E-01	-3.272916E-11	2.488943E-05	1.572464E-13	1.366653E-03
922	G	2.867977E-07	2.286547E-01	1.433308E-10	4.001928E-05	2.007602E-12	1.138589E-03
923	G	2.873100E-07	7.780222E-02	1.152080E-09	4.893984E-05	-1.863129E-11	7.783324E-04
924	G	2.892174E-07	-6.809501E-03	-2.249956E-08	1.638898E-05	-3.692280E-10	2.894364E-04
925	G	-2.892036E-07	-6.809508E-03	2.246011E-08	-1.638897E-05	-3.692280E-10	-2.894363E-04
926	G	-2.872962E-07	7.780220E-02	-1.191560E-09	-4.893984E-05	-1.863137E-11	-7.783324E-04
927	G	-2.867840E-07	2.286547E-01	-1.828219E-10	-4.001927E-05	2.007532E-12	-1.138589E-03
928	G	-2.867944E-07	4.251423E-01	-6.772862E-12	-2.488943E-05	1.571758E-13	-1.366653E-03
929	G	-2.867979E-07	6.479187E-01	-9.708439E-12	-1.212361E-05	-1.532839E-15	-1.481018E-03
930	G	-2.867980E-07	8.817921E-01	-9.390739E-12	-4.917976E-06	8.310250E-15	-1.516301E-03
931	G	-2.867967E-07	8.817921E-01	-9.359153E-12	4.917977E-06	1.130089E-14	-1.516301E-03
932	G	-2.867966E-07	6.479187E-01	-1.209232E-11	1.212361E-05	2.114418E-14	-1.481018E-03
933	G	-2.867930E-07	4.251423E-01	-1.807876E-11	2.488943E-05	-1.375643E-13	-1.366653E-03
934	G	-2.867827E-07	2.286547E-01	1.549194E-10	4.001928E-05	-1.987921E-12	-1.138589E-03
935	G	-2.872949E-07	7.780220E-02	1.160607E-09	4.893984E-05	1.865098E-11	-7.783324E-04
936	G	-2.892023E-07	-6.809508E-03	-2.249411E-08	1.638897E-05	3.692476E-10	-2.894363E-04

(a) Eigenvector for λ_1

EIGENVALUE = 2.033178E+02
CYCLES = 2.269383E+00 REAL EIGENVECTOR NO. 8

POINT ID.	TYPE	T1	T2	T3	R1	R2	R3
913	G	-6.068379E-02	-6.080651E-02	1.127039E-08	-2.107066E-05	4.066446E-10	9.289903E-05
914	G	-6.068385E-02	4.125170E-03	-8.914117E-09	-6.308119E-05	4.604840E-12	7.179175E-04
915	G	-6.068390E-02	1.543652E-01	-5.941721E-09	-5.215102E-05	-1.283685E-11	1.185584E-03
916	G	-6.068393E-02	3.642460E-01	-4.131426E-09	-3.279422E-05	-1.068825E-11	1.485908E-03
917	G	-6.068396E-02	6.089446E-01	-2.494067E-09	-1.612332E-05	-1.054972E-11	1.638416E-03
918	G	-6.068397E-02	8.685055E-01	-8.562076E-10	-6.581666E-06	-1.028350E-11	1.685937E-03
919	G	-6.068397E-02	8.685055E-01	7.962111E-10	6.581666E-06	1.035607E-11	1.685937E-03
920	G	-6.068396E-02	6.089446E-01	2.445360E-09	1.612332E-05	1.062229E-11	1.638416E-03
921	G	-6.068393E-02	3.642460E-01	4.094009E-09	3.279422E-05	1.076082E-11	1.485908E-03
922	G	-6.068390E-02	1.543652E-01	5.915594E-09	5.215102E-05	1.290943E-11	1.185584E-03
923	G	-6.068385E-02	4.125170E-03	8.899281E-09	6.308119E-05	-4.532264E-12	7.179175E-04
924	G	-6.068379E-02	-6.080651E-02	-1.127393E-08	2.107066E-05	-4.065721E-10	9.289903E-05
925	G	-6.068379E-02	6.080651E-02	-1.125380E-08	2.107065E-05	4.066446E-10	9.289893E-05
926	G	-6.068385E-02	-4.125148E-03	8.930721E-09	6.308119E-05	4.604862E-12	7.179174E-04
927	G	-6.068390E-02	-1.543652E-01	5.958326E-09	5.215102E-05	-1.283684E-11	1.185584E-03
928	G	-6.068393E-02	-3.642460E-01	4.148032E-09	3.279422E-05	-1.068824E-11	1.485908E-03
929	G	-6.068396E-02	-6.089445E-01	2.510676E-09	1.612333E-05	-1.054971E-11	1.638416E-03
930	G	-6.068397E-02	-8.685055E-01	8.728174E-10	6.581666E-06	-1.028349E-11	1.685937E-03
931	G	-6.068397E-02	-8.685055E-01	-7.796013E-10	-6.581666E-06	1.035608E-11	1.685937E-03
932	G	-6.068396E-02	-6.089445E-01	-2.428753E-09	-1.612333E-05	1.062230E-11	1.638416E-03
933	G	-6.068393E-02	-3.642460E-01	-4.077402E-09	-3.279422E-05	1.076083E-11	1.485908E-03
934	G	-6.068390E-02	-1.543652E-01	-5.898989E-09	-5.215102E-05	1.290944E-11	1.185584E-03
935	G	-6.068385E-02	-4.125148E-03	-8.882678E-09	-6.308119E-05	-4.532259E-12	7.179174E-04
936	G	-6.068379E-02	6.080651E-02	1.129054E-08	-2.107065E-05	-4.065720E-10	9.289893E-05

(b) Eigenvector for λ_2

EIGENVALUE = 5.683811E+03
CYCLES = 1.199886E+01 REAL EIGENVECTOR NO. 9

POINT ID.	TYPE	T1	T2	T3	R1	R2	R3
913	G	-2.025844E-06	-5.546009E-02	-1.903932E-07	-3.137746E-06	-1.552685E-09	-1.521892E-03
914	G	-2.035052E-06	-4.000425E-01	3.891998E-10	-7.395012E-05	-2.002922E-10	-2.440153E-03
915	G	-2.031442E-06	-6.854999E-01	1.292289E-09	-2.647920E-04	6.450861E-12	-9.052104E-04
916	G	-2.031394E-06	-6.192828E-01	9.999191E-12	-3.190304E-04	1.387507E-12	1.816550E-03
917	G	-2.031439E-06	-1.424734E-01	-1.029109E-11	-2.288933E-04	-3.536335E-14	4.134212E-03
918	G	-2.031451E-06	5.948362E-01	-5.378782E-13	-1.152025E-04	-2.159908E-14	5.114862E-03
919	G	-2.031451E-06	5.948362E-01	1.455048E-12	1.152025E-04	2.089724E-14	5.114862E-03
920	G	-2.031439E-06	-1.424734E-01	1.109905E-11	2.288933E-04	3.466162E-14	4.134212E-03
921	G	-2.031394E-06	-6.192828E-01	-9.300395E-12	3.190304E-04	-1.388208E-12	1.816550E-03
922	G	-2.031442E-06	-6.854999E-01	-1.291699E-09	2.647920E-04	-6.451563E-12	-9.052104E-04
923	G	-2.035052E-06	-4.000425E-01	-3.887191E-10	7.395012E-05	2.002915E-10	-2.440153E-03
924	G	-2.025844E-06	-5.546009E-02	1.903935E-07	3.137746E-06	1.552685E-09	-1.521892E-03
925	G	2.025517E-06	-5.546006E-02	-1.903933E-07	-3.137759E-06	1.552685E-09	1.521892E-03
926	G	2.034724E-06	-4.000425E-01	3.891333E-10	-7.395008E-05	2.002920E-10	2.440153E-03
927	G	2.031115E-06	-6.854999E-01	1.292198E-09	-2.647920E-04	-6.451052E-12	9.052105E-04
928	G	2.031067E-06	-6.192828E-01	9.879107E-12	-3.190304E-04	-1.387695E-12	-1.816550E-03
929	G	2.031112E-06	-1.424737E-01	-1.044050E-11	-2.288933E-04	3.517480E-14	-4.134211E-03
930	G	2.031123E-06	5.948362E-01	-7.166463E-13	-1.152025E-04	2.141058E-14	-5.114862E-03
931	G	2.031123E-06	5.948362E-01	1.276049E-12	1.152025E-04	-2.108252E-14	-5.114862E-03
932	G	2.031112E-06	-1.424737E-01	1.094890E-11	2.288933E-04	-3.484679E-14	-4.134211E-03
933	G	2.031067E-06	-6.192828E-01	-9.421731E-12	3.190304E-04	1.388023E-12	-1.816550E-03
934	G	2.031115E-06	-6.854999E-01	-1.291792E-09	2.647920E-04	6.451379E-12	9.052105E-04
935	G	2.034724E-06	-4.000425E-01	-3.887779E-10	7.395008E-05	-2.002917E-10	2.440153E-03
936	G	2.025517E-06	-5.546006E-02	1.903936E-07	3.137759E-06	-1.552684E-09	1.521892E-03

(c) Eigenvector for λ_3

Figure 3.12: First three eigenvectors for scaled model

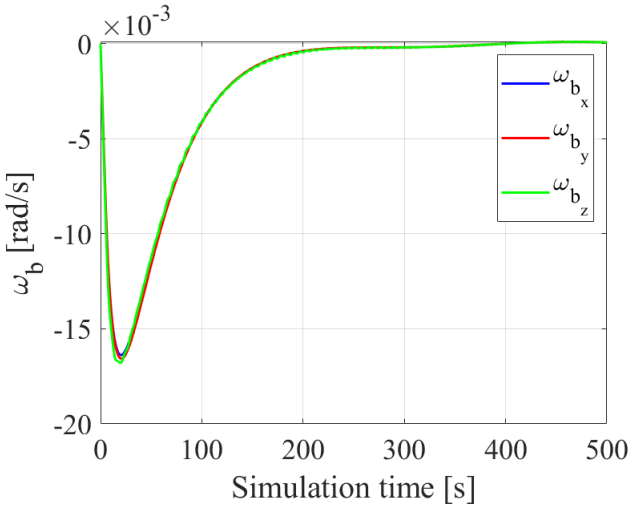

(a) Angular velocities trend

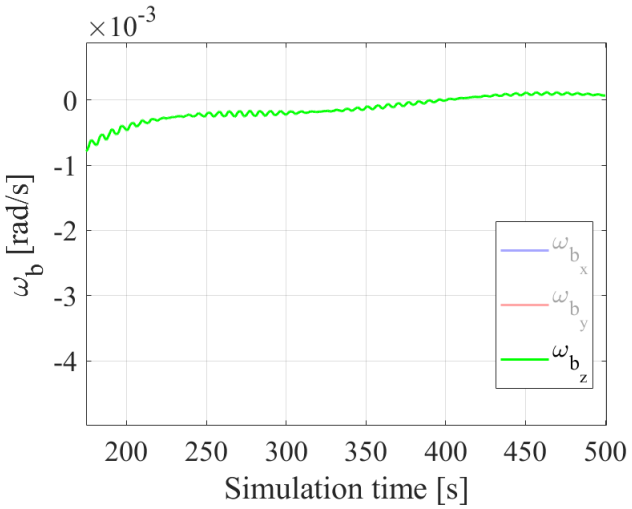

(b) Zoom on ω_{b_z}

Figure 3.13: Trends of angular velocities considering three modal modes

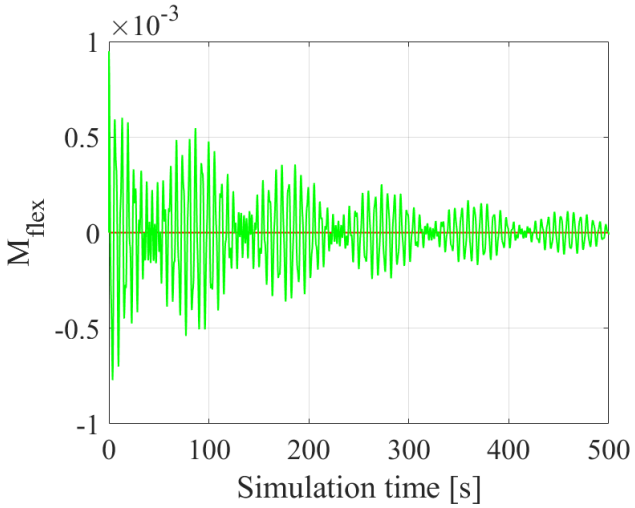

Figure 3.14: Perturbation momentum around z-axis

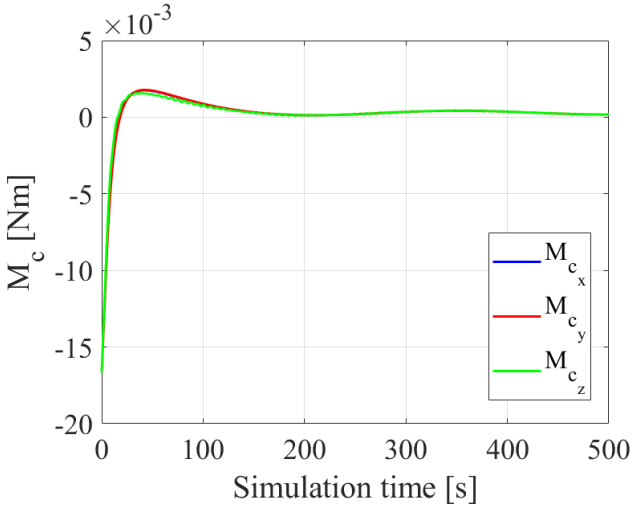

Figure 3.15: Control torque considering three modal modes

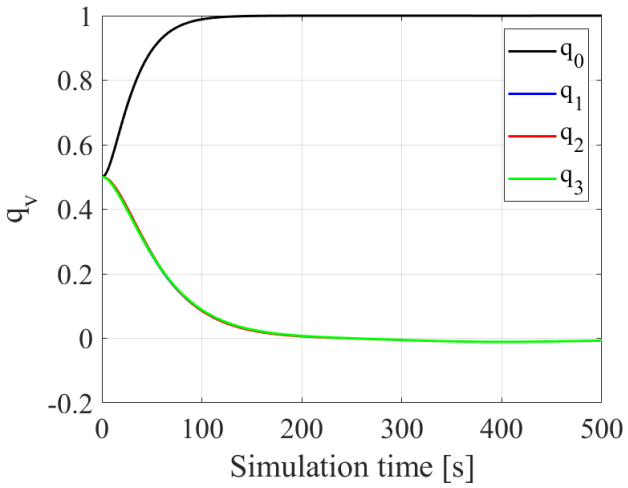

Figure 3.16: Quaternions' trend considering three modal modes

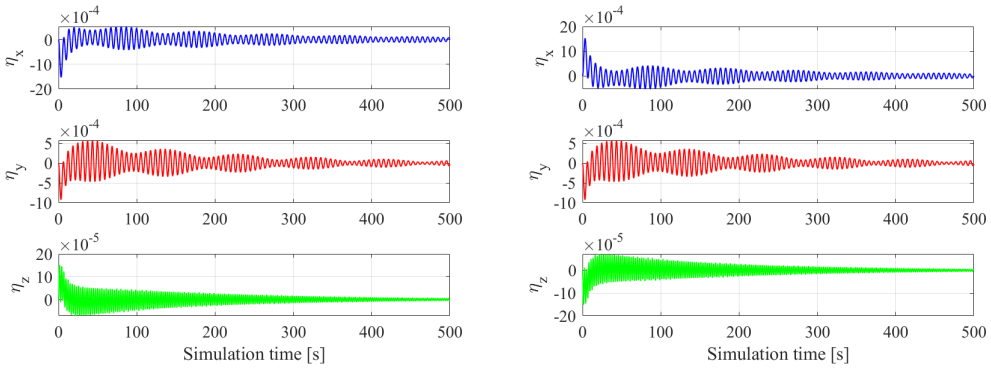

(a) Panel 1

(b) Panel 2

Figure 3.17: Modal coordinates of panels in standard model considering three modal modes

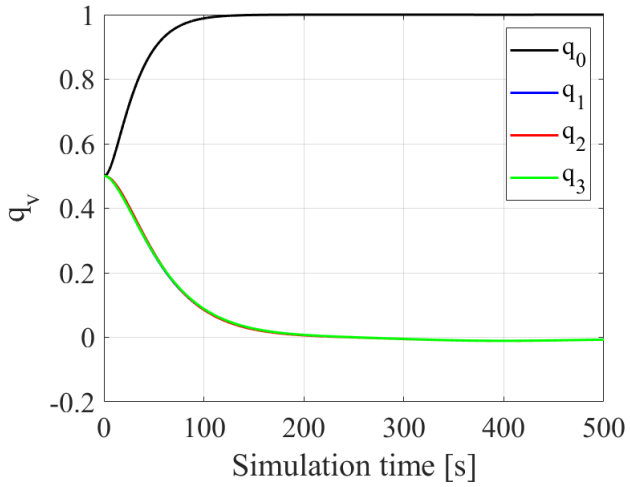

Figure 3.18: Quaternions for the standard model considering five modes

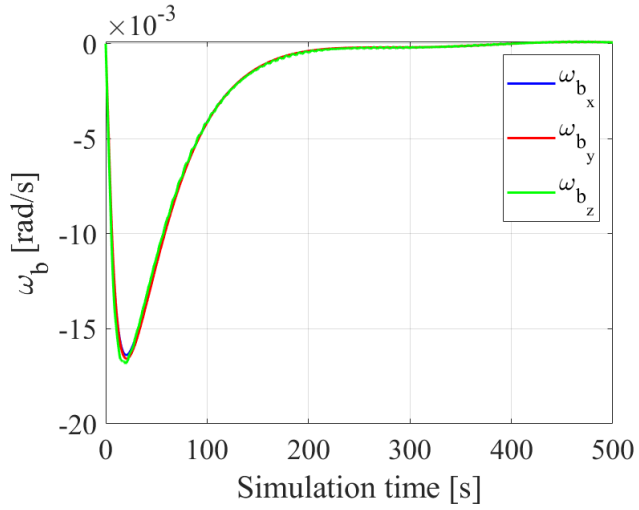

Figure 3.19: Angular velocities evolution for the standard model considering five modes

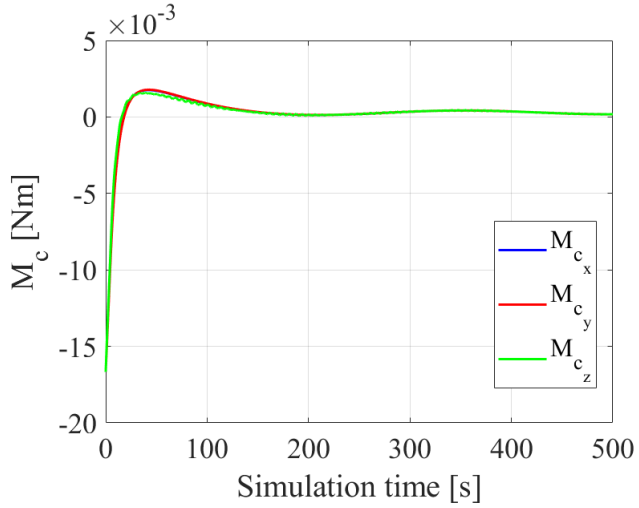

Figure 3.20: Control torque for the standard model considering five modes

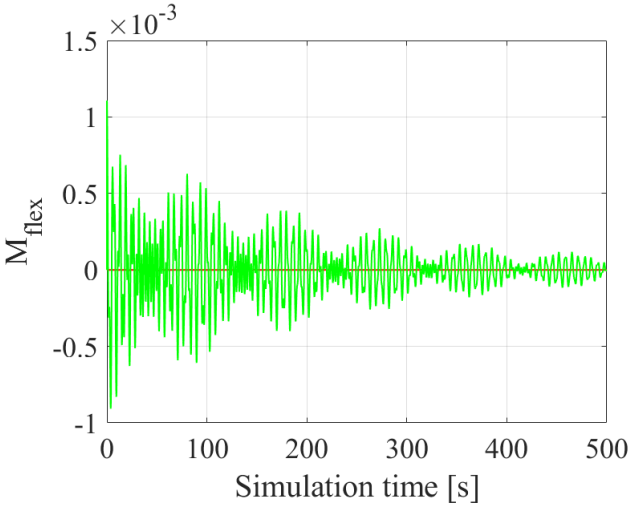

Figure 3.21: Perturbation momentum by flexible panels for the standard model considering five modes

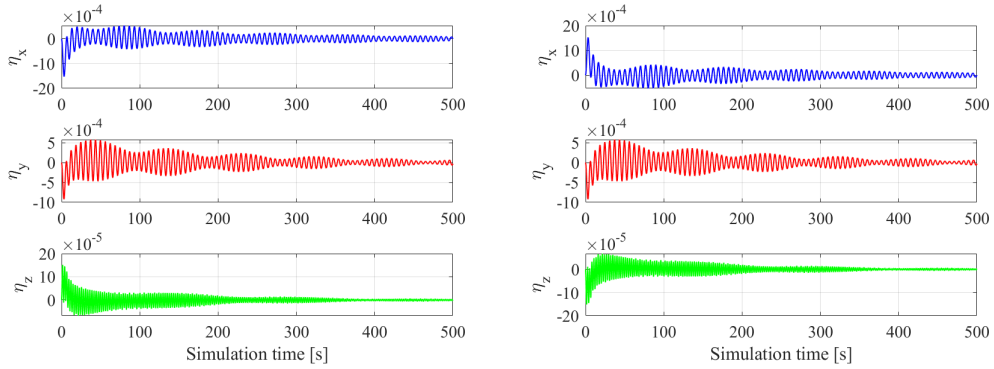

(a) Panel 1

(b) Panel 2

Figure 3.22: Modal coordinates of panels for the standard model considering five modes

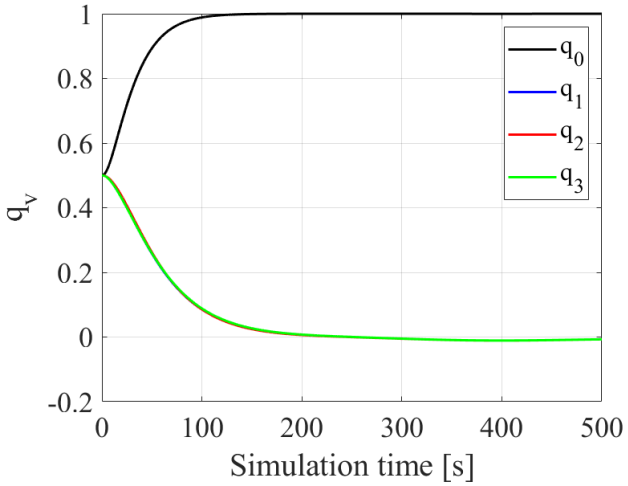

Figure 3.23: Quaternions for the standard model considering ten modes

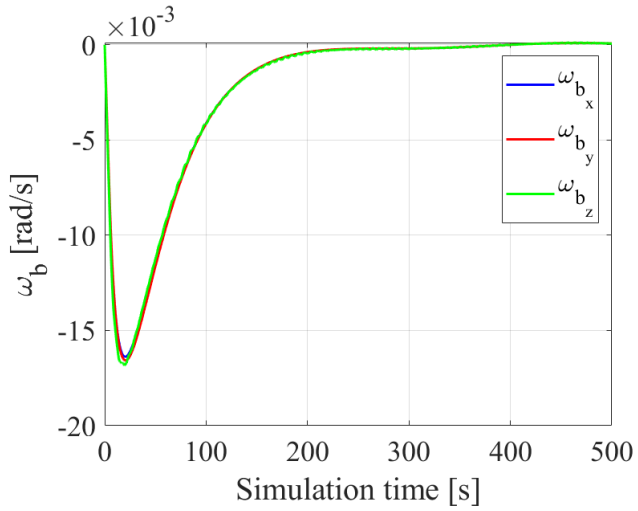

Figure 3.24: Angular velocities evolution for the standard model considering ten modes

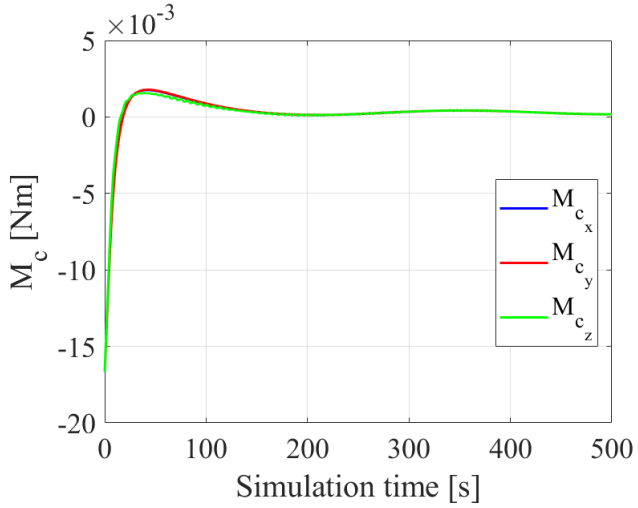

Figure 3.25: Control torque for the standard model considering ten modes

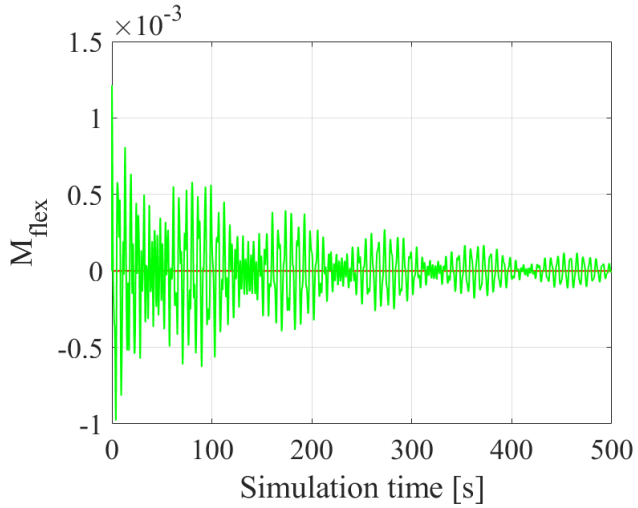

Figure 3.26: Perturbation momentum by flexible panels for the standard model considering ten modes

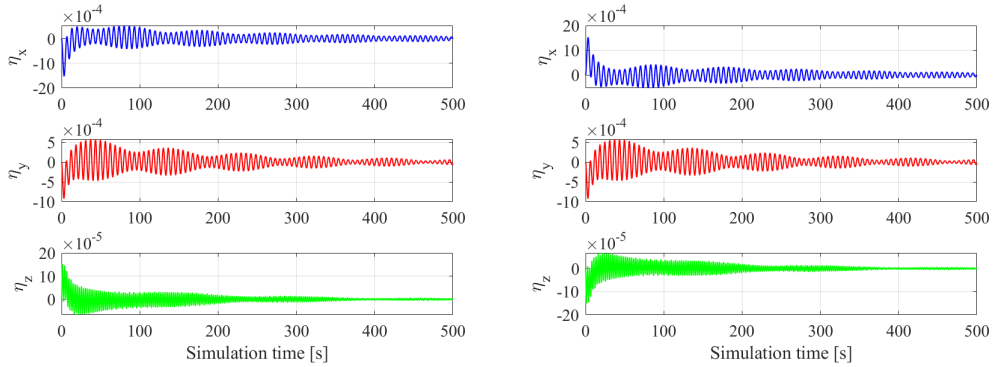

(a) Panel 1 (b) Panel 2

Figure 3.27: Modal coordinates of panels for the standard model considering ten modes

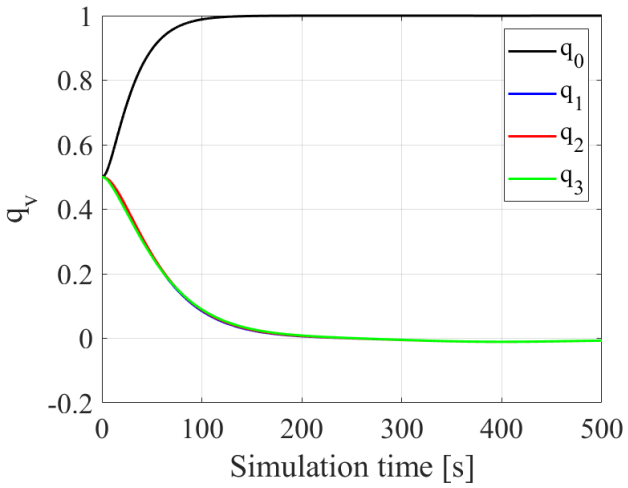

Figure 3.28: Quaternions trend for MPC model

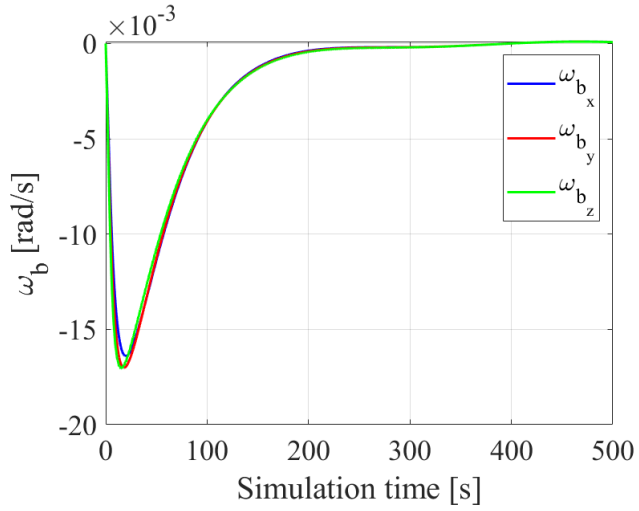

Figure 3.29: Angular velocities of MPC model

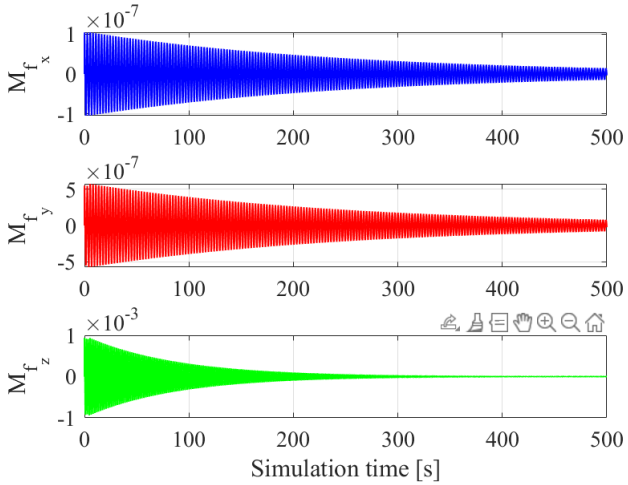

Figure 3.30: Perturbation moment given by the four flexible panels

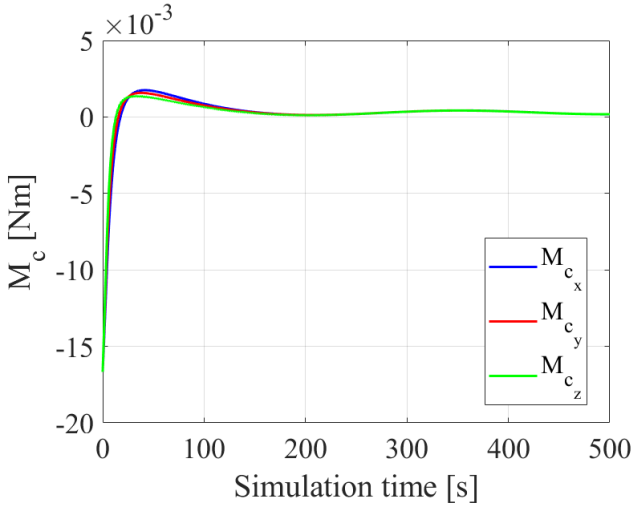

Figure 3.31: Control torques in MPC model

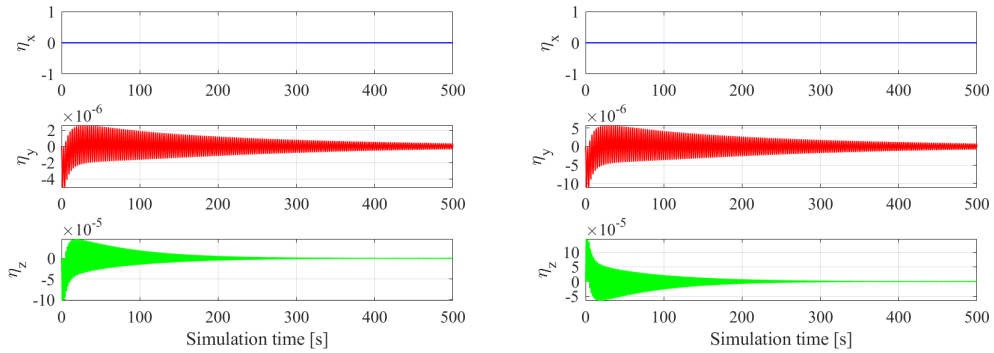

(a) Panel 1

(b) Panel 2

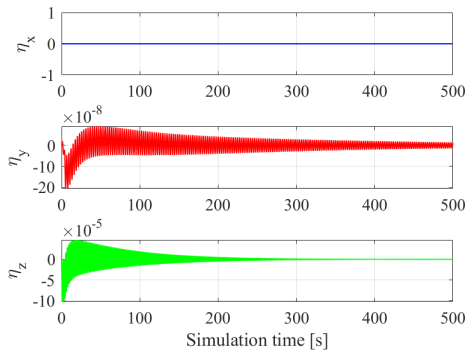

(c) Panel 3

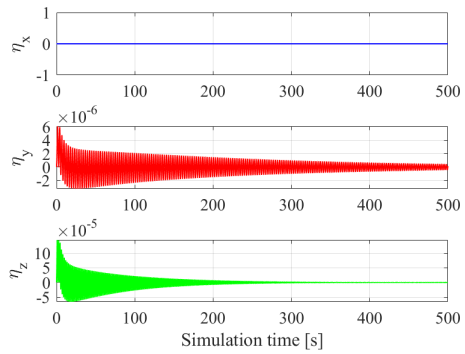

(d) Panel 4

Figure 3.32: Modal coordinates of flexible panels in MPC model

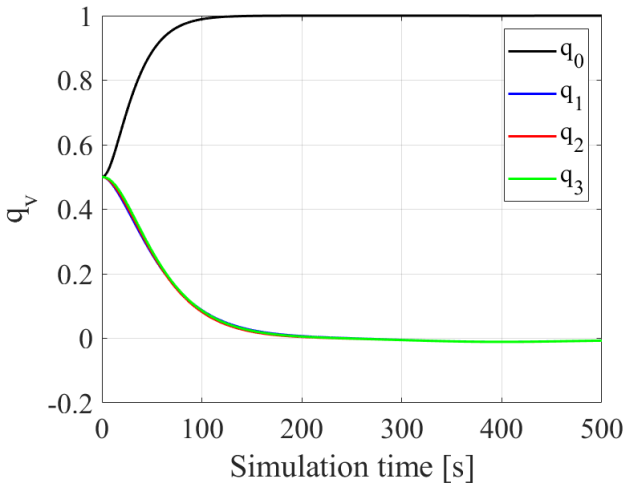

Figure 3.33: Quaternions trend for variant A

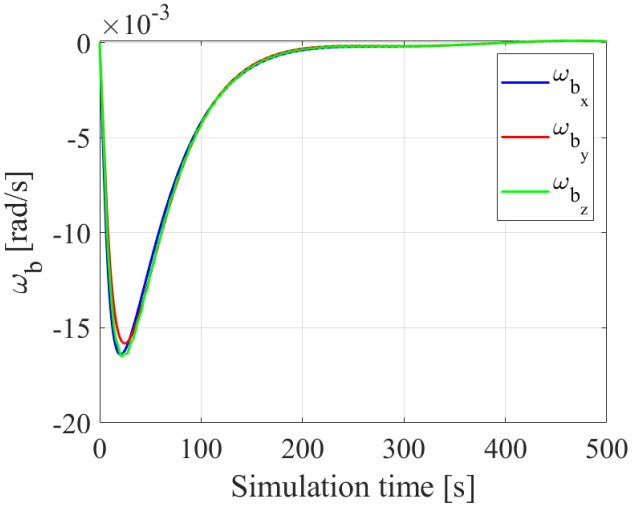

Figure 3.34: Angular velocities of variant A

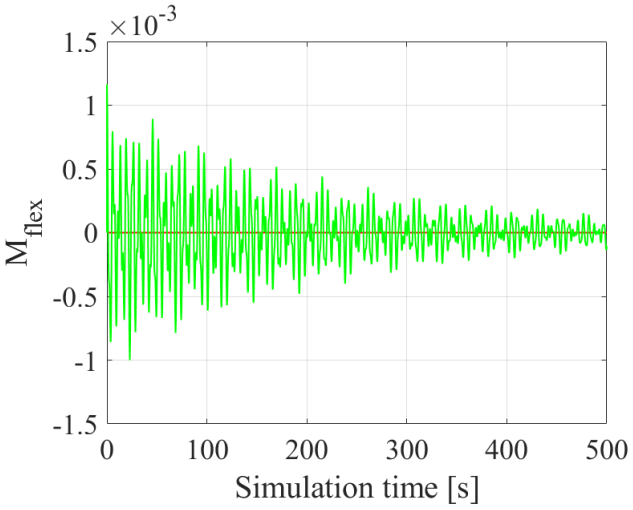

Figure 3.35: Perturbation moment given by the flexible panels in variant A

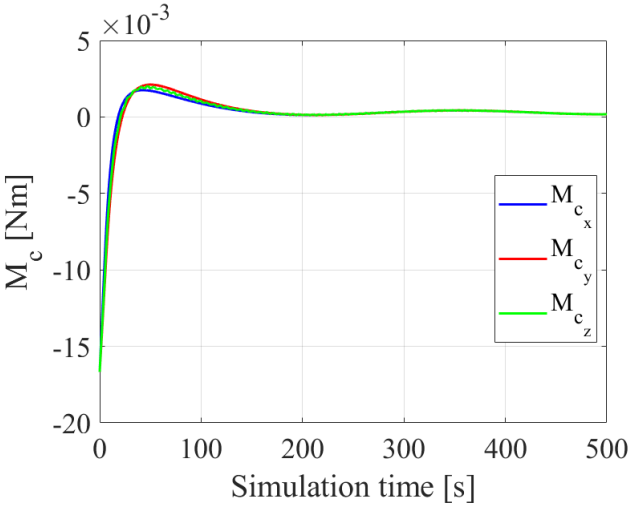

Figure 3.36: Control torques in variant A

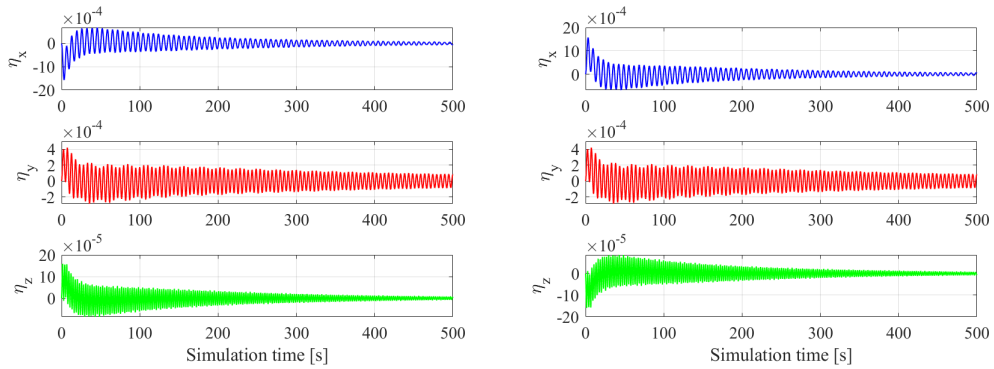

(a) Panel 1 (b) Panel 2

Figure 3.37: Modal coordinates of flexible panels in variant A

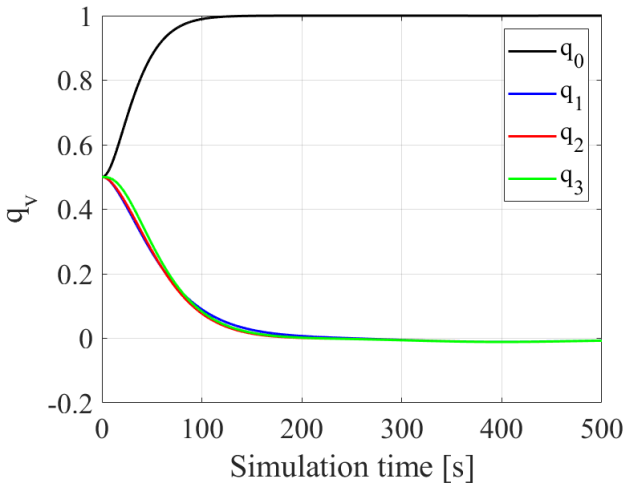

Figure 3.38: Quaternions trend for variant B

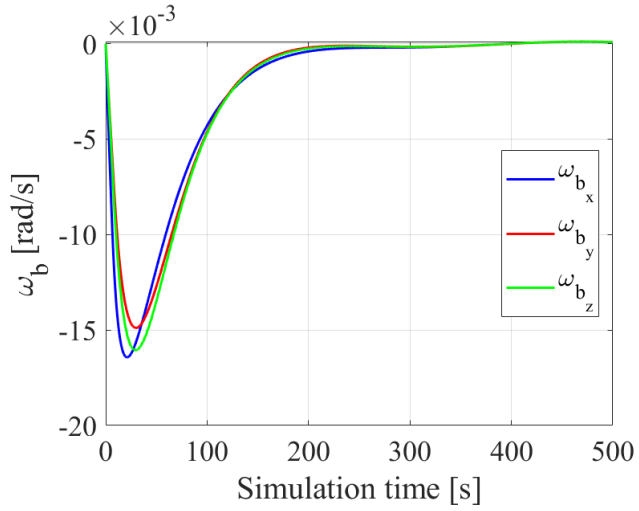

Figure 3.39: Angular velocities of variant B

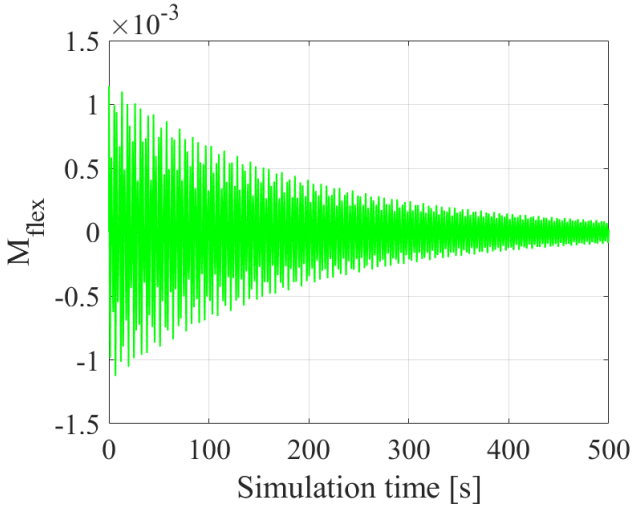

Figure 3.40: Perturbation moment given by the flexible panels in variant B

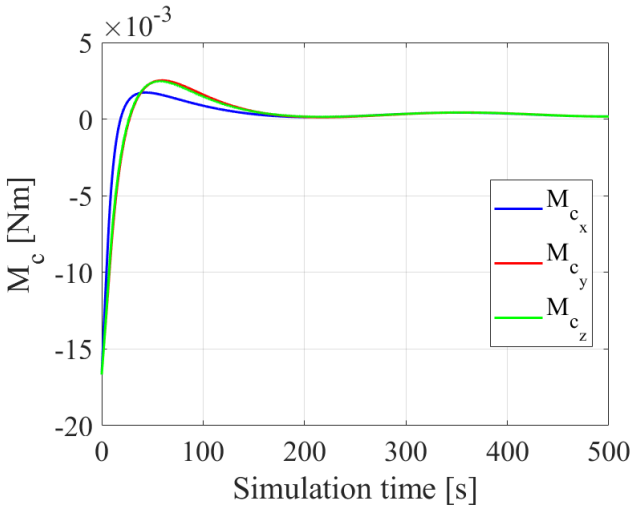

Figure 3.41: Control torques in variant B

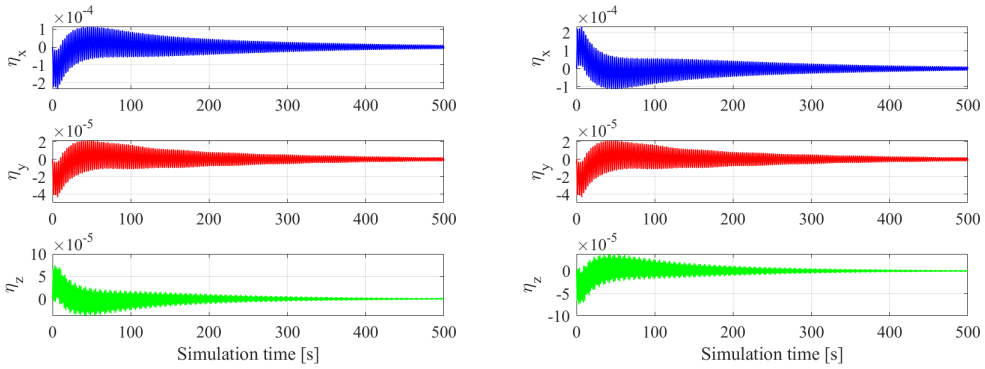

(a) Panel 1

(b) Panel 2

Figure 3.42: Modal coordinates of flexible panels in variant B

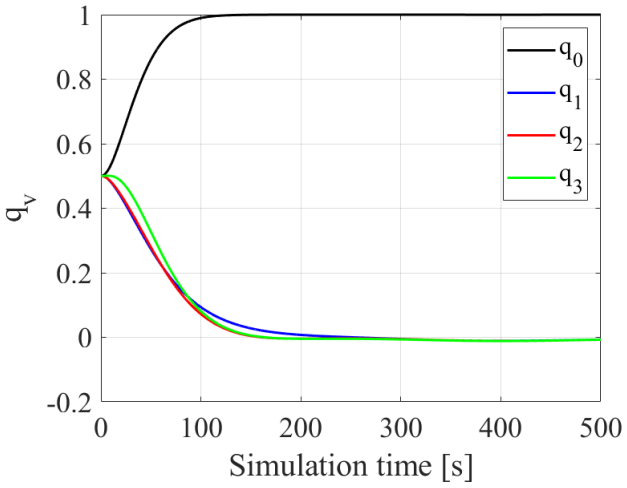

Figure 3.43: Quaternions trend for variant C

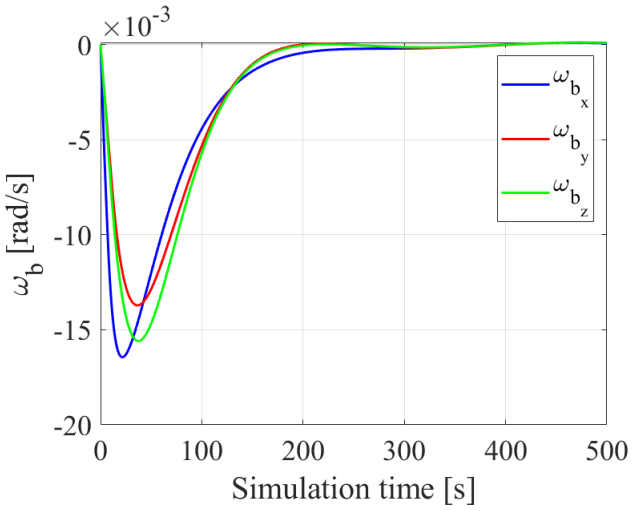

(a) Angular velocities trend

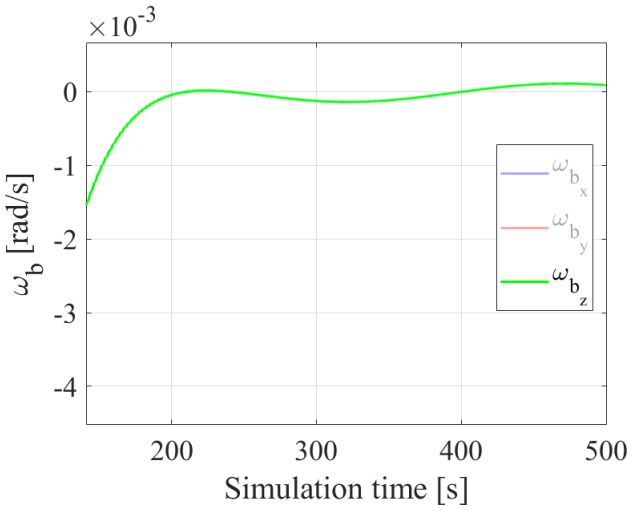

(b) Zoom on ω_{b_z}

Figure 3.44: Trends of angular velocities for variant C

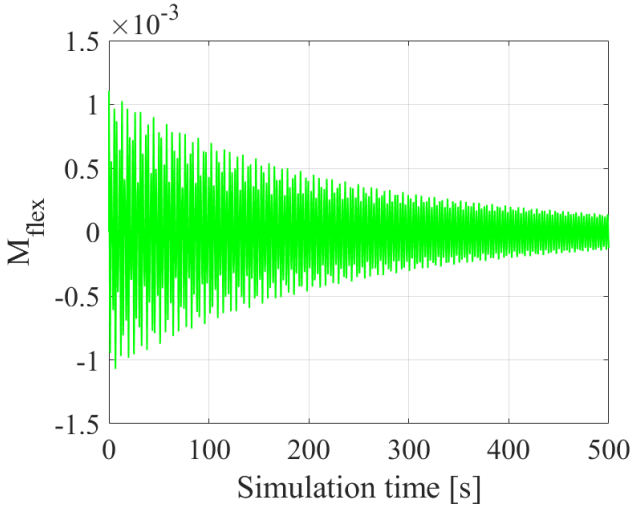

Figure 3.45: Perturbation moment given by the flexible panels in variant C

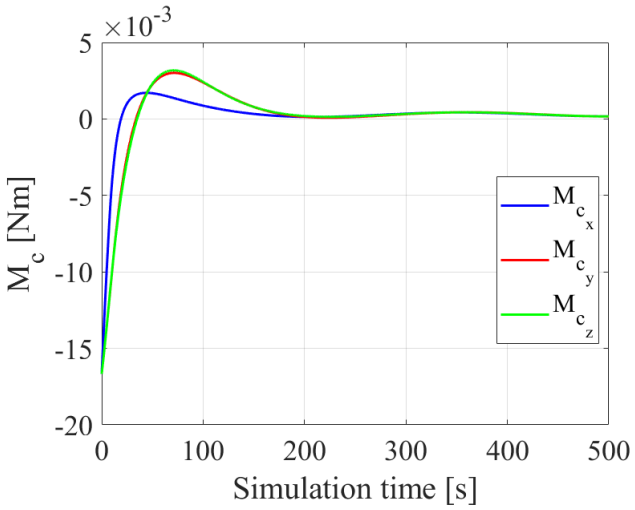

Figure 3.46: Control torques in variant C

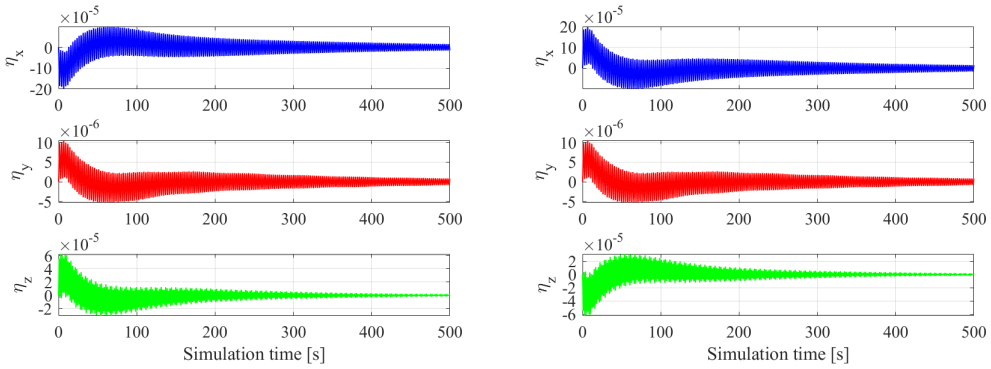

(a) Panel 1

(b) Panel 2

Figure 3.47: Modal coordinates of flexible panels in variant C

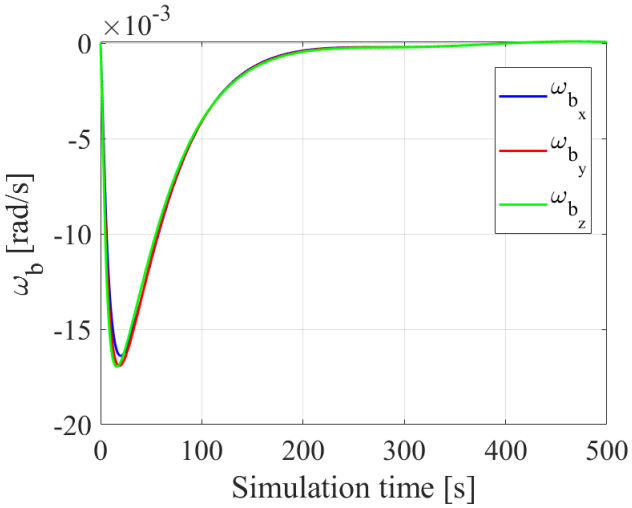

(a) Angular velocities trend

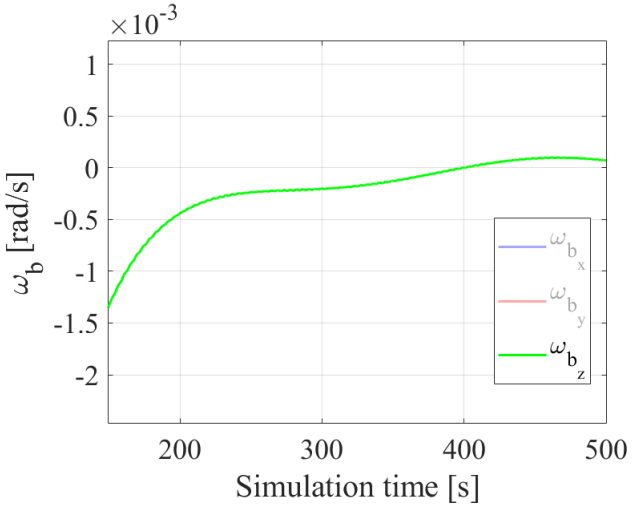

(b) Zoom on ω_{b_z}

Figure 3.48: Trends of angular velocities for scaled model

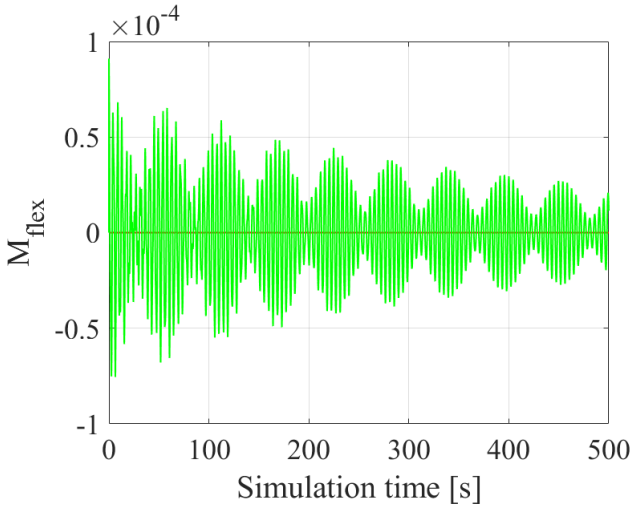

Figure 3.49: Perturbation momentum around z-axis for scaled model

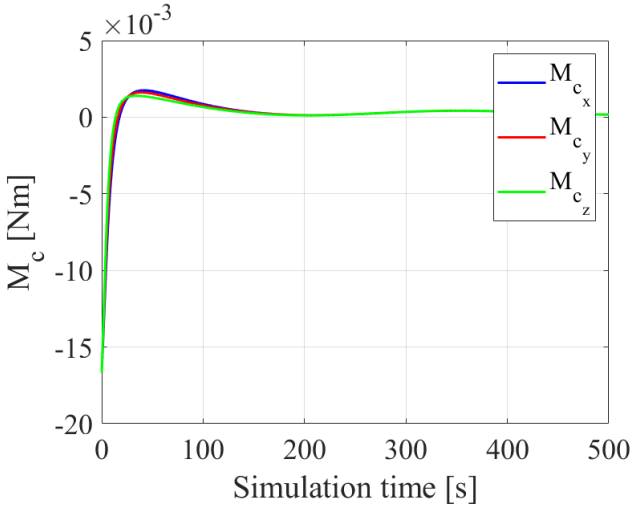

Figure 3.50: Control torque for scaled model

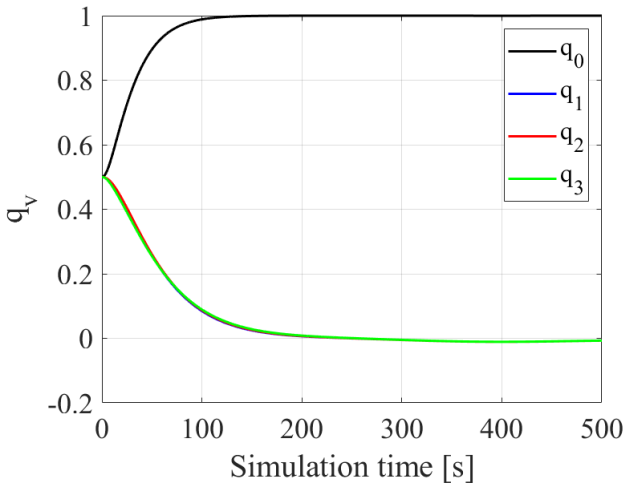

Figure 3.51: Quaternions' trend for scaled model

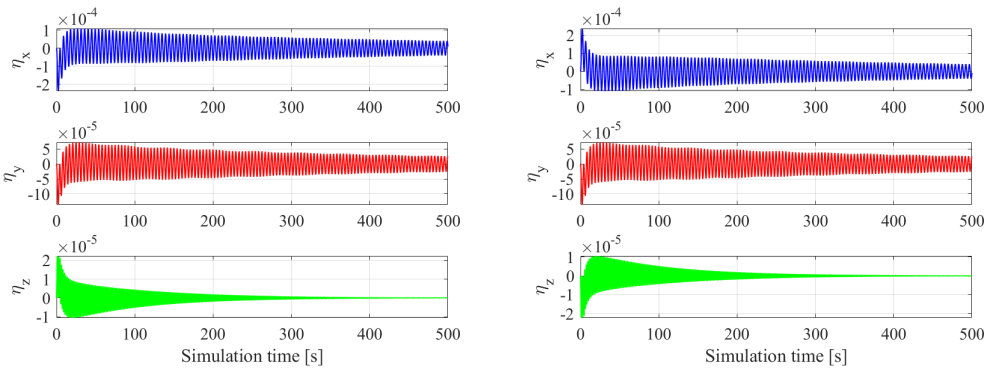

(a) Panel 1

(b) Panel 2

Figure 3.52: Modal coordinates of panels in scaled model

Chapter 4

Conclusions

This concluding chapter will provide a comprehensive reflection on the research presented throughout this thesis. This concluding chapter will revisit the key findings, discuss the significance of the methodologies employed, and examine the broader implications of the study in the context of attitude control systems for flexible satellites. In doing so, it will provide a synthesis of the work's contribution to the field. The final section will conclude with a forward-looking discussion addressing potential avenues for future research.

The initial stage of the study involved the introduction and detailed description of all the elements required for the definition and analysis of attitudes. This was followed by an explanation of the hybrid coordinate method for the rigid-flexible coupling in flexible structure studies. The attitude dynamics are studied with the use of Euler's equation, taking into account the perturbation resulting from the presence of flexible appendages and the reaction wheel torque model.
Subsequently, a concise overview of the finite element method (FEM) is provided, with a particular focus on the fundamental principles upon which this method is based. One of the objectives of this project is to evaluate the effect of flexible structures in different types of spacecraft. To this end, a series of finite element models have been developed and analysed using modal analysis in MSC Patran and Nastran. Particular attention has been paid to the interface between the rigid hub of the satellite and the panels. In order to verify how this connection impacts modal behaviour and control strategies, a model with MPC elements has been realised. The natural frequencies and eigenvectors obtained have been imported into Matlab and Simulink for designing an appropriate orbital simulator which takes into account the flexible panels' model. The design of the orbital simulator includes all the different subsystems that are necessary for an appropriate simulation of an inertial pointing manoeuvre, which is defined as the reaching of the desired attitude orientation. In order to address the challenges posed by orbital perturbations, which are typical of the harsh space environment, and internal disturbances deriving from the flexible panels, a QFC controller is selected and tuned to ensure the successful execution of the manoeuvre.
The results for all the configurations under consideration have been collated and compared, with the use of graphs, images and detailed observations. While the results demonstrate that the desired attitude has been successfully achieved in all of the case studies, there are a few areas that require further attention: firstly, the progressive increment of panels' length results

in similar evolution in simulation results, with a progressive reduction of oscillation in angular rates; then, the FEM analysis results show a counter intuitive behaviour, better explained in the following. The MPC-based methodology does not fully capture the uncertainties and flexibility introduced by the presence of hinges in the model, so the studied model results with a more rigid behaviour, as the higher natural frequencies suggest. However, in light of the specific objectives of this project, particularly the necessity for autonomous panel behaviour, the MPC-based methodology has been retained despite its inherent limitations and the overall framework provides a sufficient representation of the system's dynamics for the purposes of this investigation.

From this analysis, it is evident that future work should prioritise the refinement of the selection of MPC elements or the investigation of alternative modelling approaches to more accurately account for hinge flexibility. Furthermore, given that the modifications made to the spacecraft model do not significantly impact attitude dynamics, a methodology could be developed to eliminate the necessity of FEM analysis during parametric studies, thereby reducing the workload.

Bibliography

[1] ICEYE, "Truth. through uninterrupted earth observation." https://www.iceye.com/company. Last Accessed: 27/06/2024.

[2] "Iceye-x1 (sar microsatellite-x1), eo portal.." https://www.eoportal.org/satellite-missions/iceye-x1. Last Accessed: 27/06/2024.

[3] J. Van der Ha and F. Janssens, "Jet-damping and misalignment effects during solid-rocket-motor burn," *Journal of Guidance Control and Dynamics*, vol. 28, pp. 412–420, 05 2005.

[4] J. E. Scott R. Starin, "Attitude determination and contol systems," tech. rep.

[5] "Msc nastran 2012, dynamic analysis user's guide." https://hexagon.com/company/divisions/manufacturing-intelligence/msc-software.

[6] M. Mammarella, "Progettazione ed implementazione di algoritmi di controllo per applicazioni aerospaziali." Lezione 02 - Progettazione di sistemi di controllo, A.a 22/23.

[7] G. Avanzini, "Spacecraft attitude dynamics and control." Dispense del corso di Dinamica e Controllo di Assetto di Satelliti, A.A 2008-09.

[8] R. R. Bate, D. D. Mueller, J. E. White, and W. W. Saylor, *Fundamentals of Astrodynamics*. Dover Publication, 2020.

[9] F. L. Markley and J. L. Crassidis, *Fundamentals of Spacecraft Attitude Determination and Control*. Space Technology Library ; 33, New York, NY: Springer New York, 1st ed. 2014. ed., 2014.

[10] P. Likins, "Dynamics and control of flexible space vehicles," tech. rep., Jet Propulsion Lab, California Inst. of Tech.,Pasadena, CA, USA, January 15, 1970.

[11] H. A. Technologies, "Understanding reaction wheels." https://aerospace.honeywell.com. Accessed: 14/02/2024.

[12] E. Capello, D. Peaucelle, and M. Mancini, "Adaptive variable structure control system for attitude spacecraft applications." https://hdl.handle.net/11583/2976603, 2023-02-14.

[13] C. Liu, X. Yue, K. Shi, and Z. Sun, "Chapter 7 - improved mixed h2/h control with poles assignment constraint," in *Spacecraft Attitude Control* (C. Liu, X. Yue, K. Shi, and Z. Sun, eds.), pp. 205–232, Elsevier, 2022.

[14] D. J N Reddy, *An Introduction to the Finite Element Method*. McGraw-Hill Education, 2005.

[15] M. Gherlone, *Fondamenti di meccanica strutturale*. Gioacchino Onorati editore srl unip, 2018.

[16] D. Logan, *A First Course in the Finite Element Method*. Cengage Learning, 2011.

[17] T. Hughes, *The Finite Element Method: Linear Static and Dynamic Finite Element Analysis*. Dover Civil and Mechanical Engineering, Dover Publications, 2012.

[18] K. McConnell, *Vibration Testing: Theory and Practice*. A Wiley-Interscience publication, Wiley, 1995.

[19] D. Ewins, *Modal Testing: Theory, Practice and Application*. Mechanical Engineering Research Studies: Engineering Dynamics Series, Wiley, 2009.

[20] B. Pyne, H. Saito, P. R. Akbar, K. Tanaka, J. Hirokawa, and T. Tomura, "Flight model 7-panel slot-array deployable antenna measurement results of microx-sar 100kg class demonstration satellite," in *2020 50th European Microwave Conference (EuMC)*, pp. 816–819, 2021.

[21] S. Xie, K. Jing, H. Zhou, and X. Liu, "Mechanical properties of nomex honeycomb sandwich panels under dynamic impact," *Composite Structures*, vol. 235, p. 111814, 2020.

[22] J. C. Urschel, "Uniform erros estimates for the lanczos method," tech. rep., Department of Mathematics, Massachusetts Institute of Technology.

[23] NASA, "Guidance, navigation, and control." `https://www.nasa.gov/smallsat-institute/sst-soa/guidance-navigation-and-control/`. Last Accessed: 11/07/2024.